

1 **Supplementary Information**

2  
3 **Diffusionless Transformation of Soft Cubic Superstructure from Amorphous to Simple**  
4 **Cubic and Body-Centered Cubic Phases**

5  
6 *Jie Liu<sup>1,2</sup>, Wenzhe Liu<sup>3</sup>, Bo Guan<sup>4</sup>, Bo Wang<sup>3</sup>, Lei Shi<sup>3</sup>, Feng Jin<sup>1</sup>, Zhigang Zheng<sup>\*5</sup>, Jingxia*  
7 *Wang<sup>\*1,2</sup>, Tomiki Ikeda<sup>1</sup> and Lei Jiang<sup>1,2</sup>*

8  
9 <sup>1</sup> Key Laboratory of Bio-inspired Materials and Interfaces Sciences, Technical Institute of  
10 Physics and Chemistry, Chinese Academy of Sciences, Beijing, 100190, China

11  
12 <sup>2</sup> Center of Material Science and Optoelectronics Engineering, School of Future Technology,  
13 University of Chinese Academy of Sciences, Beijing 101407, China

14  
15 <sup>3</sup> Department of Physics, Key Laboratory of Micro-and Nano-Photonic Structures, and State  
16 Key Laboratory of Surface Physics, Fudan University, Shanghai 200433, China

17  
18 <sup>4</sup> Institute of Chemistry, Chinese Academy of Sciences, Beijing, 100190, China

19  
20 <sup>5</sup> Department of Physics, East China University of Science and Technology, Shanghai  
21 200237, China

22  
23 **Corresponding Author**

24 \*E-mail: jingxiawang@mail.ipc.ac.cn (Jingxia Wang).

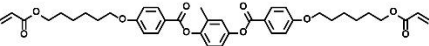
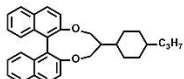
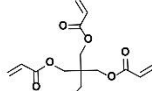
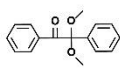
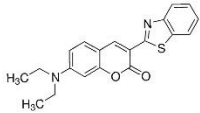
25 \*E-mail: zgzheng@ecust.edu.cn (Zhigang Zheng).

28 **Supplementary Note 1 Chemicals and corresponding structures**

29 **Supplementary Table 1** Abbreviation used in this work.

30		
31	DLPT	Diffusionless phase transformation
32	LC	Liquid crystal
33	BPLCs	Blue phase liquid crystals
34	PS-BPLCs	Polymer-stabilized blue phase liquid crystals
35	N*	Cholesteric phase
36	POM	Polarized optical microscopy
37	TEM	Transmission electron microscopy
38	FWHM	Full width at half maxima
39	DTCs	Double-twisted cylinders
40	SAXS	Small angle X-ray scattering
41	Syn-SAXS	Synchrotron small angle X-ray diffraction
42	ARM	micro-region angle resolved spectra system
43	FFT	fast Fourier transformation
44	BPI	Blue phase I
45	BPI <sub>{100}</sub>	BPI with {100} crystal plane parallel to the substrates
46	BPI <sub>{110}</sub>	BPI with {110} crystal plane parallel to the substrates
47	BPI <sub>{211}</sub>	BPI with {211} crystal plane parallel to the substrates
48	BPII	Blue phase II
49	BPII <sub>{100}</sub>	BPII with {100} crystal plane parallel to the substrates
50	BPII <sub>{110}</sub>	BPII with {110} crystal plane parallel to the substrates
51	BPIII	Blue phase III
52	BZ	Brillouin zone
53	BCC	Body-center cubic
54	SC	Simple cubic
55	C6	Coumarin 6
56	C6-BPLCs	Coumarin 6 doped blue phase liquid crystals
57	UV	Ultraviolet light
58	PET	Polyester
59	PI	Polyimide
60	1D	One-dimensional
61	2D	Two-dimensional
62	3D	Three-dimensional
63		

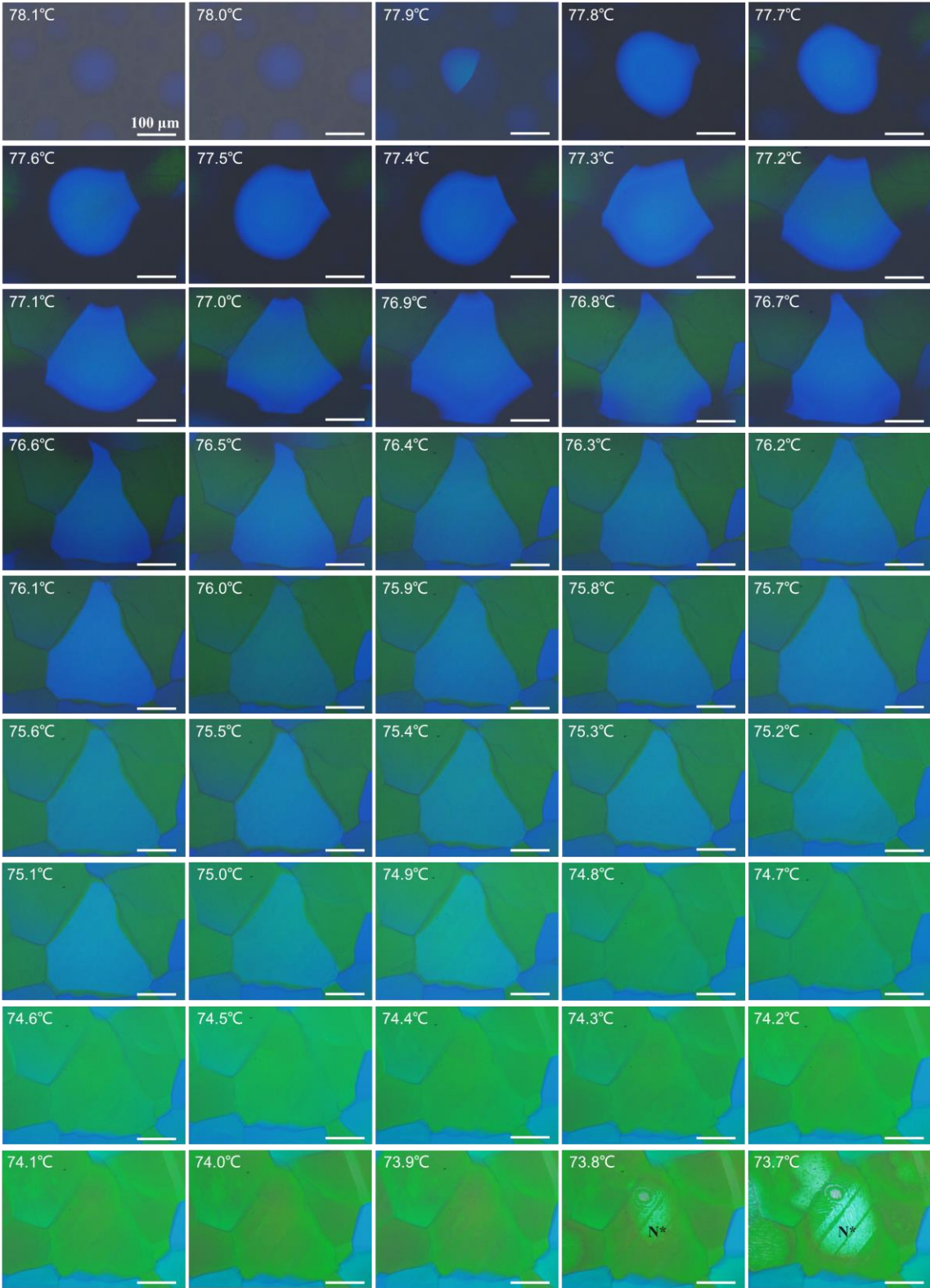
64 **Supplementary Table 2** Chemical structures of host LCs, reactive monomers, laser dye, and photoinitiator

Component Name	Chemical Structure	Synonyms
HTG135200	Commercial Nematic Liquid Crystal hybrid	
C6M		2-methyl-1,4-phenylene bis(4-((6-(acryloyloxy)hexyl)oxy)benzoate))
R5011		(13bR)-5,6-Dihydro-5-(trans-4-propylcyclohexyl)-4H-dinaphtho[2,1-f:1',2'-h][1,5]dioxin
TMPTA		1,1,1-Trimethylolpropane Triacrylate
I-651		2,2-Dimethoxy-2-phenylacetophenone
Coumarin 6 (C6)		3-(2-Benzothiazolyl)-N,N-diethylumbelliferylamine

65

66

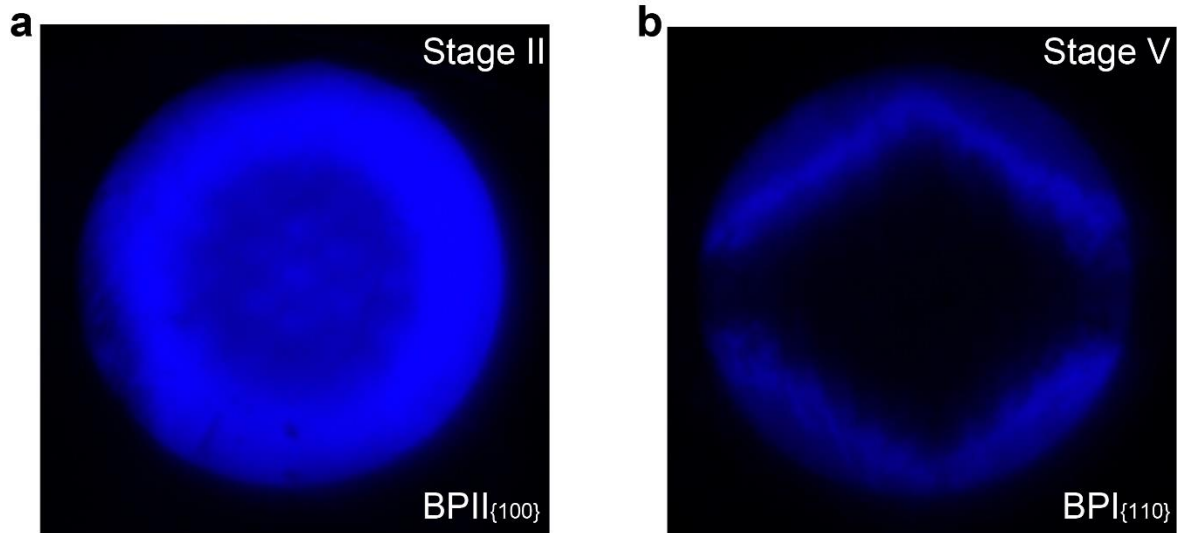
67 **Supplementary Note 2 Basic optical properties of the phase transition process of BPLCs**  
68 **using POM**



69 **Supplementary Fig. 1 Temperature dependence of optical textures focused on one domain.** Typical  
70 textures captured using POM for BPLCs during phase transformation from 78.1 to 73.7 °C (from Stage I to  
71 Stage IV). The temperature noted is from the bottom of the LC cell.  
72  
73

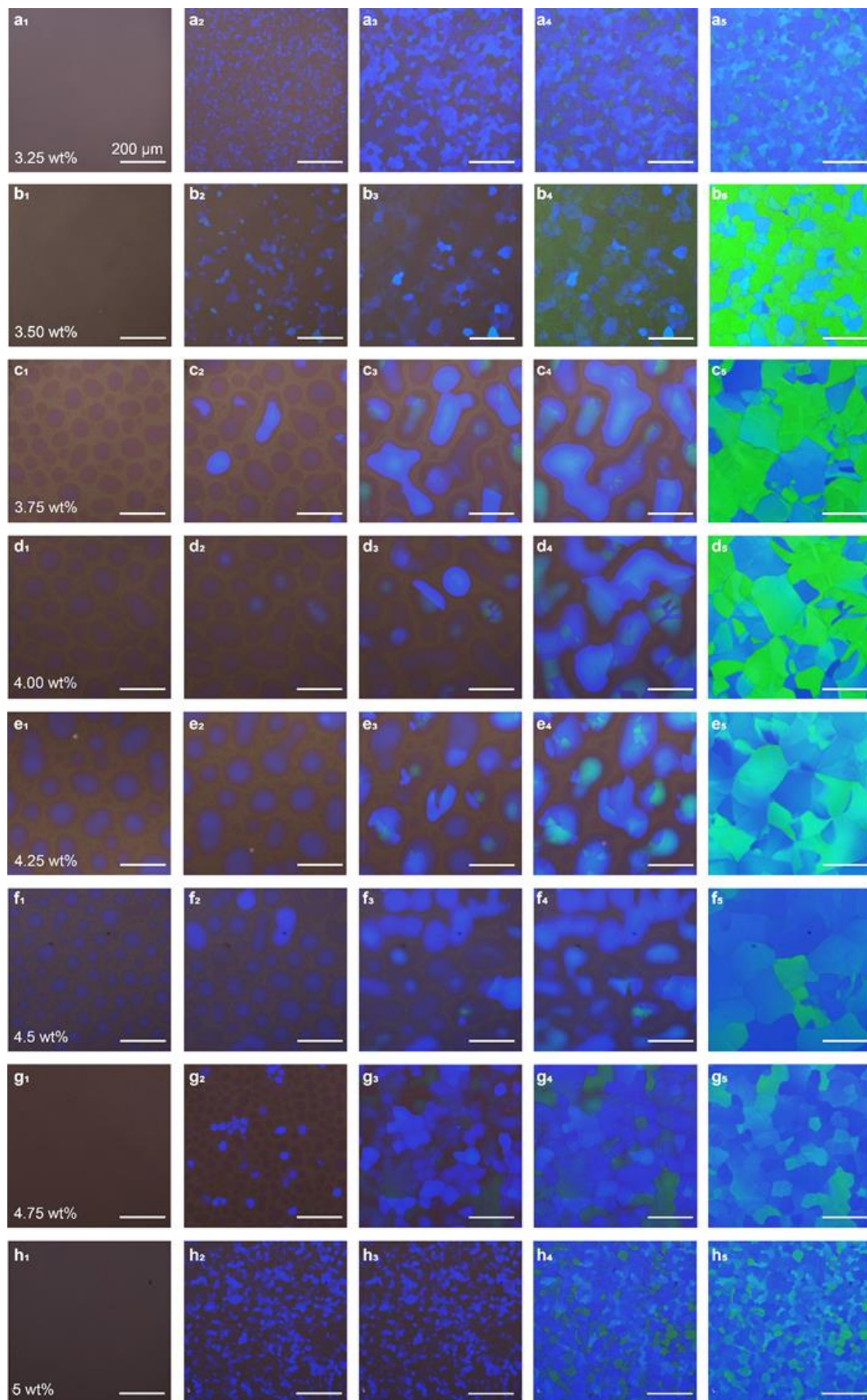
74 To gain additional insights into the phase transition process of BPLCs, detailed  
75 information was captured using POM focused on one domain of poly-domain BPLCs when  
76 cooling from 78.1 to 73.7 °C (from Stage I to IV) at a rate of 0.05 °C/min. At 74.8 °C, BPII  
77 disappears suddenly, and the transformation from BPI to the chiral nematic phase occurs at  
78 73.7 °C. The BPI temperature window  $T_{BPI}$  is 3.9 °C from 77.7 °C to 73.7 °C (without  
79 considering the coexistence of BPI/N\*).

80



81  
 82 **Supplementary Fig. 2** Kossel diagram of  $BP II_{\{100\}}$  (the label of  $BP II_{\{100\}}$  denotes that the  $BP II$  domain with  
 83  $\{100\}$  crystal planes parallel to the substrates) at Stage II and  $BP I_{\{110\}}$  at Stage V.  
 84

85 In Stage II,  $BP II$  nucleates in  $BP III$  forming  $BP III/BP II$  core-shell configurations. The  
 86 Kossel diagram shows a circle pattern along  $[100]$  direction of  $BP II_{\{100\}}$  in  $BP III/BP II$  core-  
 87 shell configurations (a). In Stage V, all  $BP II$  and  $BP III$  transfer to  $BP I$ . The Kossel diagram  
 88 shows a diamond-shaped pattern along  $[110]$  direction of  $BP I$  (b).  
 89

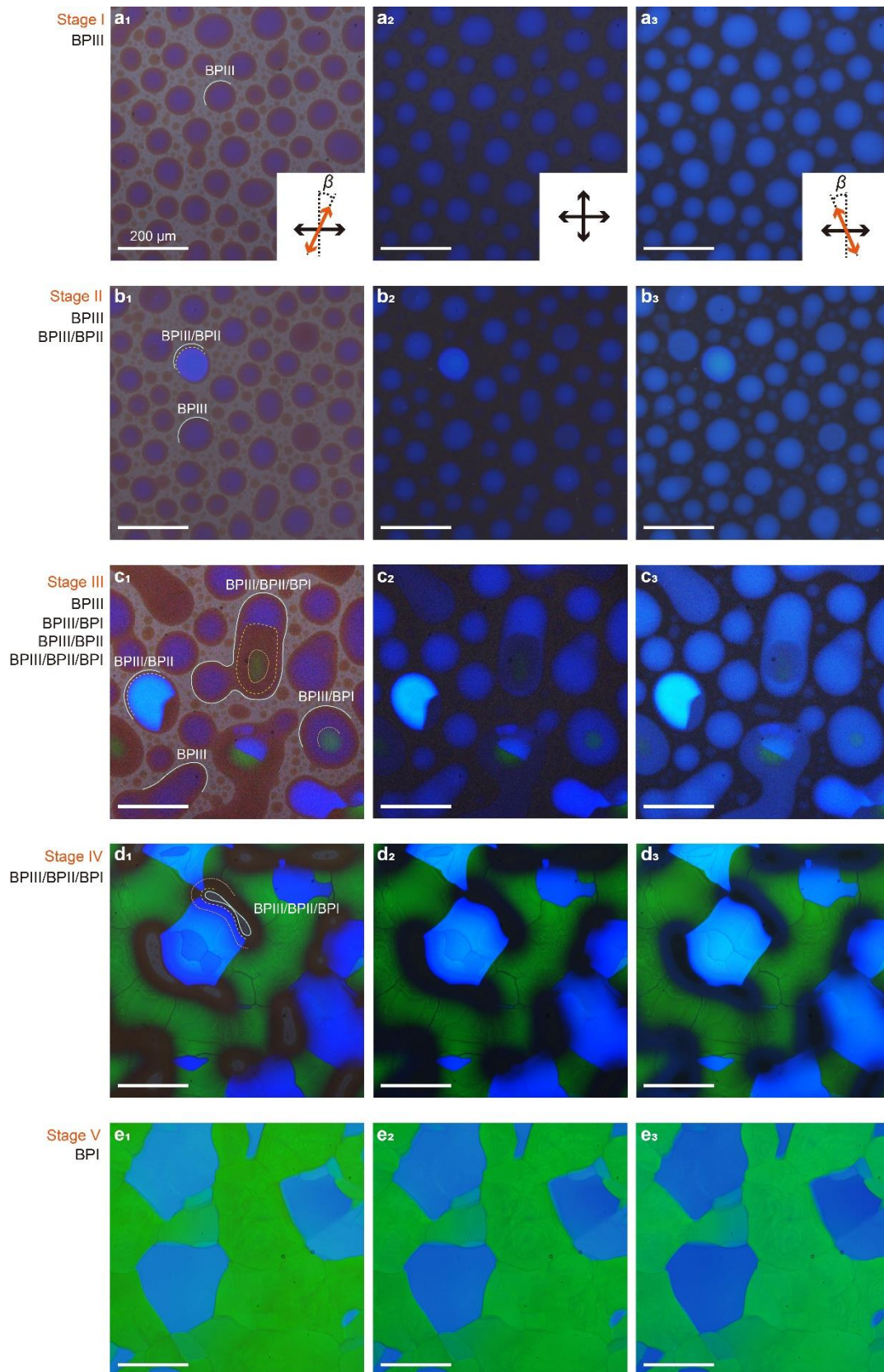


90  
91  
92  
93  
94  
95

**Supplementary Fig. 3** POM observation of phase transition behavior of BPLCs with a varying dosage of cross-linker: TMPTA. The dosage of TMPTA varies from 3.25 to 5.00 wt% where (a<sub>1</sub>-a<sub>5</sub>) 3.25 wt%, (b<sub>1</sub>-b<sub>5</sub>) 3.50 wt%, (c<sub>1</sub>-c<sub>5</sub>) 3.75 wt%, (d<sub>1</sub>-d<sub>5</sub>) 4.00 wt%, (e<sub>1</sub>-e<sub>5</sub>) 4.25 wt%, (f<sub>1</sub>-f<sub>5</sub>) 4.50 wt%, (g<sub>1</sub>-g<sub>5</sub>) 4.75 wt% and (h<sub>1</sub>-h<sub>5</sub>) 5.00 wt%.

96 Large-scale POM observation of phase transformation from BPIII to BPI during the  
97 cooling process from the isotropic state at 0.05°C/min is presented when varying the dosage of  
98 TMPTA. BPLCs with large domain sizes are obtained when the dosage of TMPTA is between  
99 3.75 and 4.5 wt% which tends to form typical five stages (see Figure 1 in the main text). When  
100 the dosage of TMPTA is over 4.75 wt% or below 3.50 wt%, the size of the core-shell  
101 configuration is greatly reduced, resulting in the connection of BPIII/BPII core-shell  
102 configurations (a, g and h). In this case, no BPI can directly nucleate in the BPIII domain,  
103 resulting in the vanishing of BPIII/BPI core-shell configuration of Stage III.  
104





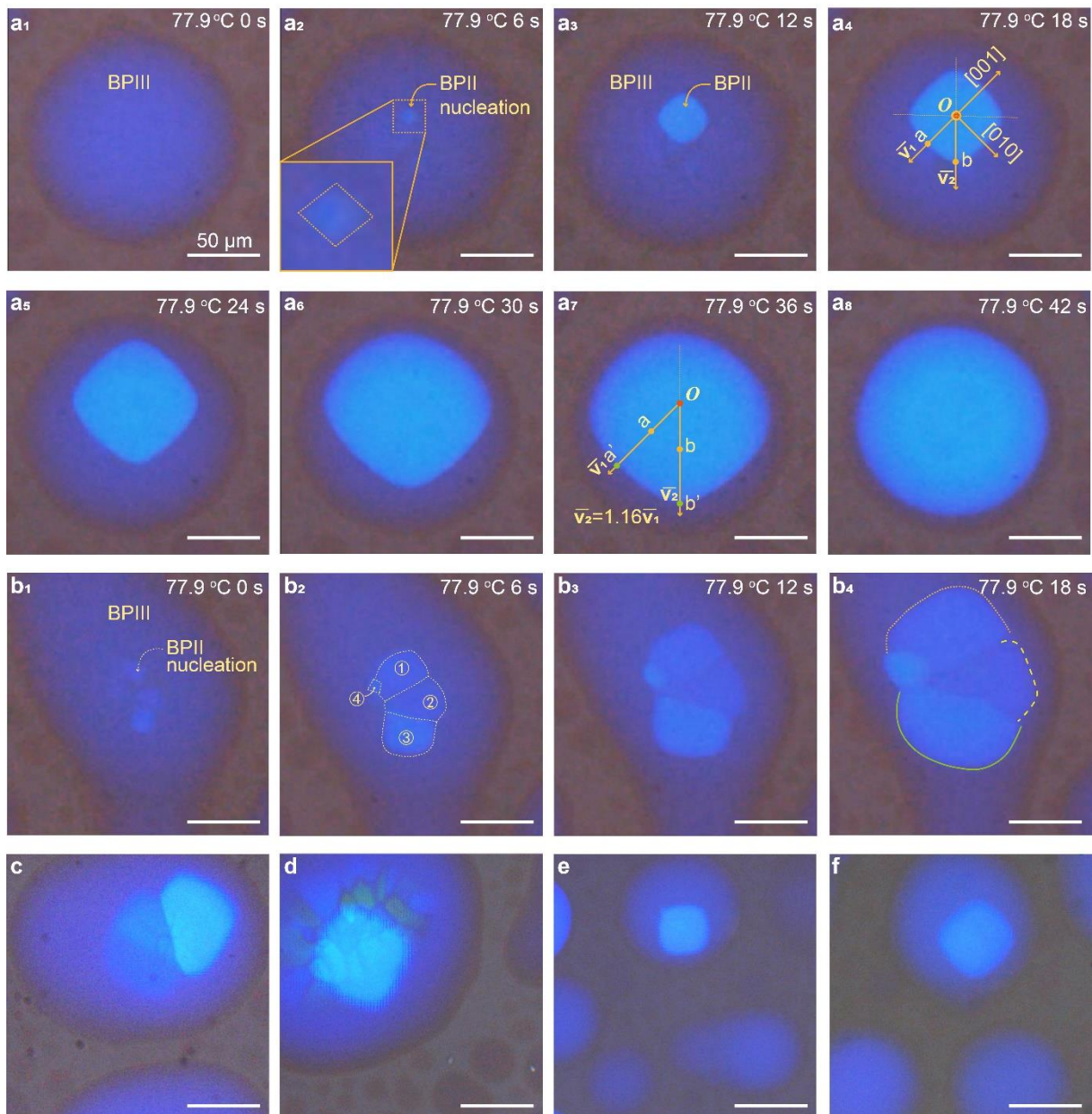
105

106 **Supplementary Fig. 4** POM observation of core-shell configuration from each stage. POM images of  
 107 (a<sub>1</sub>-a<sub>3</sub>) Stage I, (b<sub>1</sub>-b<sub>3</sub>) Stage II, (c<sub>1</sub>-c<sub>3</sub>) Stage III, (d<sub>1</sub>-d<sub>3</sub>) Stage IV, and (e<sub>1</sub>-e<sub>3</sub>) Stage V before polymerization.  
 108 Arrows inserted in POM images of (a<sub>1</sub>-a<sub>3</sub>) represent the optic axes of polarizers and the deviation angle  
 109  $\beta = \pm 4^\circ$ . The solid bright blue circle, the yellow dotted circle, and the orange dotted line in (a<sub>1</sub>-d<sub>1</sub>) highlight  
 110 BPII, BPII, and BPI domains respectively.

111 According to previous works, BPIII could be conveniently distinguished from the isotropic  
112 state due to its optical activity which renders different colors (yellowish-brown and dark blue)  
113 when the analyzer of a POM is rotated slightly (deviation angle ( $\beta$ ) of  $4^\circ$  is adopted here) to the  
114 left or right<sup>1-3</sup>. As shown in (a<sub>1</sub>), the BPIII domain with dark blue color nucleates in the isotropic  
115 background during the cooling process. Dark blue is the typical color of BPIII in POM images  
116 with an analyzer rotated slightly left (a<sub>1</sub>, b<sub>1</sub>). In (b<sub>1</sub>), the domain with dark blue is BPIII where  
117 the boundary of BPIII is labeled by a solid bright blue line. The domain of BPII is highlighted  
118 by a dotted yellow circle, which is covered by the dark brown shell of BPIII, forming a  
119 BPIII/BPII core-shell configuration. In (c<sub>1</sub>), three kinds of core-shell configurations of  
120 BPIII/BPI, BPIII/BPII, and BPIII/BPII/BPI, as well as monophasic BPIII domain, are labeled.  
121 It is noteworthy that the brown domain circled by the yellow dash line in the BPIII/BPII/BPI  
122 core-shell configuration refers to the BPII with non {100} crystal plane parallel to substrates,  
123 while the bright blue domain highlighted by the yellow dash line in BPIII/BPII domain is  
124 BPII<sub>{100}</sub>. It is convinced not only BPIII could be distinguished from the isotropic state but also  
125 BPII with non {100} crystal plane parallel to substrates could be distinguished from core-shell  
126 configurations by rotating analyzer of POM slightly to the left or right. In (d<sub>1</sub>), All the core-  
127 shell configurations of BPIII/BPI and BPIII/BPII transfer to BPIII/BPII/BPI (Stage IV). In (e<sub>1</sub>),  
128 all the brown and bright blue areas vanish, proving that BPIII and BPII completely transfer to  
129 BPI (Stage V).

130

131



132  
133  
134  
135  
136

**Supplementary Fig. 5 Nuclei and anisotropy growth of BPII in BPIII.** **a<sub>1</sub>-a<sub>8</sub>** One nuclei site of BPII in the BPIII domain. **b<sub>1</sub>-b<sub>4</sub>** Four nuclei sites of BPII in the BPIII domain. **c-f** Other examples of anisotropy growth of BPII in BPIII. The lines in B<sub>2</sub> and B<sub>4</sub> highlight the BPII grows from the four nuclei..

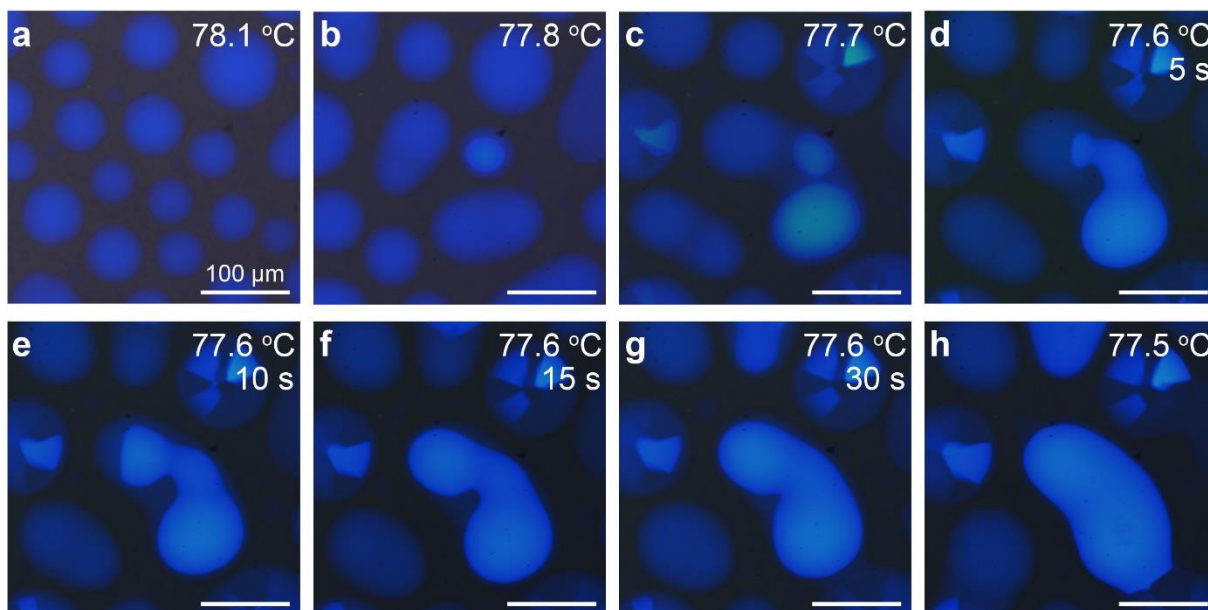
137 During the BPIII→BPII phase transition process, BPII nucleates in the center of BPIII as  
138 shown in (a<sub>2</sub>) and (b<sub>1</sub>). The nuclei of BPII<sub>(100)</sub> have a rounded square shape (inserted image of  
139 a<sub>2</sub>). Then, BPII<sub>(100)</sub> grows up adiabatically and the growth rate is anisotropy where  $\vec{v}_2$  along  
140 [011] crystal direction (2.25 μm/s) is faster than  $\vec{v}_1$  along [001] crystal direction (1.93 μm/s),  
141 giving the relationship of  $\vec{v}_2=1.16\vec{v}_1$ . This relationship slightly derives from theoretical  
142  $\vec{v}_2=\sqrt{2}\vec{v}_1$  owing to the shape of nuclei is a rounded square. It is noticeable that the growth of

143 BPII<sub>{100}</sub> is not isotropy with a spherical shape which is predicted by simulation<sup>4</sup>. When there  
144 are more than one nuclei of BPII<sub>{100}</sub> in a BPIII domain (b<sub>1</sub>-b<sub>4</sub>), each nucleus grows  
145 anisotropically with a rounded square shape. More experiments further support that the  
146 anisotropy growth of BPII<sub>{100}</sub> in the BPIII domains (c-f). Besides, there is no BPII nucleus  
147 directly in the isotropic state without the pre-formed BPIII domain.

148

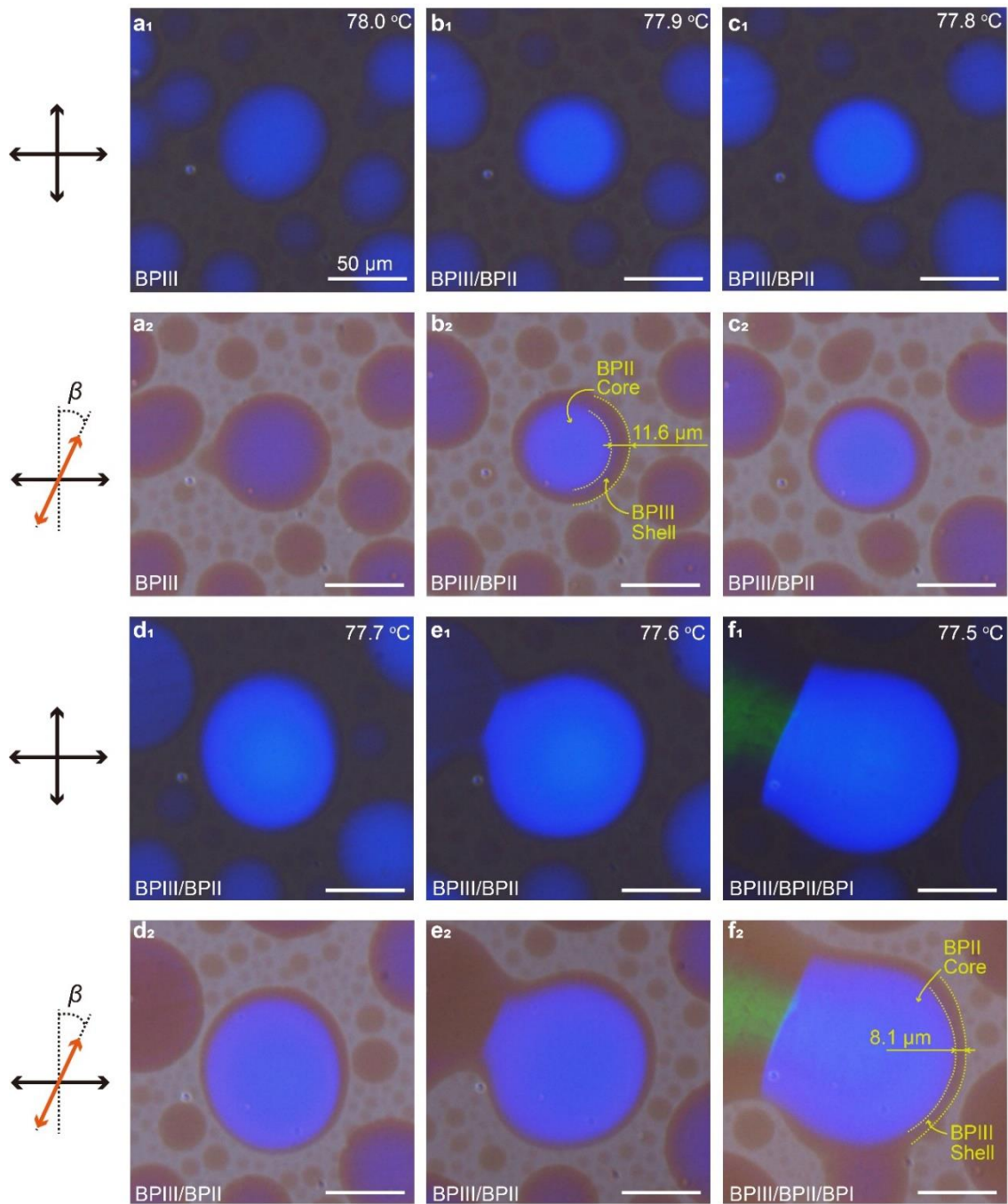
149

150



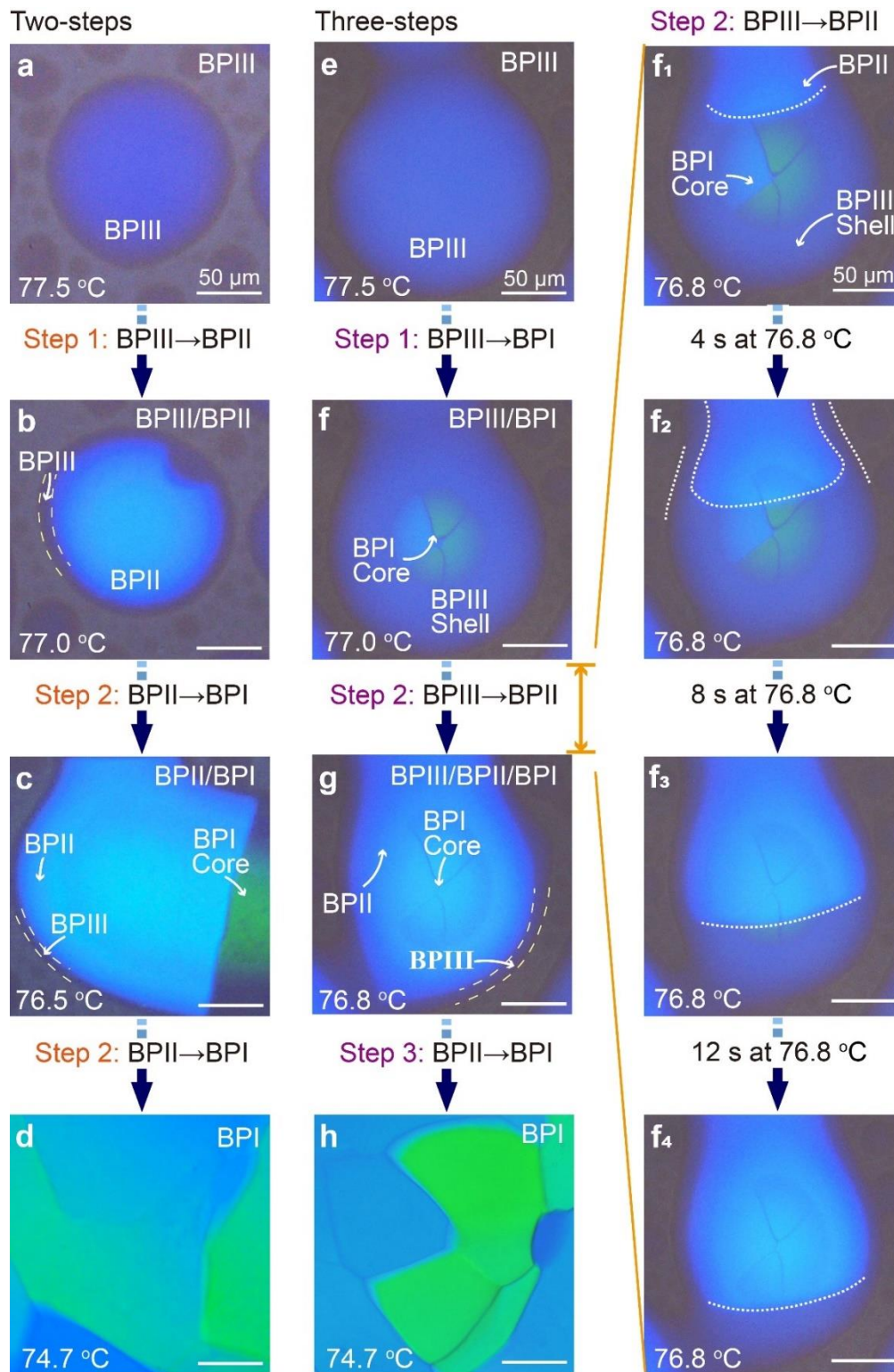
151  
 152 **Supplementary Fig. 6 POM characterization of diffusionless phase transition (DLPT) from BPIII to**  
 153 **BPII. a** Typical textures of Stage I. **b, c** BPII nucleates in the center of the BPIII domain during the  
 154 temperature reduction process. **d-g** Rapid growth with spreading behavior when the temperature is kept at  
 155 77.6 °C for 30 s. **h** BPII core and BPIII shell grow up spontaneously during the decreasing temperature  
 156 process.  
 157

158 The phase transition from BPIII to BPII (equally to Stage I to II) is considered as a DLPT  
 159 process where clear boundaries and spreading behavior are observed by POM. The textures  
 160 were captured during temperature reduction from 78.1 to 77.5 °C at a cooling rate of  
 161 0.01 °C/min, in which the rapid growth of BPII is observed with spreading behavior when the  
 162 temperature is kept at 77.6 °C for 30 s. BPII starts to nucleate in the center of BPIII at 77.8 °C  
 163 (b) and the number of BPII crystal nucleus increases during the temperature reduction process  
 164 (c). When the temperature is kept at 77.6 °C for 30 s, the as-formed nuclei of BPII grow from  
 165 the right-bottom part toward the left-up part (d-g), and the two nuclei merge into one BPII  
 166 domain (c-d). The full size of the BPII domain is limited by the size of BPIII.  
 167



168  
 169 **Supplementary Fig. 7 POM characterization of formation and evolution of BPIII/BPII core-shell**  
 170 **configuration.** POM images of (a<sub>1</sub>-a<sub>2</sub>) BPIII domain, (b-e) BPIII/BPII core-shell configuration, (f<sub>1</sub>-f<sub>2</sub>)  
 171 Transformation from BPIII/BPII core-shell configuration to BPIII/BPII/BPI core-shell configuration. Red  
 172 arrows on the left of POM images represent the optic axes of polarizers and the deviation angle  $\beta = \pm 4^\circ$ .  
 173

174 After the formation of BPIII/BPII core-shell configuration through nuclei and anisotropy  
 175 growth process (Supplementary Fig. 5), the domain with BPIII/BPII core-shell configuration  
 176 grows up spontaneously during the cooling process (b-e). Notably, the ratio between BPIII and  
 177 BPII has changed, that is BPIII shell gradually becomes thinner from 11.6  $\mu\text{m}$  (b) to 8.1  $\mu\text{m}$  (f).



178  
179  
180  
181  
182  
183  
184  
185  
186  
187  
188

**Supplementary Fig. 8 POM characterization of the two-, three-step successive DLPT of BPLCs.** a-d Two-step process: (a) BPIII domain in Stage I, (b) BPIII/BPII core-shell configuration in Stage II & III obtained by DLPT from BPIII to BPII, (c) BPIII/BPII/BPI core-shell configuration in Stage III & IV, and (d) polydomain BPI in Stage V obtained by thermoelastic martensitic transformation from BPII to BPI. e-h Three-step process: (e) BPIII domain in Stage I, (f) BPIII/BPI core-shell configuration in Stage III obtained by DLPT from BPIII to BPI, (g) BPIII/BPII/BPI core-shell configuration in Stage III & IV obtained by DLPT from BPIII to BPII and (h) polydomain BPI in Stage V obtained by thermoelastic martensitic transformation from BPII to BPI. f<sub>1</sub>-f<sub>4</sub> Detailed characterization of BPIII→BPII transformation from BPIII/BPI to BPIII/BPII/BPI core-shell configuration.

189 During phase transition from Stage I to V, there exist three kinds of core-shell  
190 configurations: (i) BPIII/BPII configurations (BPII covered by a thin shell of BPIII) (b); (ii)  
191 BPIII/BPII/BPI core-shell configurations (BPI covered by BPII and BPIII sequentially) (c, g);  
192 (iii) BPIII/BPI core-shell configurations (BPI covered by BPIII) (f).

193 In BPLCs, BPIII-to-BPII, BPIII-to-BPI, and BPII-to-BPI are DLPT processes, in which  
194 two- or three-step successive phase transformation is observed. In a two-step process (a-d),  
195 BPLCs firstly form a BPIII/BPII core-shell configuration in Stage II (Step 1: DLPT of  
196 BPIII→BPII), and then BPI nucleates and grows in BPII in Stage III forming a BPIII/BPII/BPI  
197 core-shell configuration (Step 2: the thermoelastic martensitic transformation of BPII-to-BPI).

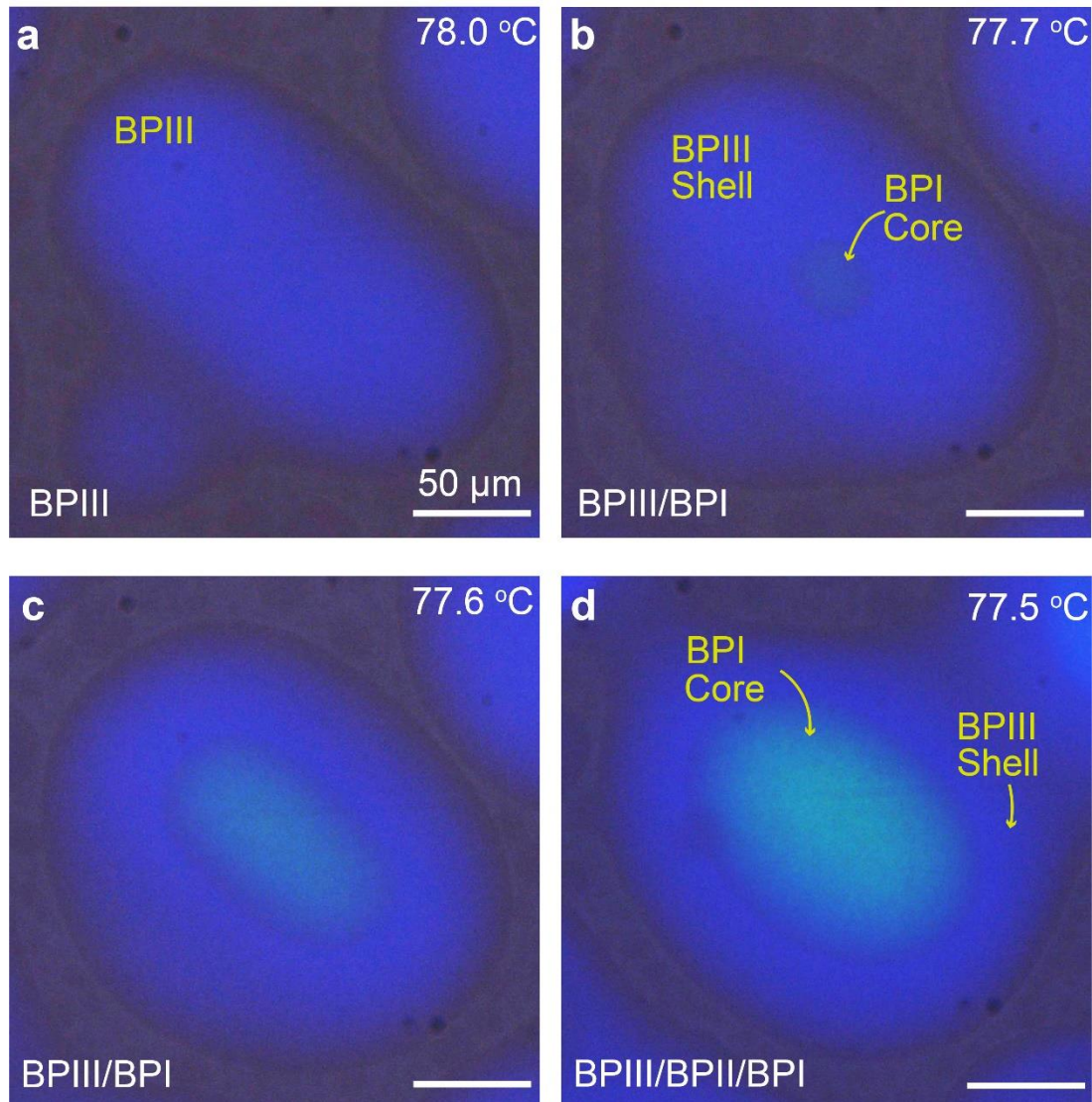
198 In a three-step process, BPI firstly nucleates in the center of the BPIII domain in Stage III  
199 (Step 1: DLPT of BPIII-to-BPI), then part of BPIII shell transfers to BPII (Step 2: DLPT of  
200 BPIII-to-BPII). BPI core grows with the decreasing temperature until BPII completely transfers  
201 to BPI (Step 3: the thermoelastic martensitic transformation of BPII-to-BPI).

202 This two-step successive DLPT is rarely investigated in soft matter or atomic crystals.

203

204





206

207

208

209

210

211

212

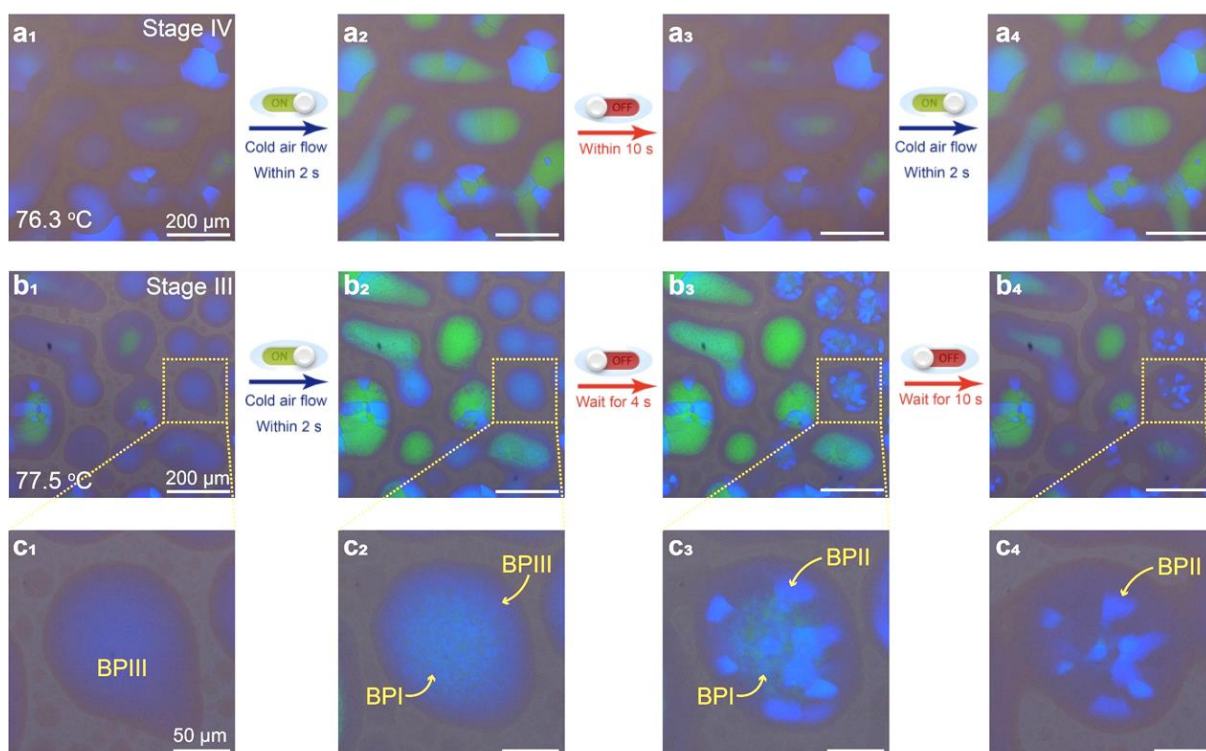
213

214

215

**Supplementary Fig. 9 POM characterization of the formation process of BPIII/BPI core-shell configuration. a** BPIII domain. **b-d** Growth of BPI in BPIII toward the formation of BPIII/BPI core-shell configuration.

In this work, BPI can transfer from BPIII directly without the pre-formed BPII, forming a BPIII/BPI core-shell configuration (b-d). It is found that this process is widely observed in polydomain BPLCs with a large domain size of over 150  $\mu\text{m}$ . The direct phase transformation from BPIII to BPI is observed earlier than the transformation from BPIII to BPII.

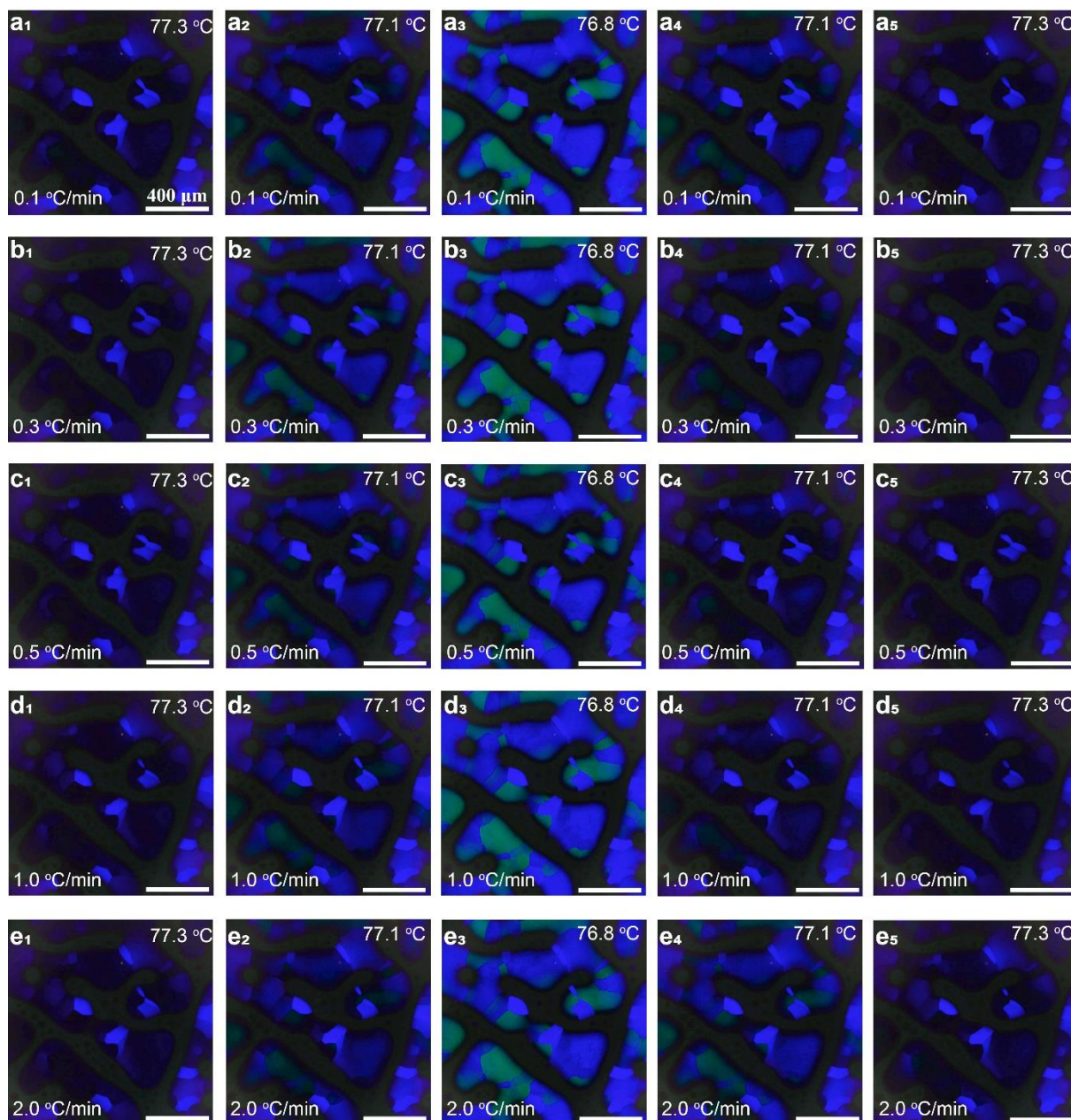


216  
 217 **Supplementary Fig. 10 POM observation of speed and reversibility of DLPT between BPI and BPII at**  
 218 **Stage III or IV. a<sub>1</sub>-a<sub>4</sub>** Textures of Stage IV with the temperature of the hot stage at 76.3 °C upon flowing or  
 219 stop flowing color air for the same region. **a<sub>1</sub>** The original state of Stage IV. **a<sub>2</sub>** A phase transition occurs  
 220 within 2 s from BPII to BPI after flowing cold air. **a<sub>3</sub>** The BPI in BPIII/BPII/BPI core-shell configuration  
 221 transfer back to BPII after stopping flowing cold air for 10 s. **a<sub>4</sub>** The phase transition from BPII in  
 222 BPIII/BPII/BPI core-shell configuration to BPI within 2 s upon flowing cold air. **b<sub>1</sub>-b<sub>4</sub>** Textures of Stage III  
 223 when the temperature of the hot stage is kept at 77.5 °C with or without flowing or stop flowing cold air. **b<sub>1</sub>**  
 224 The original state of Stage IV. **b<sub>2</sub>** The phase transition from BPIII domain to BPIII/BPII core-shell  
 225 configurations or from BPII in BPIII/BPII/BPI core-shell configurations to BPI after flowing cold air within  
 226 2 s. **b<sub>3</sub>** The BPII appears between the BPIII and BPI in BPIII/BPI core-shell configurations in **b<sub>2</sub>** after stopping  
 227 flowing cold air for 4 s. **b<sub>4</sub>** The BPI in BPIII/BPII/BPI core-shell configuration transfer back to BPII after  
 228 stopping flowing cold air for 10 s. **c<sub>1</sub>-c<sub>4</sub>** Enlarged images of the area highlighted by yellow dotted squares in  
 229 **b<sub>1</sub>-b<sub>4</sub>**.  
 230

231 The DLPT between BPII to BPI is rapid and completely reversible which are the two  
 232 significant characteristics of thermoelastic martensitic transformation (a<sub>1</sub>-a<sub>4</sub>). Herein, the  
 233 transformation from BPII in BPIII/BPII/BPI core-shell configurations to BPI takes place within  
 234 2 s when the temperature of the upper surface of the LC cell is slightly reduced by flowing cold  
 235 air. Reversibly, the transformation from BPI in BPIII/BPII/BPI core-shell configurations to  
 236 BPII takes place within 10 s when the temperature of the upper surface of the LC cell recovers  
 237 to the original state by stopping flowing cold air. It demonstrated high reversibility with more  
 238 than 50 conversion-reversion cycles (Movie 2), indicating little temperature hysteresis for the  
 239 DLPT between BPII and BPI. In (b<sub>1</sub>-b<sub>2</sub>), the framed part of the POM image is BPIII domains,

240 and transformation from BPIII domains to BPIII/BPI core-shell configurations take place  
241 within 2 s when the temperature of the upper surface of the LC cell is slightly reduced by  
242 flowing cold air ( $b_2$ ), BPI appears in the center of BPIII. After stopped cold air for 4 s, the BPIII  
243 appears between the BPIII shell and BPI core, resulting in all the BPIII/BPI core-shell  
244 configurations convert to BPIII/BPII/BPI core-shell configurations ( $b_3$ ). Finally, BPI cores in  
245 BPIII/BPII/BPI core-shell configurations transfer to BPII ( $b_4$ ) after stopping flowing cold air  
246 for 10 s. It is confirmed that the phase transformation between BPIII and BPI is not completely  
247 reversible with thermal hysteresis and the transformation between BPII and BPII is completely  
248 reversible with little hysteresis.

249



250

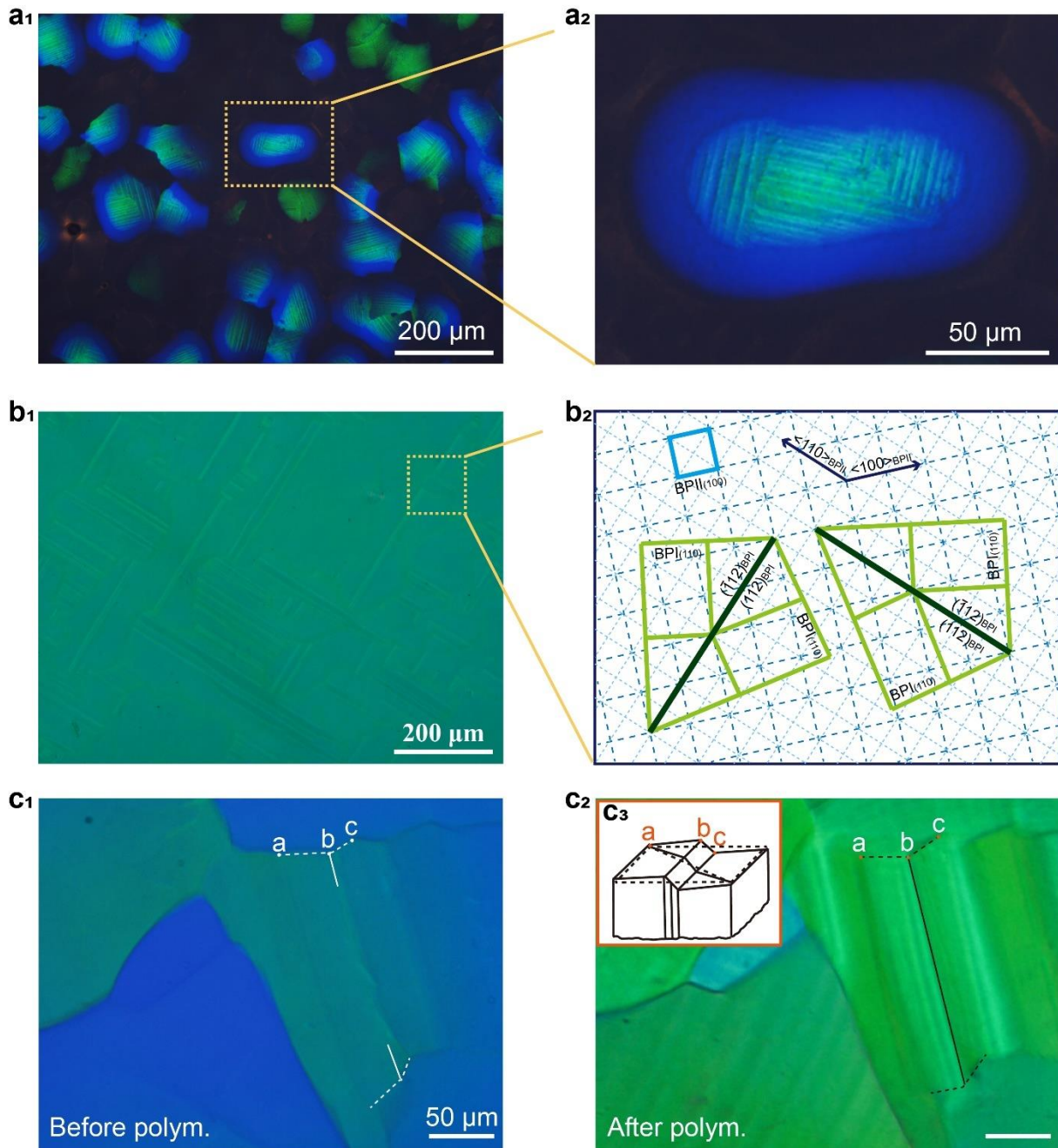
251 **Supplementary Fig. 11** Reversible thermoelastic martensitic transformation between BPII and BPI in  
 252 BPIII/BPII/BPI core-shell configurations (Stage IV) with distinct temperature change rates of (a) 0.1, (b)  
 253 0.3, (c) 0.5, (d) 1.0, and (e) 2.0 °C/min

254

255 Except for flowing the cold air over the sample, several detailed heating and cooling cycles  
 256 are performed on the BPLCs at the rates of 0.1, 0.3, 0.5, 1.0 to 2.0 °C/min to investigate the  
 257 phenomenon of hysteresis as clear as possible. The temperature is controlled by a heating stage  
 258 equipped with a liquid nitrogen cooling system. The phase transition between BPI and BPII is  
 259 proved without obvious temperature hysteresis, providing evidence of thermoelastic martensitic  
 260 transformation.

261

262



263  
 264 **Supplementary Fig. 12** Twins (a-b) and surface reliefs (c) observed during the phase transformation. **a<sub>1</sub>**  
 265 POM image taken in reflection mode. The phase transition from polydomain BPII to BPI occurs in an LC  
 266 cell composed of two bare glass substrates without any surface treatment. Cross-hatched textures, namely  
 267 twin textures, were observed in the center of the BPIII/BPII/BPI core-shell configurations, where BPI<sub>{110}</sub>  
 268 was covered by BPII<sub>{100}</sub> and then BPIII. **a<sub>2</sub>** Magnified POM image exhibiting the twin textures in  
 269 polydomain BPLCs. **b<sub>1</sub>** Twin textures observed in a monodomain BPI<sub>{110}</sub> transferred from monodomain  
 270 BPII<sub>{100}</sub>. **b<sub>2</sub>** Schematic of the BPI<sub>{110}</sub> lattice after martensitic transformation from monodomain  
 271 BPII<sub>{100}</sub>. **c<sub>1</sub>-c<sub>2</sub>** Surface reliefs of BPI<sub>{110}</sub> after phase transformation from BPII<sub>{100}</sub>. **c<sub>1</sub>** before and **c<sub>2</sub>** after  
 272 polymerization. **c<sub>3</sub>** Schematic of the surface reliefs. Before polym.' and 'after polym.' refers to before  
 273 polymerization and after polymerization  
 274  
 275

276 It is observed that the cross-hatched textures of BPI exhibit in both poly- (a<sub>1</sub>-a<sub>2</sub>) and single-  
 277 domain BPLCs (b<sub>1</sub>-b<sub>2</sub>), originating from a thermoelastic martensitic transformation from the  
 BPII<sub>{100}</sub>. As shown in (a<sub>1</sub>-a<sub>2</sub>), the cross-hatched textures appear in a BPIII/BPII/BPI core-shell

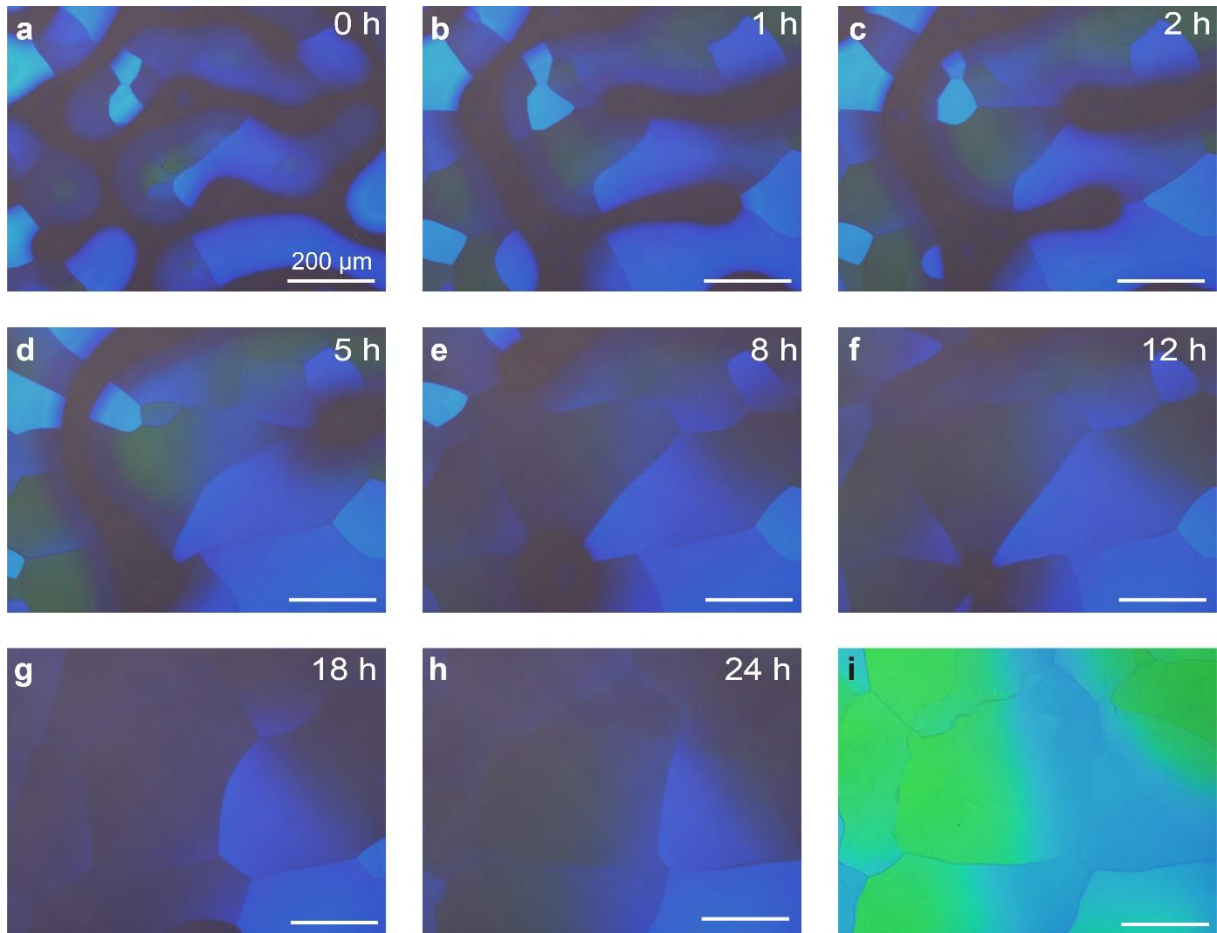
278 configuration, in which  $\text{BPI}_{\{110\}}$  (green) is covered by a  $\text{BPII}_{(100)}$  (blue). The cross-hatched  
279 textures are observed in polydomain  $\text{BPI}_{\{110\}}$  ( $a_2$ ) which transfer from  $\text{BPII}_{\{100\}}$  ( $a_1$ ). These  
280 textures are the results of strain release via twinning which is anticipated for martensitic  
281 transformation. A similar texture is observed in monodomain  $\text{BPI}_{\{110\}}$  ( $b_1$ ), in which the bands  
282 are larger than their polydomain counterparts ( $a_1$ - $a_2$ ). The alternating lamellar of the two  
283 possible configurations ( $b_1$ ) is caused by the twinning corresponding to the monodomain  
284  $\text{BPI}_{\{110\}}$  with equal proportions. The idealized arrangement of the two twin sets framed in ( $b_1$ )  
285 is shown in ( $b_2$ ), and  $\{112\}_{\text{BPI}}$  is parallel to  $\{110\}_{\text{BPII}}$  which is further confirmed by syn-SAXS  
286 (Supplemental Fig. 52). The cross-hatched textures appear due to the reduction of the average  
287 macroscopic strain of the unit cell, and the shear strain cannot be resolved through the formation  
288 of a single twin, and each twin exhibits a shear strain of the opposite direction. These  
289 neighboring bands are considered to be two variants that together relax the transformation  
290 strains ( $b$ ).

291 In addition, the surface reliefs ( $c_1$ - $c_3$ ) in  $\text{BPI}_{\{110\}}$  before ( $c_1$ ) and after ( $c_2$ ) polymerization,  
292 as characteristic properties of martensitic transformation, are observed due to the shear strain  
293 during the phase transformation from  $\text{BPI}_{\{110\}}$  to  $\text{BPII}_{\{100\}}$ . The grain consists of parallel bands  
294 and the adjacent bands are parallel to  $\{112\}_{\text{BPI}}$  ( $c_1$ - $c_3$ ).

295 The results of twinning and surface reliefs further confirm the argument that the phase  
296 transformation between  $\text{BPII}$  and  $\text{BPI}$  takes place in a diffusionless manner.

297

298

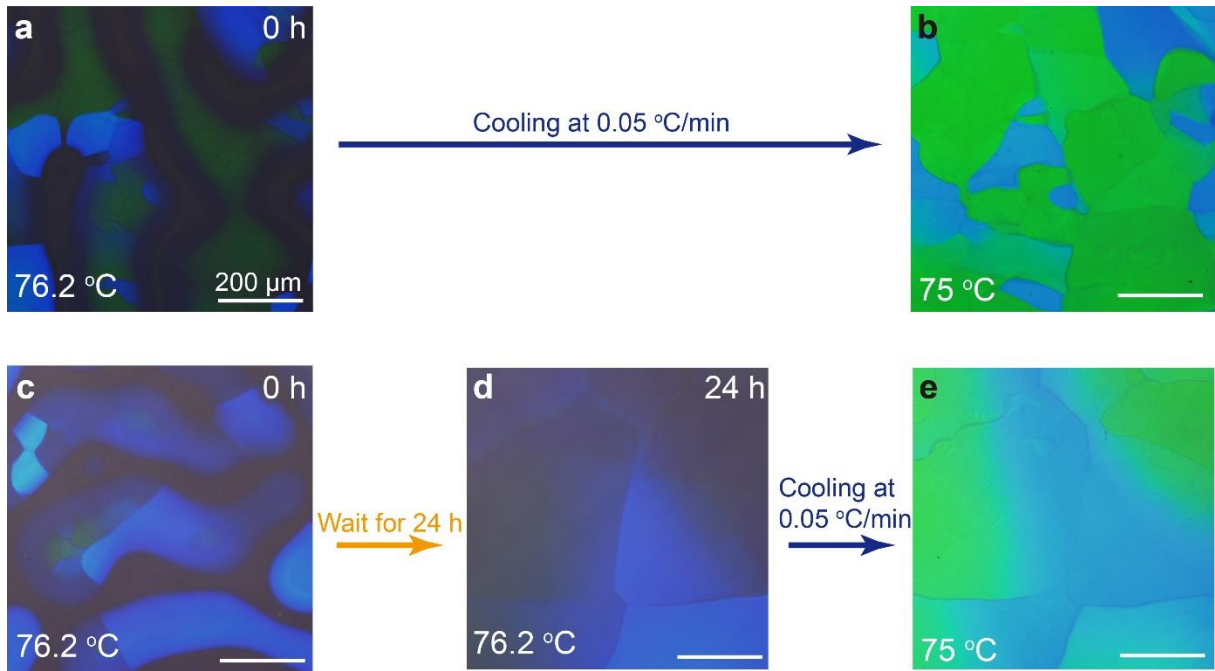


299  
300  
301  
302  
303  
304  
305  
306

**Supplementary Fig. 13 The enlargement of domain size of BPLCs at Stage IV annealed with increasing time.** **a** Optical textures of fresh-formed BPLCs by direct cooling from the isotropic state to 76.2 °C (Stage IV) at 0.05 °C/min. **b-h** Optical textures with the temperature maintained at 76.2 °C after being preserved for 1-24 h. **i** BPI obtained by cooling from (**h**) at a cooling rate of 0.05 °C/min to 74.7 °C.

307 It is observed that the number of nuclei both BPI and BP II in BP III/BP II/BPI core-shell  
308 configurations is gradually reduced (a-h) after annealing for 1-24 h at 76.2 °C. providing the  
309 possibility for enlarging the domain size of BPLCs which is considered as a significant issue to  
310 improve the performance of the devices fabricated based on BPLCs.

310

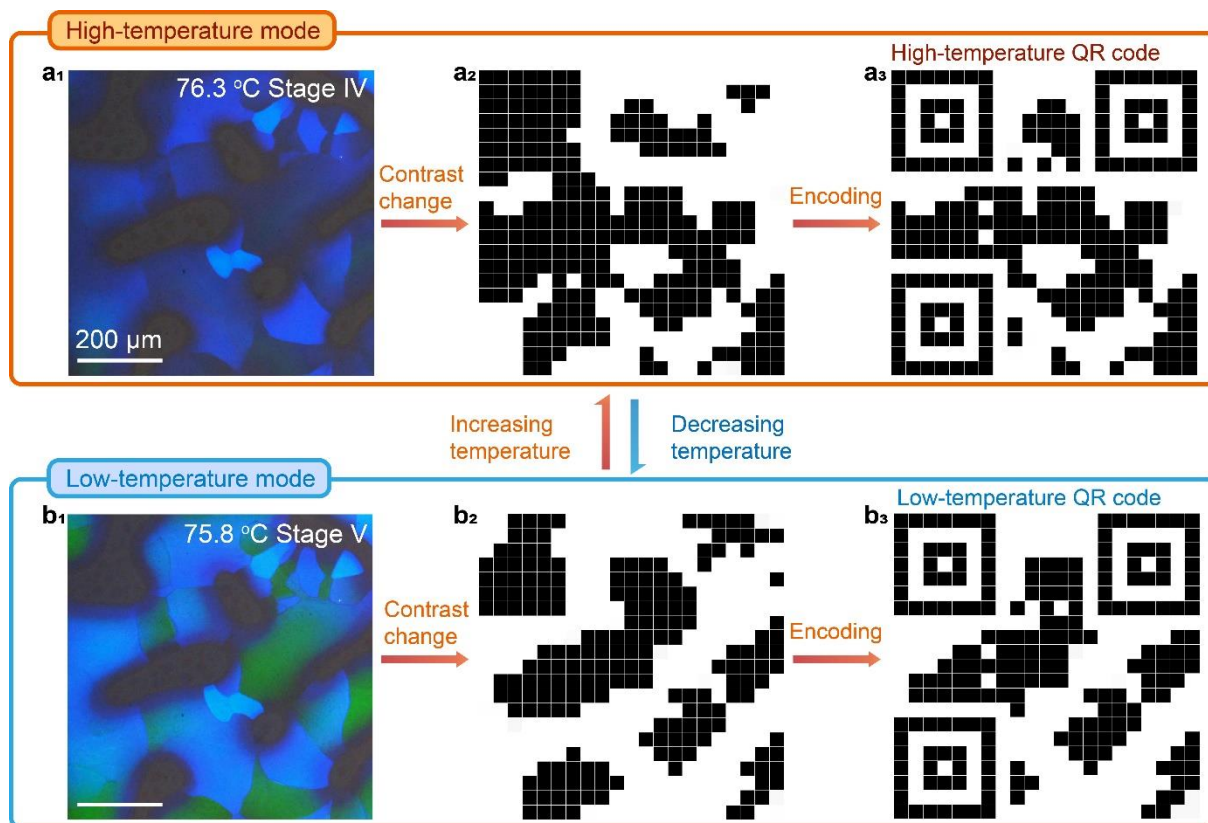


311  
 312 **Supplementary Fig. 14 Enlargement of domain size by annealing.** **a,c** BPLCs in Stage IV  
 313 (BPIII/BPII/BPI) cooled from the isotropic phase to 76.2 °C. **b** BPI obtained by further cooling the sample  
 314 from 76.2 °C (a) to 74.7 °C at 0.05 °C/min. **d** Texture mixed with BPI and BPII obtained after maintaining  
 315 the temperature for 24 h. **e** BPI with domain-size-enlarged BPLCs obtained by cooling from (d) at  
 316 0.05 °C/min.

317  
 318 It is found that the ultra-large domain size of polydomain BPI (d-e) can be obtained by  
 319 reduction of the number of nuclei (Supplementary Fig. 13) which is achieved by annealing for  
 320 24 h at 76.2 °C (c-d). Polydomain BPI with a large domain size over 1 mm (e) is obtained after  
 321 slowly cooling from the enlarged BPIII/BPII/BPI core-shell configurations (d) at 0.05 °C/min.  
 322 The BPI domain is nearly 3 times (e) larger than that without annealing (b).

323





324

325 **Supplementary Fig. 15 Temperature-switchable QR codes.** **a<sub>1</sub>-a<sub>3</sub>** High-temperature QR code. **a<sub>1</sub>** The  
 326 POM image of BPLCs at Stage IV was captured at 76.3 °C. **a<sub>2</sub>** Image obtained after gray-level conversion,  
 327 contrast change, and pixelation processes from (**a<sub>1</sub>**) according to the image brightness. **a<sub>3</sub>** A QR code with a  
 328 size of 21×21 is encoded based on (**a<sub>2</sub>**). **b<sub>1</sub>-b<sub>3</sub>** Low-temperature QR code. **b<sub>1</sub>** POM image of BPLCs Stage  
 329 IV was captured at 75.8 °C. **b<sub>2</sub>** Image obtained from (**b<sub>1</sub>**) according to the image brightness. **b<sub>3</sub>** A QR code  
 330 with a size of 21×21 is encoded based on (**b<sub>2</sub>**).  
 331

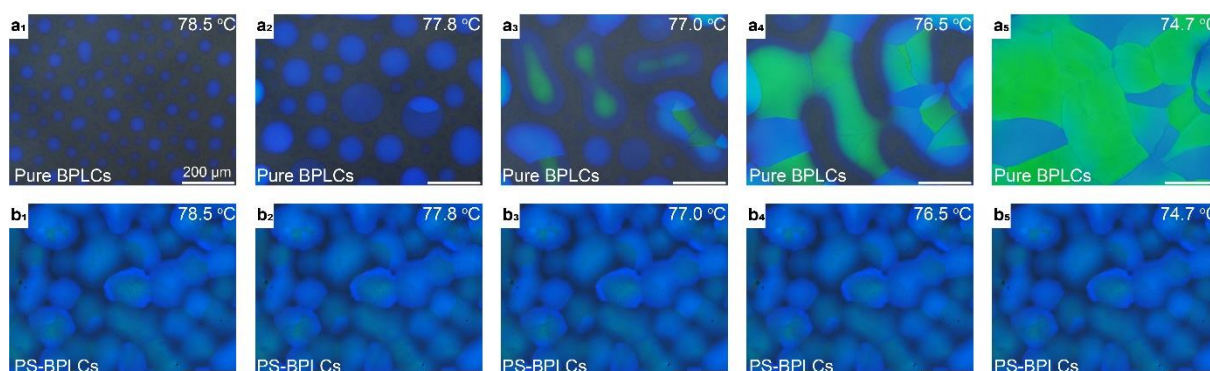
332 Due to the rapid and completely reversible properties of thermoelastic martensitic  
 333 transformation between BPII and BPI, the reversible switching of POM images are achieved at  
 334 high and low temperatures (**a<sub>1</sub>**, **b<sub>1</sub>**). This reversible storage of patterns in soft BPLCs can be  
 335 considered as an analogy to the shape-memory in solid-solid crystal transformation. The  
 336 temperature-switchable QR codes undergo the processes (Supplementary Figs. 4a-b) of gray-  
 337 level conversion, contrast change, pixelation (**a<sub>2</sub>**, **b<sub>2</sub>**), and encoding (**a<sub>3</sub>**, **b<sub>3</sub>**). Thus, the POM and  
 338 corresponding QR codes obtained at high-temperature mode (76.3 °C) with particular  
 339 information are unique in different samples or cooling circles. During the fast cooling process  
 340 from 76.3 °C to 75.8 °C at 1 °C/min, the BPI in BPIII/BPII/BPI core-shell configurations grows  
 341 up fast and leads to an increase of brightness and changing of colors of the POM image (**b<sub>1</sub>**). A  
 342 coupled QR code is obtained (**b<sub>2</sub>-b<sub>3</sub>**) at low-temperature. When the sample is heated from 75.8 °C

343 to 76.3 °C, a completely reverse transformation from BPI in BPIII/BPII/BPI core-shell  
344 configurations to BPII occurs by gradual reduction of the existing BPI. Finally, almost all BPI  
345 are converted into BPII and the distribution of core-shell configurations is recovered to the  
346 original high-temperature mode, resulting in the recovered QR code is the same as the initial  
347 one obtained before the first cooling circle. Thus, a pair of QR codes achieved at high/low  
348 temperatures can be switched reversibly with high duration stability (Movie 2). The switchable  
349 QR code has higher security than static QR code.

350

351

352 **Supplementary Note 3 Thermal stability of PS-BPLCs**



353 **Supplementary Fig. 16** Textures varied with temperature when cooled from 80.0 °C (the isotropic  
354 state for BPLCs) to 74.7 °C (BPI, StageV) at a rate of 0.05 °C/min. a<sub>1</sub>-a<sub>5</sub> BPLCs exhibit DLPT  
355 properties. b<sub>1</sub>-b<sub>5</sub> PS-BPLCs exhibit no changes.  
356  
357

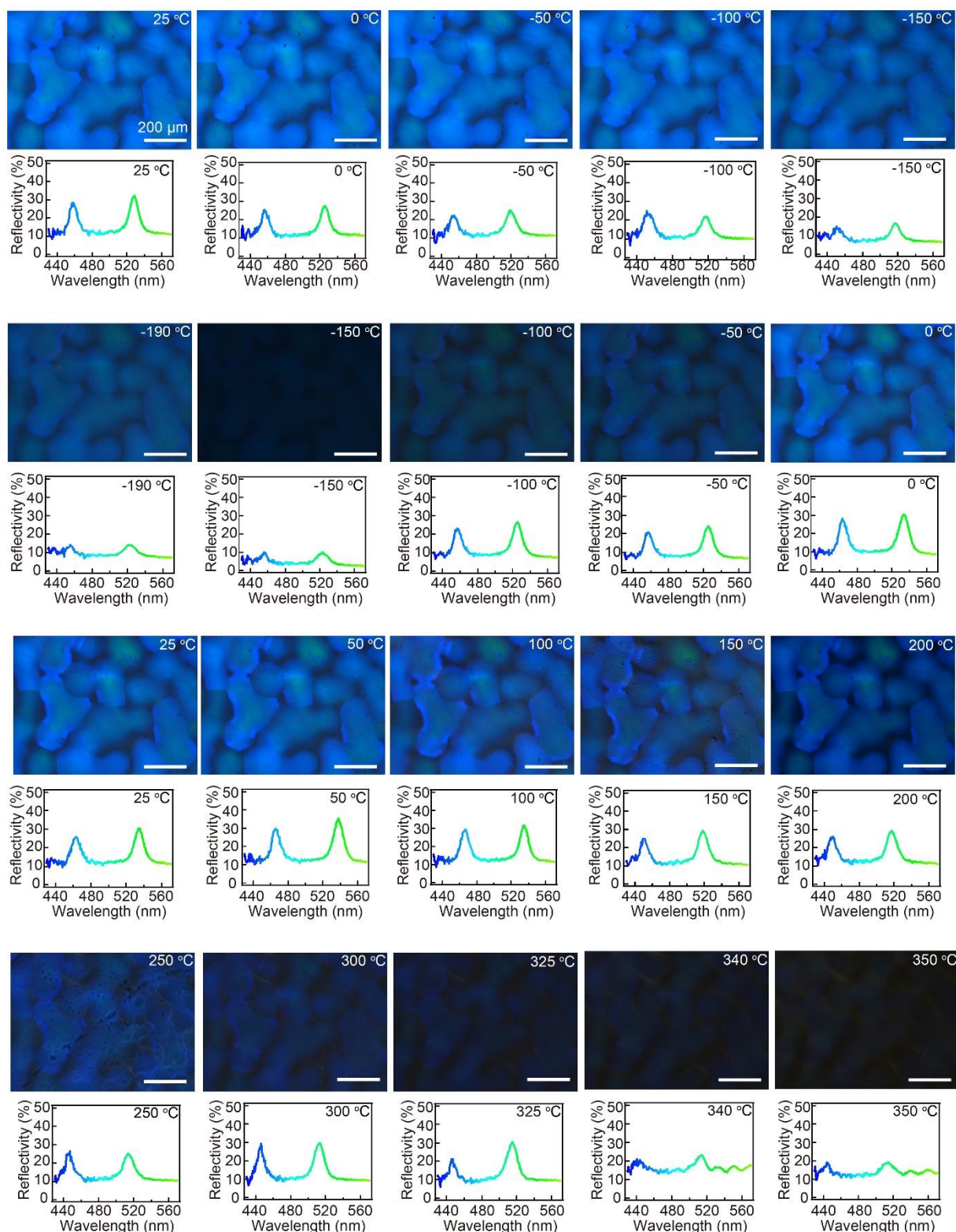
358 The BPLCs that have DLPT properties are not photopolymerized (a<sub>1</sub>-a<sub>5</sub>) which sequentially  
359 show the typical five stages. However, the mixed liquid crystal component contains reactive  
360 monomers and initiators, which can be photopolymerized to stabilize the structures of coexisted  
361 BPLCs for detailed investigation of DLPT. Once the BPLCs are photopolymerized, the PS-  
362 BPLCs in obtained which the phase transition process cannot occur (b<sub>1</sub>-b<sub>5</sub>).

363

364

365

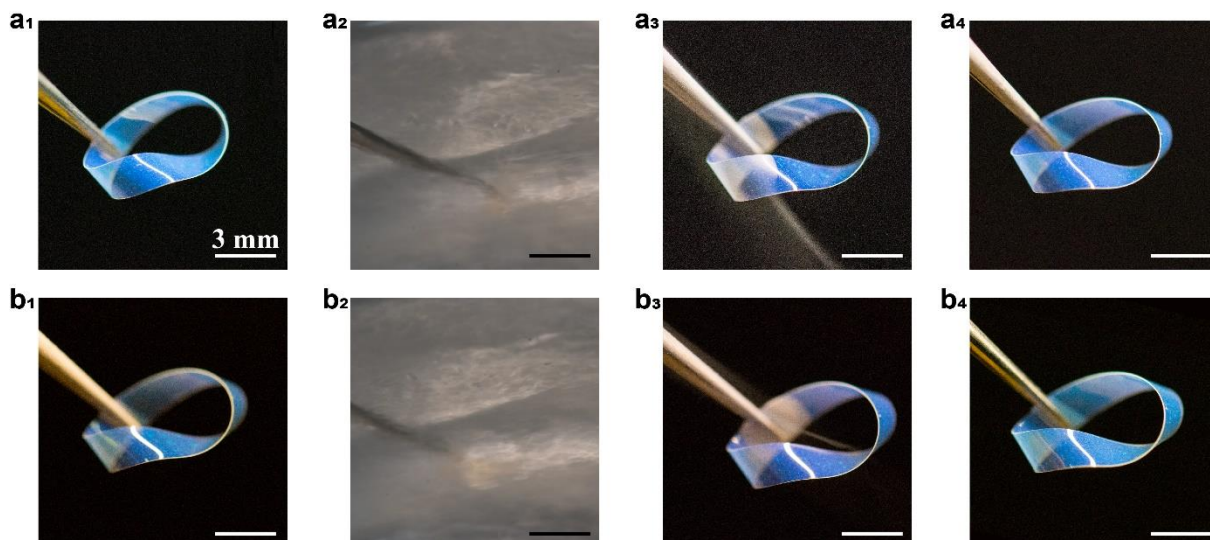
366



367  
 368 **Supplementary Fig. 17 Thermal stability of PS-BPLCs in Stage IV (BPIII/BPII/BPI core-shell**  
 369 **configuration).** POM images indicate the range of thermal stability of PS-BPLCs in Stage IV, from -190 to  
 370 350 °C. The corresponding reflection spectra are shown behind the POM images.

371  
 372 In this work, the temperature window of PS-BPLCs is identified by firstly cooling the  
 373 samples from 25 to -190 °C at a cooling rate of 5 °C/min and then heating them to 350 °C at a  
 374 heating rate of 5 °C/min. Temperature-dependent POM images and reflection spectra of the

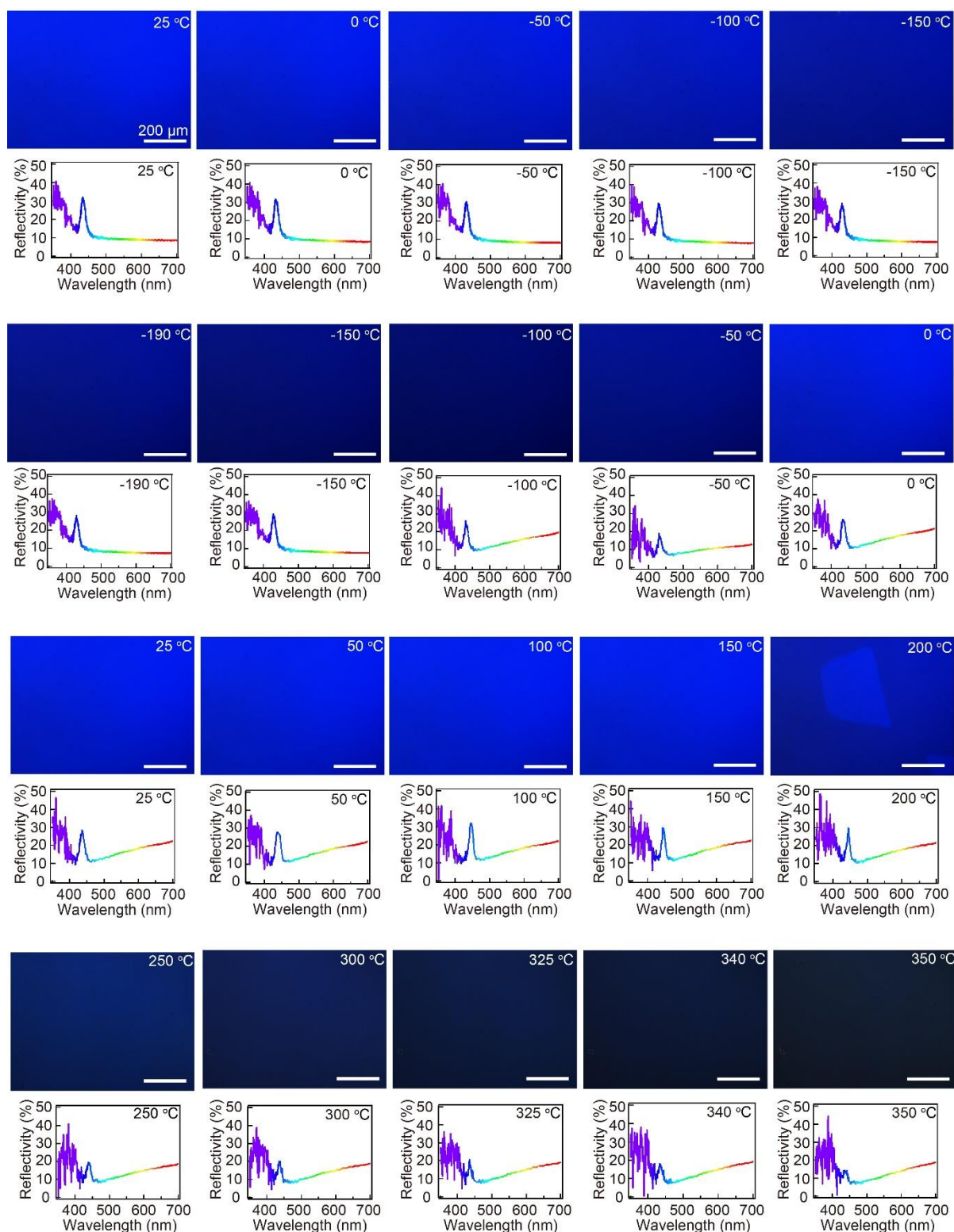
375 sample in Stage IV are shown. The reflectivity is reduced at the lower (close to -190 °C) or  
376 higher ends (close to 350 °C) of this range, suggesting a gradual transition to the isotropic state  
377 at high temperatures, and a possible glass transition at low temperature. A small percentage of  
378 reflectance reduction is caused by the increase of scattering from distinct polymer networks.  
379 Little change of texture brightness is observed by POM.  
380



381  
 382 **Supplementary Fig. 18 Low-temperature stability of PS-BPLCs at Stage IV during 10 temperature**  
 383 **circles. a<sub>1</sub>-a<sub>4</sub>** Photographs of the Mobius strip-like sample for the first circle: (a<sub>1</sub>) before immersed in, (a<sub>2</sub>)  
 384 being immersed in, (a<sub>3</sub>) just taken out from liquid nitrogen, (a<sub>4</sub>) after recovering to room temperature. **b<sub>1</sub>-b<sub>4</sub>**  
 385 Optic photos of the Mobius strip-like sample for the tenth circle: (b<sub>1</sub>) before immersed in, (b<sub>2</sub>) being  
 386 immersed in, (b<sub>3</sub>) just taken out from liquid nitrogen, (b<sub>4</sub>) after recovering to room temperature.  
 387

388 In order to investigate the low-temperature stability of PS-BPLCs, BPLCs film in Stage  
 389 IV (with the size of 2 mm × 20 mm) is rolled up to form a Mobius strip (a<sub>1</sub>). (a<sub>1</sub>-a<sub>4</sub>) present the  
 390 photographs of the Mobius strip for the test of the first circle. The Mobius strip is put in liquid  
 391 nitrogen for 1 min and then is taken out to recover to room temperature. (b<sub>1</sub>-b<sub>4</sub>) present the  
 392 photos of the Mobius strip after being immersed in liquid nitrogen and taken out for 10 circles,  
 393 the shape and color of the Mobius strip keep unchanged. Especially, iridescent color can be  
 394 seen on the strip (green speckles on the strip) before and after 10 circles of immersing in or  
 395 taking out from liquid nitrogen.

396



397  
 398 **Supplementary Fig. 19 Thermal stability of monodomain polymer-stabilized BPII.** POM images and  
 399 *in situ* reflection spectra are captured at a certain temperature when the cell was cooled from 25 to -190 °C  
 400 and heated up from -190 to 340 °C.  
 401

402 To the best of our knowledge, the broadest temperature window reported by Choi et al.<sup>6</sup>  
 403 based on a polymer-stabilized BPII is 50 °C. Both polymer-stabilized BPIII/BPII/BPI core-shell  
 404 configurations in Stage IV have a temperature window of over -190 to 340 °C (Supplementary

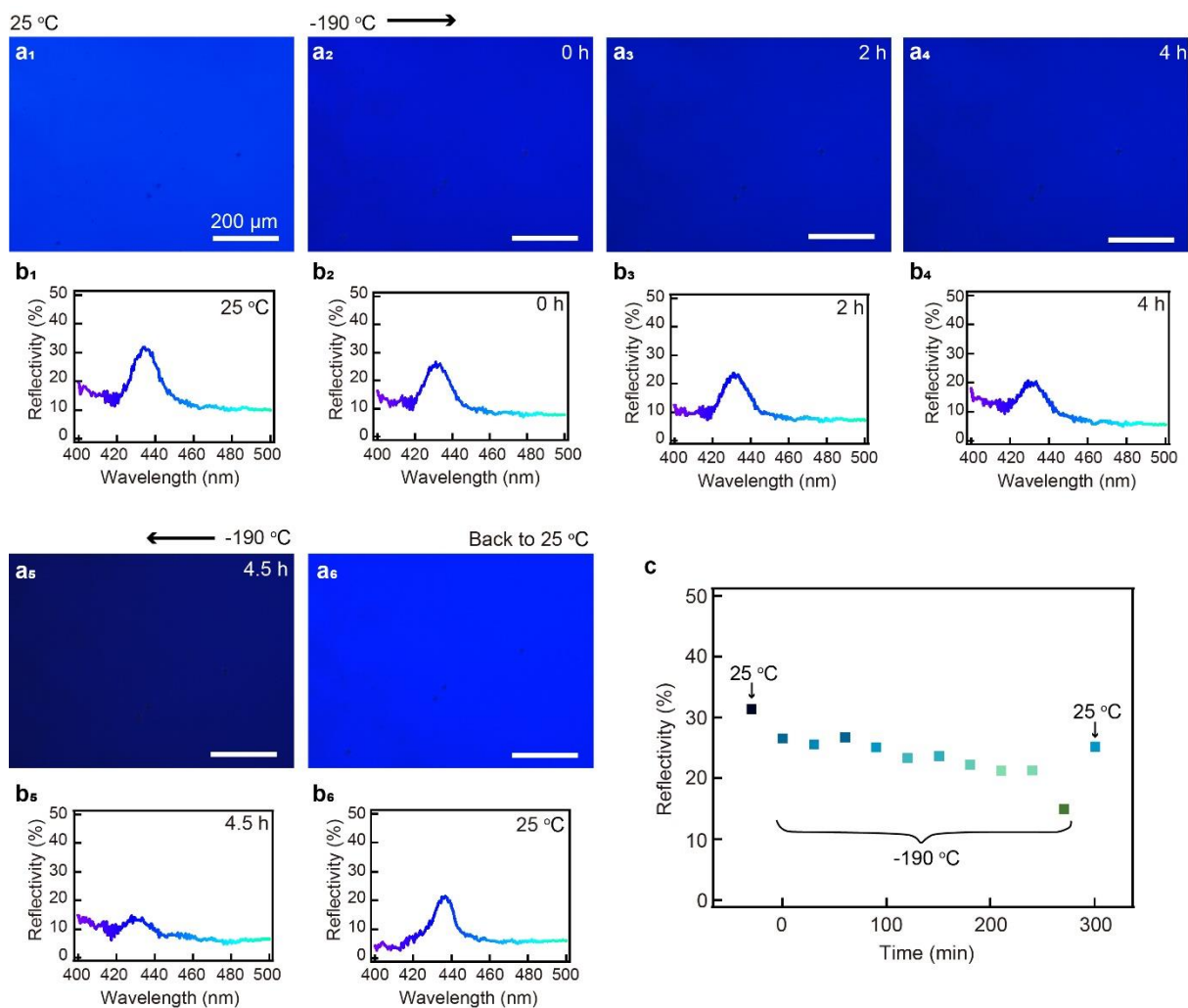
405 Fig. 17). To gain additional insights into the thermal stability of BPII, herein, detailed  
406 information is obtained by focusing on monodomain BPII at the same conditions.

407 The as-prepared monodomain polymer-stabilized BPII<sub>{100}</sub> is cooled at 5 °C/min from 25  
408 to -190 °C and then heated at 5 °C/min from -190 to 340 °C. The corresponding change of  
409 textures and reflection spectra are shown in Supplementary Fig. **19**. During the temperature  
410 reduction process, the maximum reflectivity slightly decreases when the temperature is close  
411 to -190 °C, suggesting a possible glass transition<sup>7</sup>. When BPII is heated from -190 to 0 °C,  
412 maximum reflectivity shows a tendency of decreasing first and increasing afterward. The  
413 maximum reflectivity of BPII gradually decreases when the temperature is further heated to  
414 350 °C.

415

416





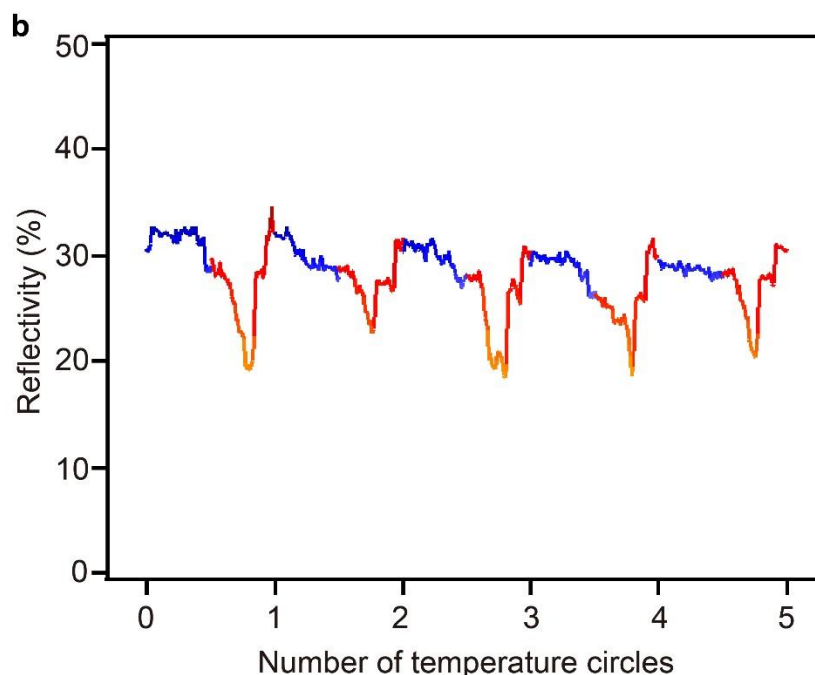
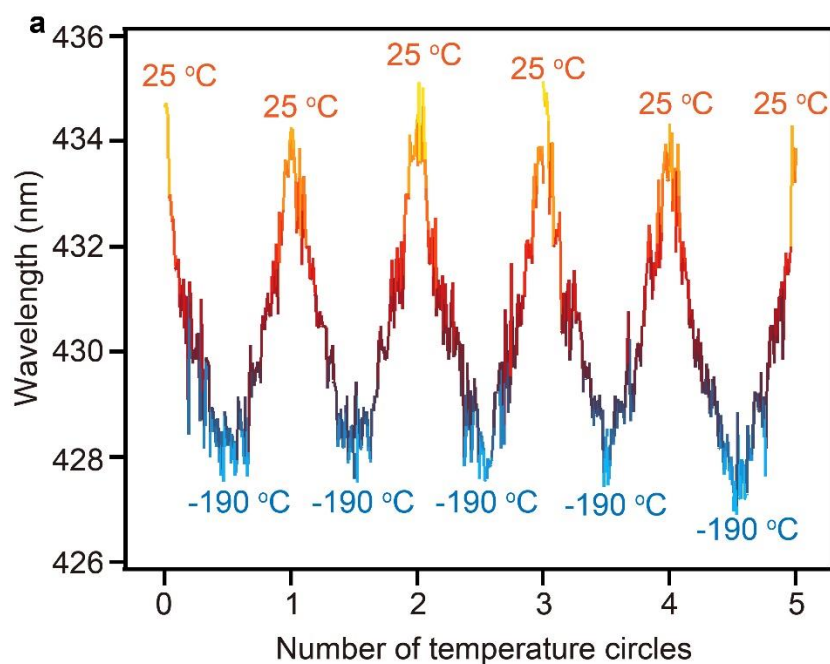
417

418 **Supplementary Fig. 20 Thermal stability of monodomain polymer-stabilized BPII kept at -190 °C as**  
 419 **a function of time. a<sub>1</sub>, b<sub>1</sub>** POM image (a<sub>1</sub>) and the corresponding reflection spectrum (b<sub>1</sub>) of the sample at  
 420 25 °C. **a<sub>2</sub>-a<sub>5</sub>** POM images of samples kept at -190 °C for 0-4.5 h. **b<sub>2</sub>-b<sub>5</sub>** Corresponding reflection spectra of  
 421 (a<sub>2</sub>-a<sub>5</sub>). **a<sub>6</sub>, b<sub>6</sub>** POM image (a<sub>6</sub>) and corresponding reflection spectrum (b<sub>6</sub>) of the sample when temperature  
 422 recovers to 25 °C. **c** Variation in reflectivity of the sample with a function of time.

423

424

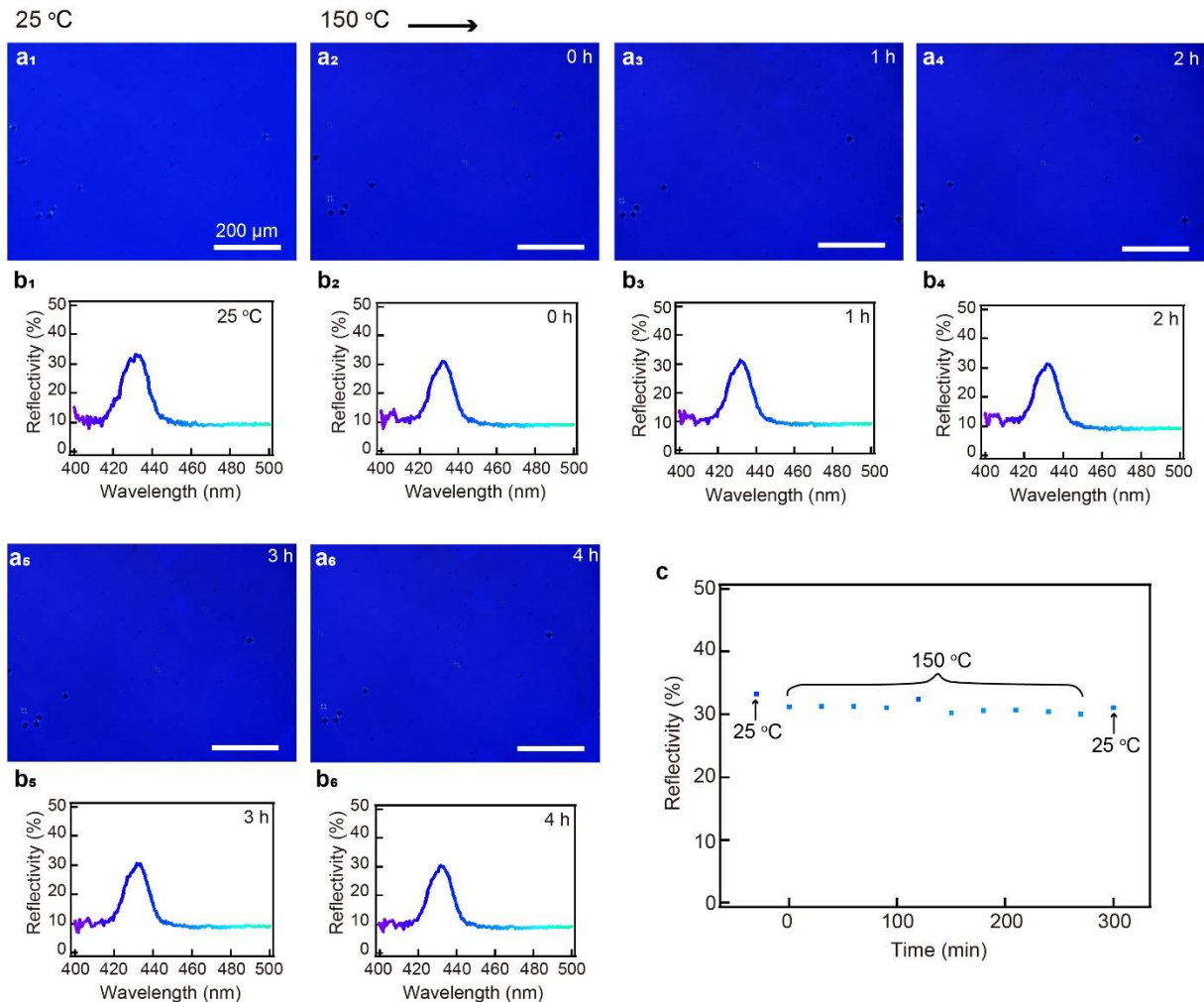
425 The low-temperature stabilities of polymer-stabilized BPII are investigated. Monodomain  
 426 BPII is firstly cooled from 25 to -190 °C at 5 °C/min and then is kept at -190 °C with a function  
 427 of time. The textures and reflectivity of BPII can be well maintained within 4 h with only a  
 428 slight decrease of reflectivity. After 4 h, the reflectivity falls to 14.644%, supposing to be a  
 429 possible glass transition at such low temperatures. Then, optical properties are recovered after  
 430 the sample is heated to 25 °C at 10 °C/min (c), except for a bit reduction of reflectively  
 431 compared with the original sample (a<sub>1</sub>).



432  
 433 **Supplementary Fig. 21 Optical stability of polymer-stabilized BPII during five temperature change**  
 434 **circles from 25 to -190 °C and then recovers to 25 °C. a** Blue and red-shift of the center of reflection  
 435 **peak. b** Reflectance changes of reflection peak.

436  
 437 The thermal stability of polymer-stabilized BPII in low temperatures is investigated. The  
 438 optical properties of monodomain BPII<sub>{100}</sub> are investigated during 5 cycles within 25 to -190 °C.  
 439 With decreasing of temperature, the center of the stopband ( $\lambda_c$ ) blue-shift from 435 to 427 nm.  
 440 Then, the  $\lambda_c$  gradually red-shift to 435 nm with the rise of temperature. The reflectivity of  
 441 polymer-stabilized BPII<sub>{100}</sub> is slightly reduced from approx. 33% to approx. 20% when the

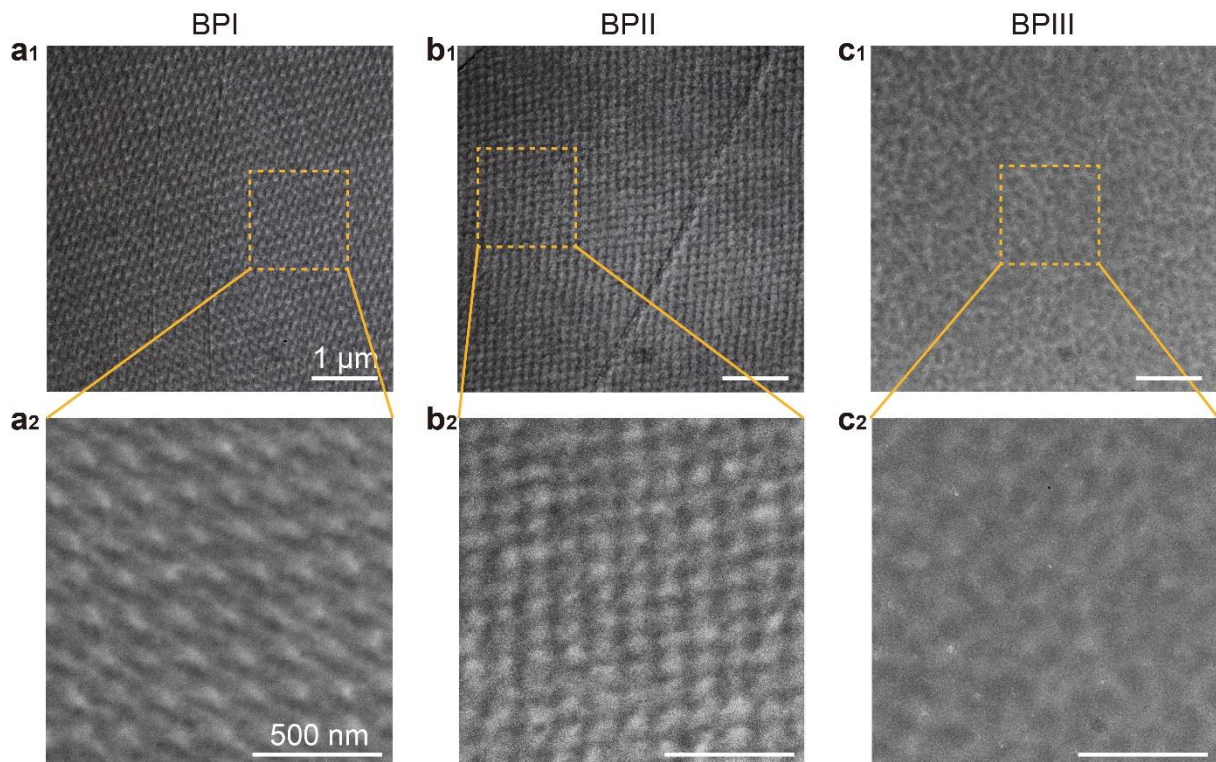
442 temperature is lowered to -190 °C. Then, BPII<sub>{100}</sub> is heated from -190 to 25 °C and the  
 443 maximum reflectivity shows a tendency of reducing first and increasing afterward. The  
 444 maximum reflectivity recovers to the original state after the temperature recovers to 25 °C.  
 445



446 **Supplementary Fig. 22 High-temperature stability of monodomain polymer-stabilized BPII kept at**  
 447 **150 °C as a function of time. a<sub>1</sub>, b<sub>1</sub>** POM image (a<sub>1</sub>) and the corresponding reflection spectrum (b<sub>1</sub>) of  
 448 original monodomain polymer-stabilized BPII<sub>{100}</sub> captured at 25 °C. **a<sub>2</sub>-a<sub>6</sub>, b<sub>2</sub>-b<sub>6</sub>** POM images (a<sub>2</sub>-a<sub>6</sub>) and  
 449 the corresponding reflection spectra (b<sub>2</sub>-b<sub>6</sub>) of samples kept at 150 °C for 0-4.5 h. (c) Variation in  
 450 reflectivity of the sample with a function of time.  
 451

452  
 453 The high-temperature stability of polymer-stabilized BPII is investigated. Monodomain  
 454 BPII<sub>{100}</sub> is firstly cooled from 25 to -190 °C at 5 °C/min and then is heated to 150 °C. The  
 455 temperature is kept at 150 °C with a function of time. There is no obvious degradation of texture  
 456 and reflectivity. After 4.5 h, the sample is cooled to 25 °C at 5 °C/min.

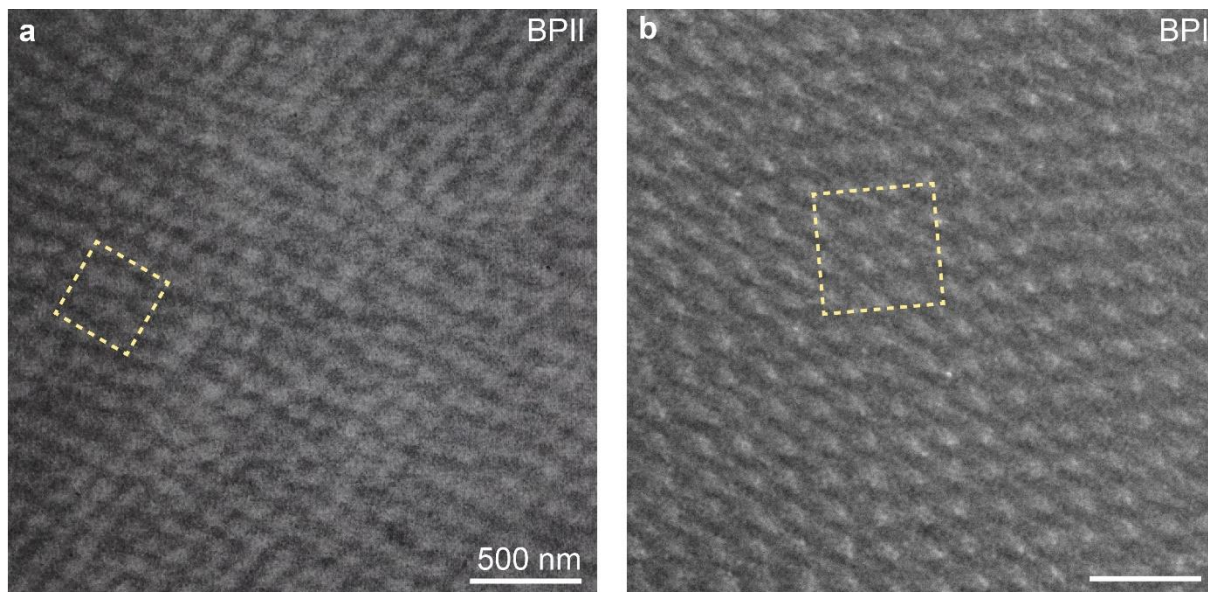
457 **Supplementary Note 4 Real-space TEM observation and crystal analysis of PS-BPLCs**



458 **Supplementary Fig. 23** TEM images of (a<sub>1</sub>, a<sub>2</sub>) BPI<sub>{100}</sub>, (b<sub>1</sub>, b<sub>2</sub>) BPII<sub>{100}</sub> and (c<sub>1</sub>, c<sub>2</sub>) BPIII. (a<sub>2</sub>-c<sub>2</sub>)  
459 Magnified TEM images of the squares highlighted in (a<sub>1</sub>-c<sub>1</sub>).  
460  
461

462 TEM observations are performed on ultrathin sections of PS-BPLCs with a thickness of 50  
463 nm. The cuts are made parallel to {110}<sub>BPI</sub> and {100}<sub>BPII</sub> crystal plane of BPII. The arrangement  
464 of DTCs is observed in (a<sub>1</sub>, a<sub>2</sub>) BPI<sub>{100}</sub>, (b<sub>1</sub>, b<sub>2</sub>) BPII<sub>{100}</sub> and (c<sub>1</sub>, c<sub>2</sub>) BPIII. Both BPI<sub>{100}</sub> and  
465 BPII<sub>{100}</sub> are highly ordered while BPIII has a random structure for its amorphous structures.  
466

467



468

469

470

471

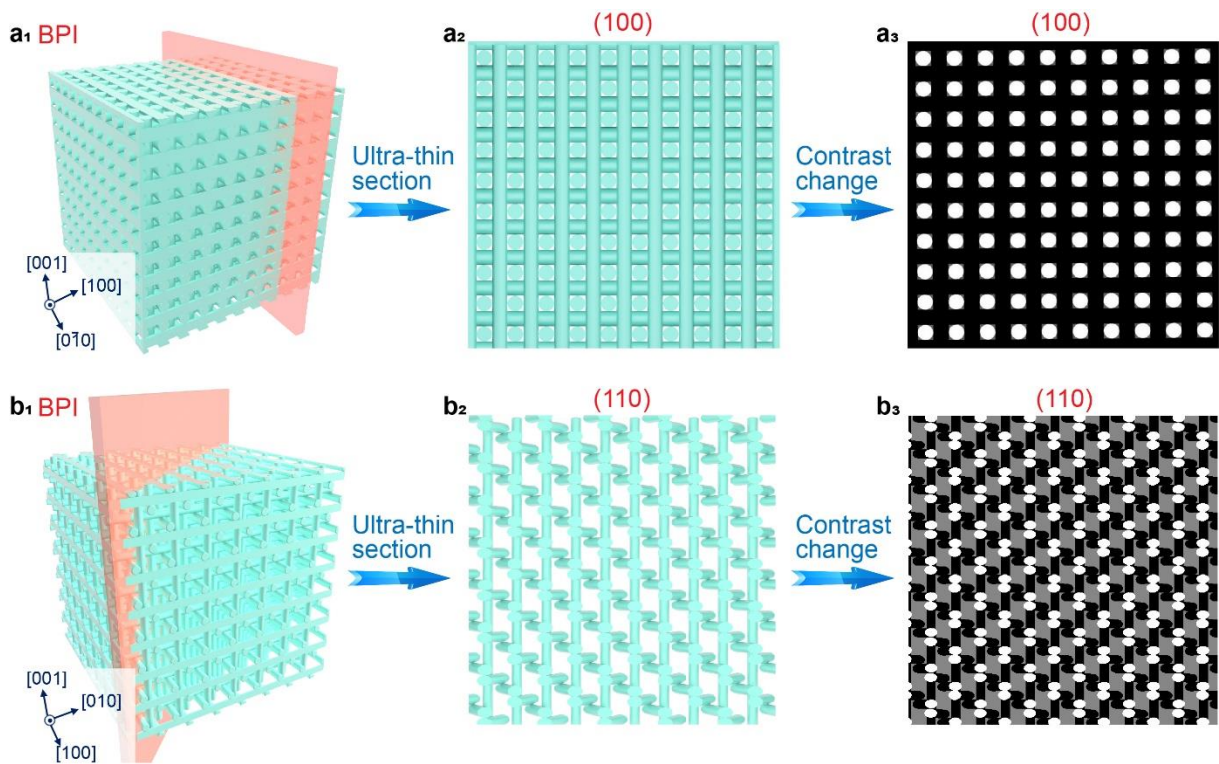
472

473

474

**Supplementary Fig. 24** TEM images of  $\text{BPII}_{\{100\}}$  (a) and  $\text{BPI}_{\{100\}}$  (b). The yellow squares highlight the area with  $3 \times 3$  unit cells of  $\text{BPII}_{\{100\}}$  and  $\text{BPI}_{\{100\}}$ .

A closer inspection of  $\text{BPII}_{\{100\}}$  (a) and  $\text{BPI}_{\{100\}}$  (b) structures revealing that the lattice constant of BPI is larger than BPII.



477 **Supplementary Fig. 25 Theoretically predicted cross-sectional structure of (a) BPII or (b) BPI for**  
 478 **BPLCs.  $a_1, b_1$**  Theoretically predicted arrangement of the DTCs in the 3D model.  $a_2, b_2$  Ultra-thin section  
 479 of the sample with a thickness of 50 nm corresponding to the region shaded in red ( $a_1, b_1$ ), viewed along  
 480 the [100] ([110]) direction for BPII (BPI).  $a_3, b_3$  Contrast changed the image of ( $a_2, b_2$ ) depending on the  
 481 orientation of DTCs.

482

483

484

485

486

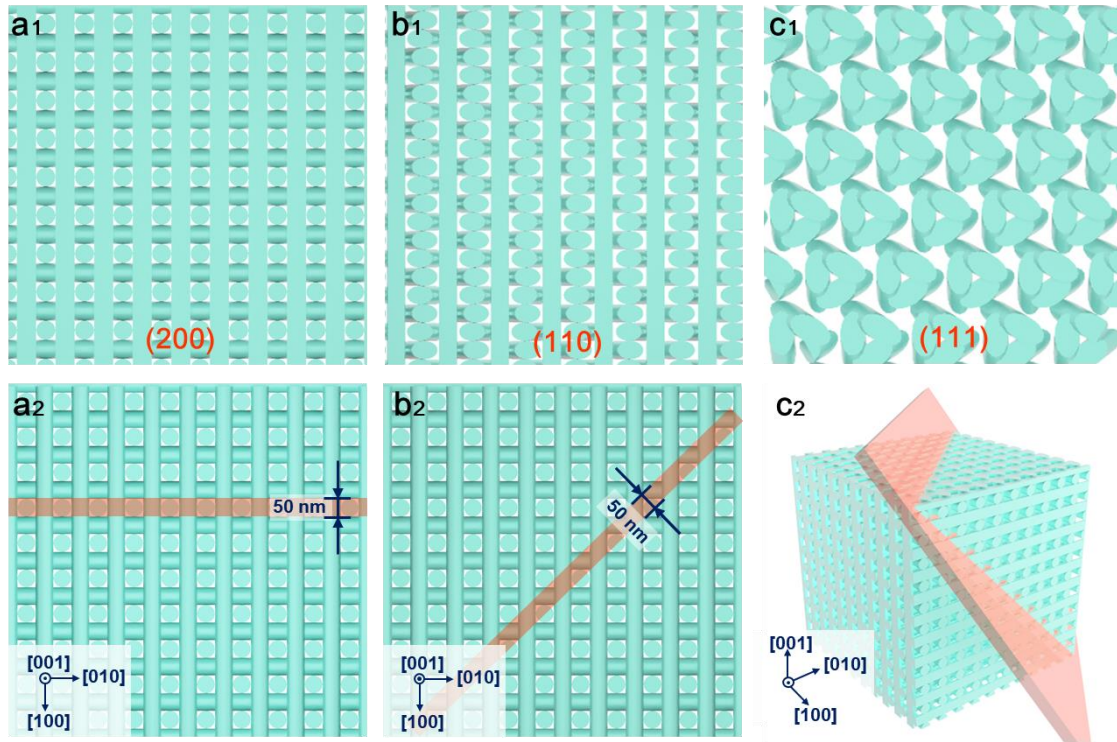
487

488

489

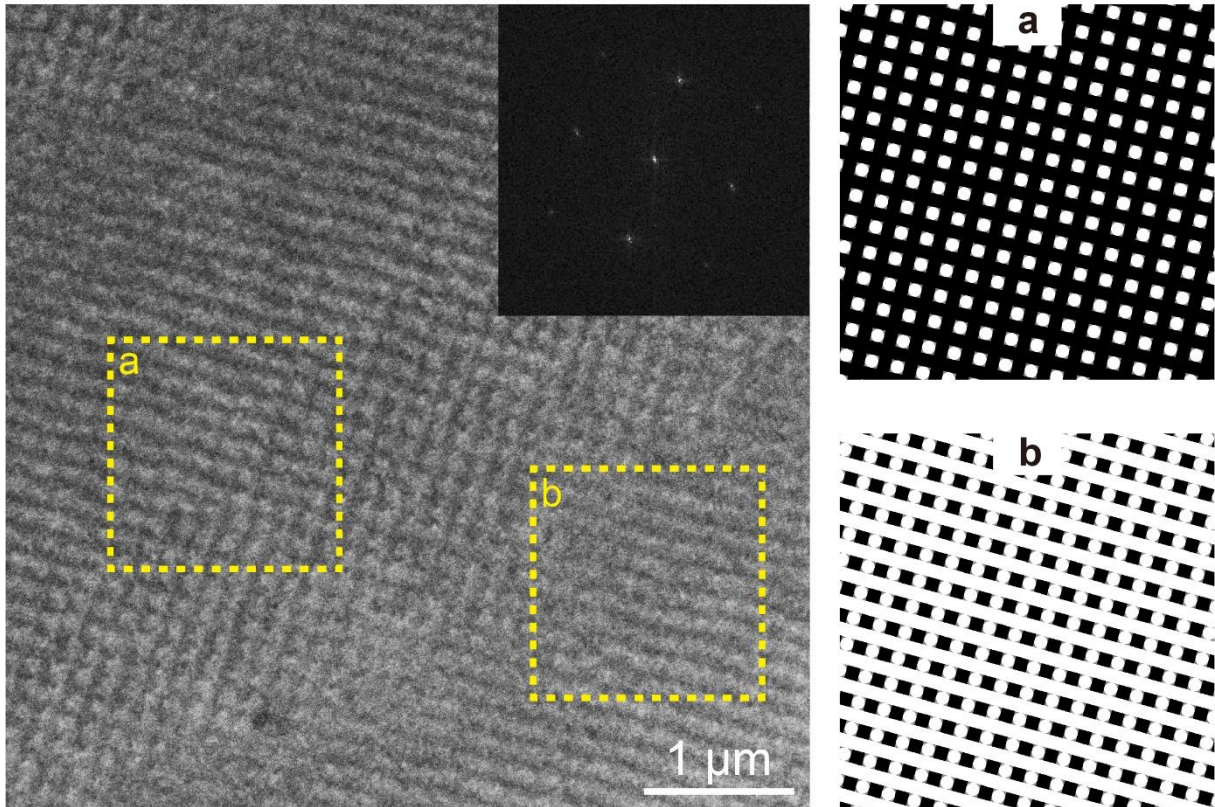
490

The predicted patterns with contrast change ( $a_3, b_3$ ) are obtained from the top view of the slice ( $a_2, b_2$ ) cut from the red slice in the 3D BPII or BPI model ( $a_1, b_1$ ). Considering that the LC director is oriented parallel to the cylinder axis within a DTC. DTCs should appear alternated bright or dark at the sites where they are vertical or parallel to the slice plane. The contrast change of the intermediate brightness is used in the region without DTCs<sup>8</sup>. Theoretically predicted TEM slices ( $a_3, b_3$ ) are used as representations of the DTCs arrangement of experiment results.



491  
492  
493  
494  
495

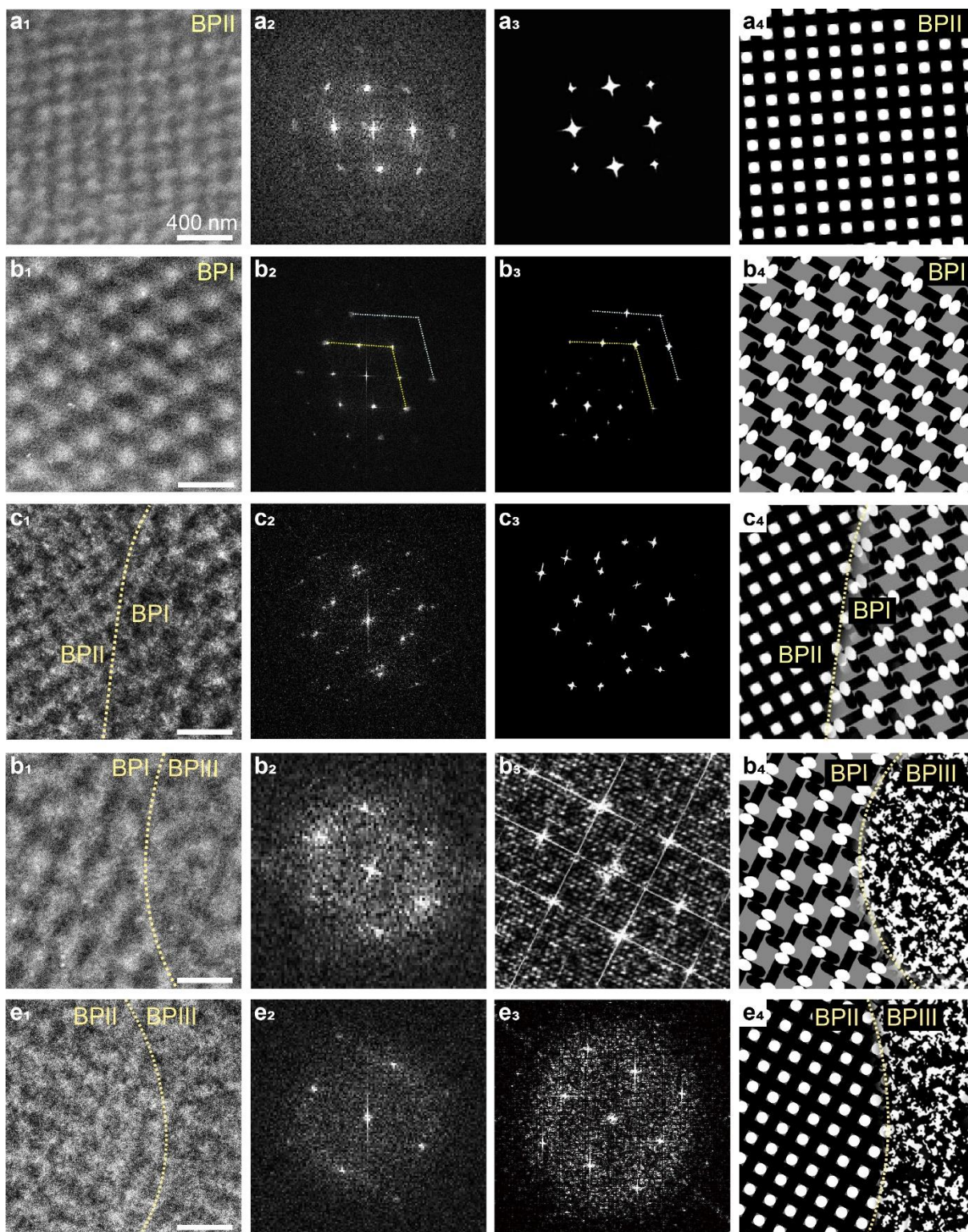
**Supplementary Fig. 26 Schematic representation of the DTCs arrangement of BPII with distinct orientation.** **a<sub>1</sub>-c<sub>1</sub>** Ultra-thin section models are relative to those shaded in red of (**a<sub>2</sub>-c<sub>2</sub>**). **a<sub>2</sub>-c<sub>2</sub>** Models of DTCs arrangement of BPII with distinct crystal orientations.



497  
 498 **Supplementary Fig. 27 Two types of structures observed in a TEM image corresponding to  $BPII_{\{100\}}$**   
 499 **after polymer-stabilization.** The inserted image is an FFT pattern transferred from the TEM image. **a** The  
 500 structure obtained when the upper part of the unit cell is cut and **(b)** is obtained when the bottom part of the  
 501 unit cell is cut.  
 502

503 The lattice constant of BPII of 171.82 nm is measured from the FFT pattern in the inserted  
 504 image. Two types of TEM structures belonging to  $BPII_{\{100\}}$  can be observed both in  
 505 experimental and predicted results. Owing to the thickness of slices (approx. 50  $\mu\text{m}$ ) obtained  
 506 from the ultra-thin section process are much smaller than the lattice constant of BPII, the  
 507 structures shown in (a) are observed when the upper part of the unit cell is cut during the ultra-  
 508 thin section process. And the structures shown in (b) are observed once the bottom part of the  
 509 unit cell is cut.  
 510  
 511





512  
 513 **Supplementary Fig. 28** TEM images (**a<sub>1</sub>-e<sub>1</sub>**), corresponding fast Fourier transform (FFT) patterns (**a<sub>2</sub>-e<sub>2</sub>**),  
 514 theoretically predicted FFT patterns (**a<sub>3</sub>-e<sub>3</sub>**) of BPLCs, and theoretical models for the arrangement of DTCs  
 515 (**a<sub>4</sub>-e<sub>4</sub>**). **(a)** BPII<sub>{100}</sub>, **(b)** BPI<sub>{110}</sub>, **(c)** interface between BPII<sub>{100}</sub> and BPI<sub>{110}</sub>, **(d)** interface between  
 516 BPI<sub>{110}</sub> and BPIII, and **(e)** interface between BPII<sub>{100}</sub> and BPIII. The dotted yellow lines highlight the  
 517 interfaces between BPI, BPII, and BPIII.  
 518

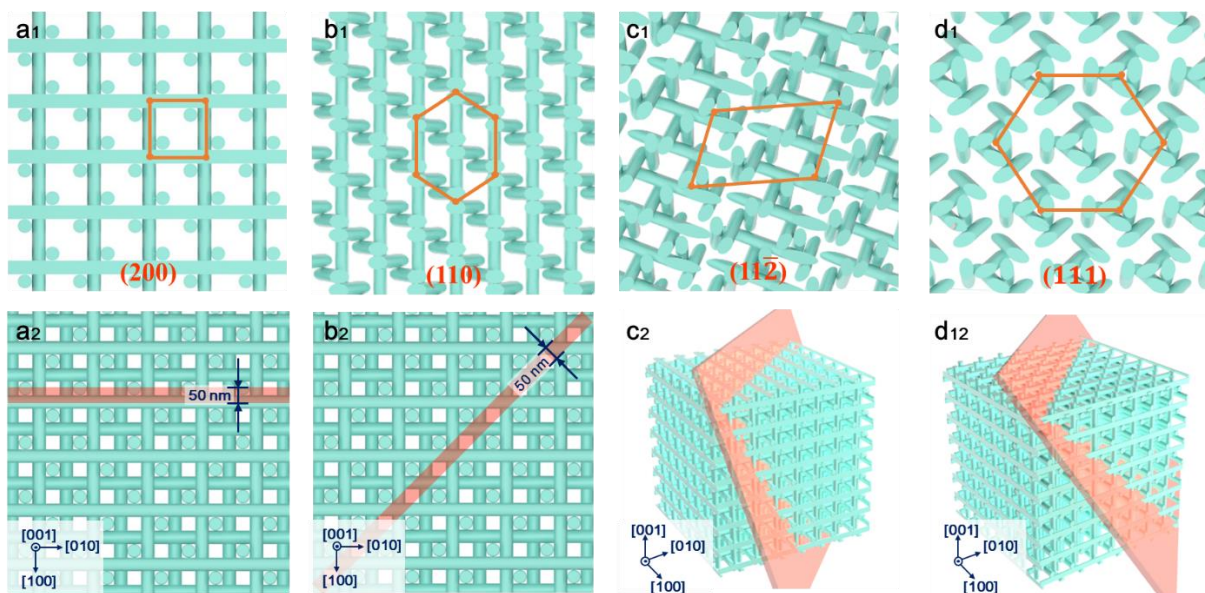
519 Detailed TEM images and corresponding theoretically predicted DTCs arrangement of  
 520 phase interfaces are presented here. (**a<sub>1</sub>-a<sub>4</sub>**) are monophasic BPII<sub>{100}</sub>. A highly ordered

521 microscopic periodic structure with a lattice constant of 171.82 nm in TEM image is observed  
522 (a<sub>1</sub>) which clearly indicates a four-fold symmetry in the observed contrasts, which agrees with  
523 the theoretically predicted symmetry along [100] direction (a<sub>4</sub>). (a<sub>4</sub>) is theoretically predicted  
524 arrangement of DTCs and the structures are obtained by cutting from the 3D model and change  
525 the contrast based on the method shown in (Supplementary Fig. 27). (a<sub>3</sub>) is the FFT pattern  
526 transferred from (a<sub>4</sub>), in which the speckles have the same position as (a<sub>2</sub>), indicating the real-  
527 space structures of (a<sub>1</sub>) and (a<sub>4</sub>) have the same arrangement of DTCs and size. Thus, the  
528 predicted DTCs arrangement in (a<sub>4</sub>) can represent the structures in (a<sub>1</sub>). Similarly, (b<sub>1</sub>-b<sub>4</sub>) are  
529 monophasic BPI. In the BPI lattice, the lattice constant  $a$  is measured as 252.57 nm. FFT  
530 analysis (b<sub>2</sub>) shows a sharp diffraction pattern of periodic BPI<sub>{110}</sub> which is similar to the  
531 theoretically predicted result (b<sub>3</sub>), indicating predicted DTCs arrangement (b<sub>4</sub>) can represent  
532 the results in TEM images (b<sub>1</sub>). (c<sub>1</sub>-c<sub>4</sub>) show the interface between BPII<sub>{100}</sub> and BPI<sub>{110}</sub>. A  
533 clear interface can be observed from the TEM image (c<sub>1</sub>). Both the FFT pattern (c<sub>2</sub>) transferred  
534 from the TEM image and the similar theoretically predicted result (c<sub>3</sub>) yield a combined sharp  
535 diffraction speckles of BPI<sub>{110}</sub> and four-fold symmetry of BPII<sub>{100}</sub>. All speckles of BPI<sub>{110}</sub>  
536 and BPII<sub>{100}</sub> indicate the highly ordered structures near the interface and phase transition  
537 occurs in submicron scales without transitional region. (d<sub>1</sub>-d<sub>4</sub>) depict the sample with the  
538 interface between BPIII and BPI<sub>{110}</sub> at Stage III. TEM image of a clear interface between BPIII  
539 and BPI<sub>{110}</sub> (d<sub>1</sub>) is observed. FFT analysis (d<sub>2</sub>) shows combined diffraction of BPI<sub>{110}</sub> and  
540 BPIII: the diffraction pattern from the periodic BPI<sub>{110}</sub> and a scattering background from the  
541 amorphous structure of BPIII. TEM slice derived from the theoretical model is obtained in (d<sub>4</sub>).  
542 FFT pattern in (d<sub>3</sub>) is transferred from a theoretically predicted arrangement of DTCs near the  
543 boundary region (d<sub>4</sub>). Comparing the FFT pattern transferred from the experimental and  
544 predicted result, the diffraction patterns are the same. Therefore, the DTCs arrangement in TEM  
545 result (d<sub>1</sub>) can be represented by predicted results (d<sub>4</sub>), indicating BPIII-to-BPI transformation  
546 is diffusionless without a transitional region near the interface. (e<sub>1</sub>-e<sub>4</sub>) demonstrate the interface

547 between BPIII and BPII<sub>{100}</sub>. A clear interface can be observed from the TEM image (e<sub>1</sub>). FFT  
548 pattern (e<sub>2</sub>) shows the combination of the periodic diffraction pattern of BPII<sub>{100}</sub> and the  
549 adjacent amorphous structure of BPIII. Theoretically predicted FFT pattern (e<sub>3</sub>) is similar to  
550 that obtained from experimental results, indicating the arrangement of DTCs in TEM (e<sub>1</sub>) is the  
551 same as a predicted result (e<sub>4</sub>).

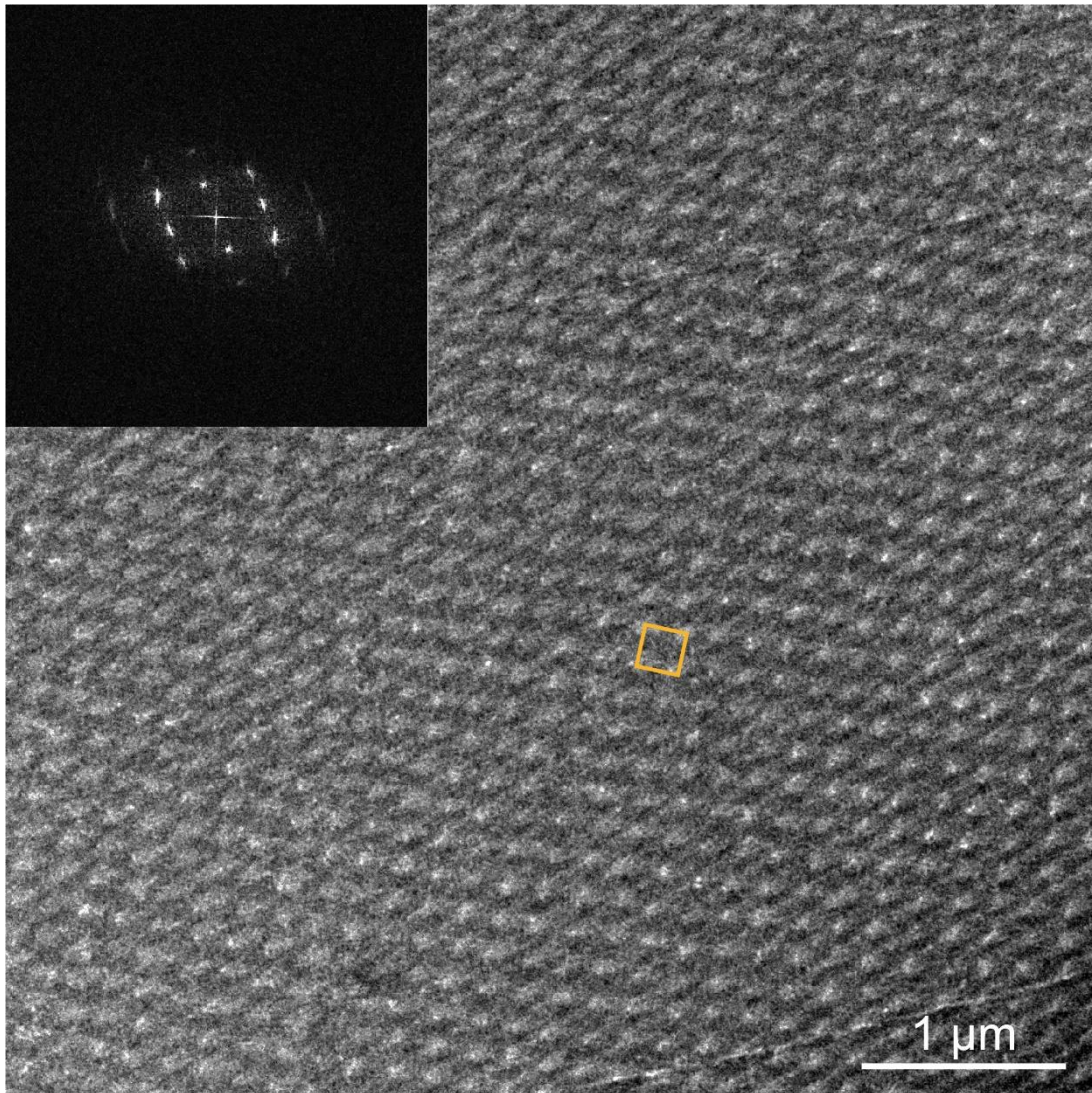
552

553



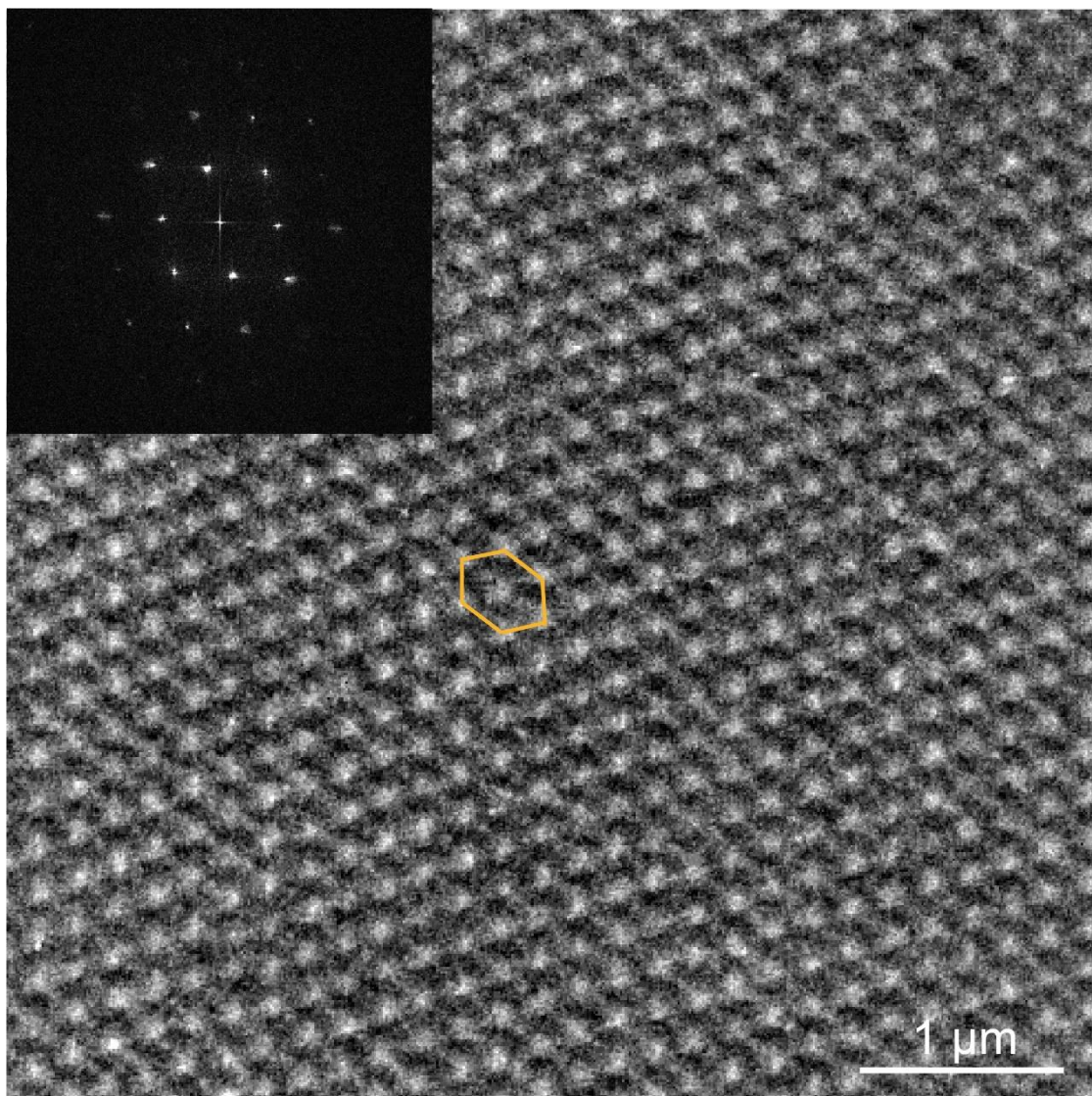
554  
 555 **Supplementary Fig. 29 Schematic representation of DTCs arrangement of BPI with distinct**  
 556 **orientation. a<sub>1</sub>-d<sub>1</sub>** Section models correspond to those shaded in red (a<sub>2</sub>-d<sub>2</sub>). The geometric figures in  
 557 orange represent the typical arrangement that may be observed in the TEM images. a<sub>1</sub>-d<sub>1</sub> DTCs distributed  
 558 within a thin section of BPI with distinct crystal orientation.  
 559

560  
 561  
 562  
 563



564  
565  
566  
567  
568  
569  
570

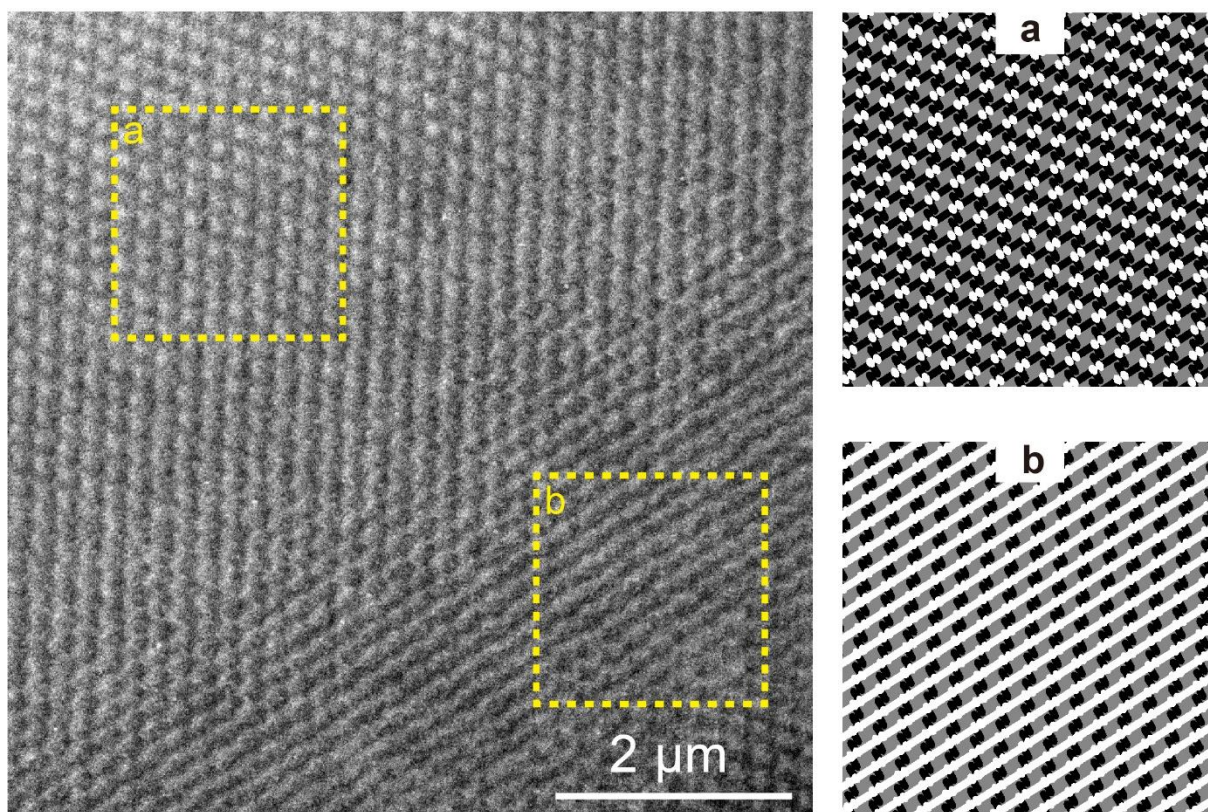
**Supplementary Fig. 30 TEM image of BPI<sub>(100)</sub> after polymer-stabilization.** The inserted image is an FFT pattern transferred from the TEM image. A rectangle highlights a unit cell of BPI which in accordance with the predicted arrangement of DTCs in Supplementary Fig. 29a<sub>1</sub>



571  
572 **Supplementary Fig. 31 TEM image of BPI<sub>(110)</sub> after polymer-stabilization.** The inserted image is an  
573 FFT pattern transferred from the TEM image.

574  
575 The lattice constant of BPI (252.57 nm) is measured from the FFT pattern in the inserted  
576 image. The flat hexagons can be found in a periodic structure which is in accordance with the  
577 predicted arrangement of DTCs in Supplementary Fig. 29b<sub>1</sub>

578

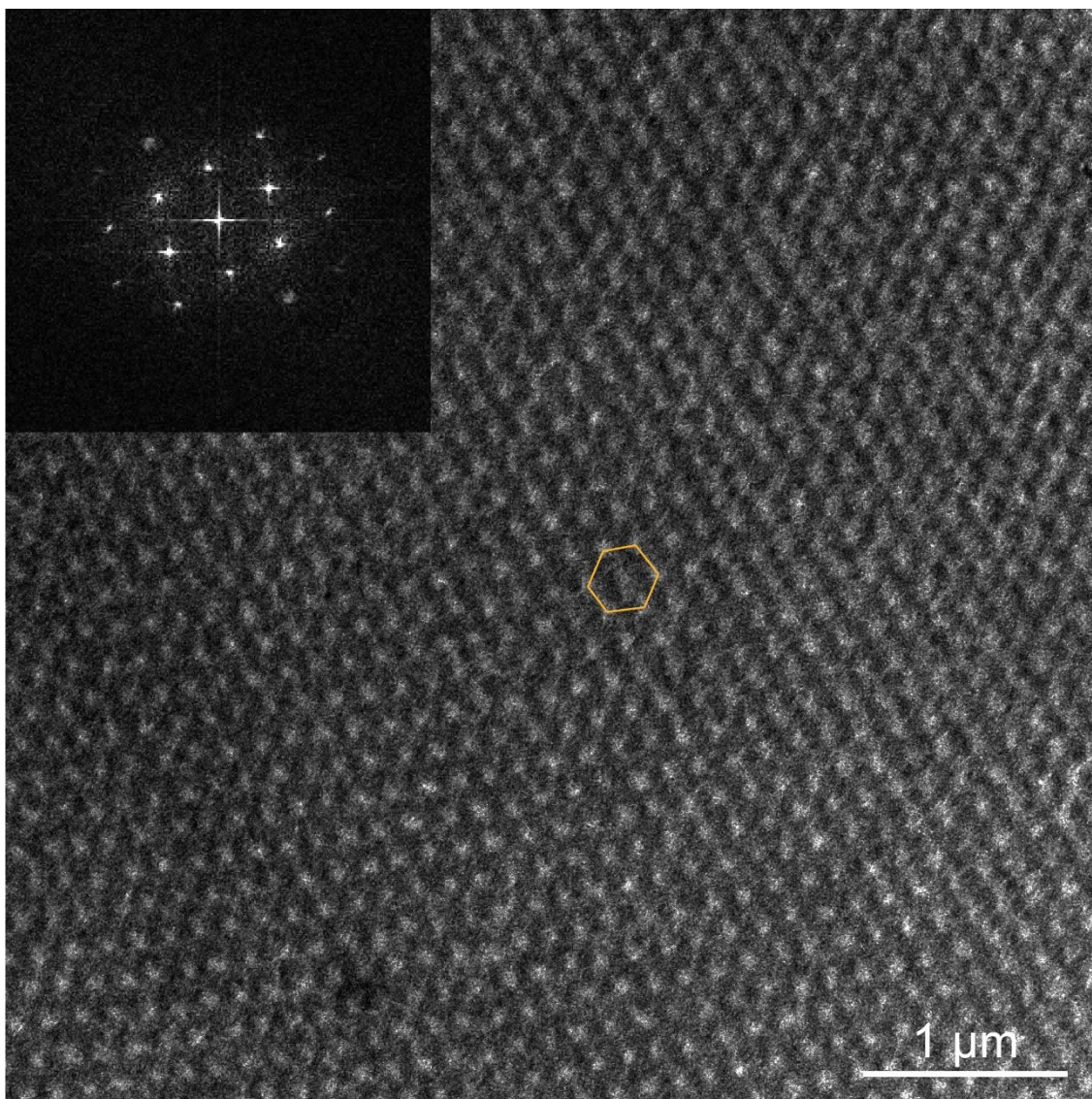


579  
 580 **Supplementary Fig. 32 Two types TEM images of BPI<sub>{110}</sub> after polymer-stabilization. a**  
 581 The structure obtained when the upper part of the unit cell is cut and (b) the bottom part of the  
 582 unit cell is cut.

583  
 584 Two types of TEM structures of BPI<sub>{110}</sub> are observed both in experimental results and  
 585 predicted results. Owing to the thickness of slices (approx. 50 μm) obtained from the ultra-thin  
 586 section process is much smaller than the lattice constant (252.57 nm). The structures shown in  
 587 (a) are observed when the upper part of the unit cell is cut. And the structures shown in (b) are  
 588 observed once the bottom part of the unit cell is cut.

589

590

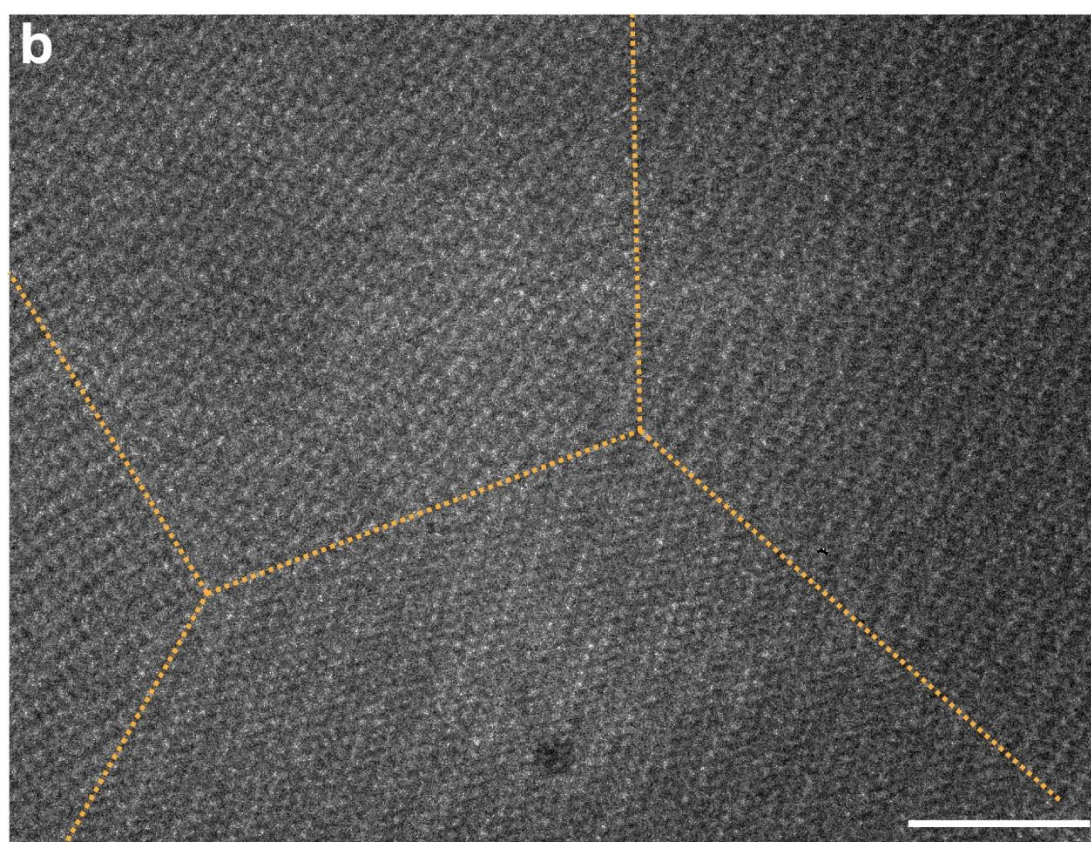
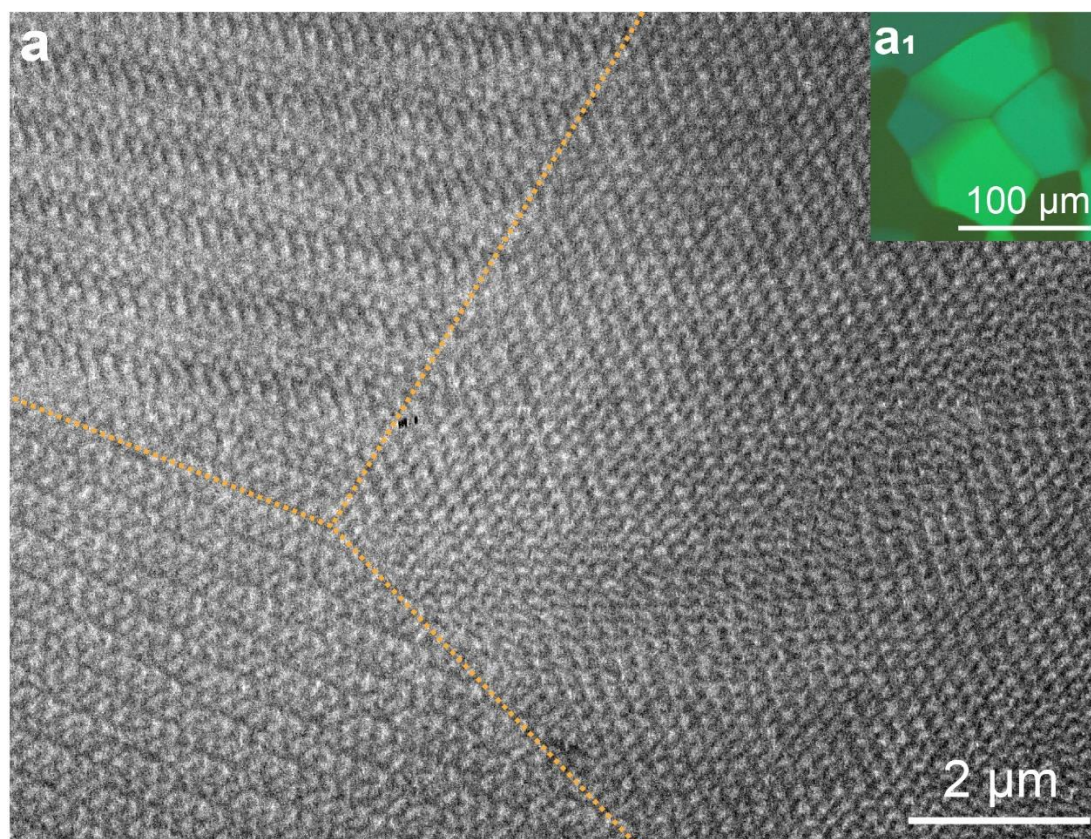


591 **Supplementary Fig. 33 TEM image of BPI<sub>(111)</sub> after polymer-stabilization.** The inserted image is an  
592 FFT pattern transferred from the TEM image.  
593

594 The regular hexagons can be found in a periodic structure which is in accordance with the  
595  
596 predicted arrangement of DTCs in Supplementary Fig. 29d<sub>1</sub>

597



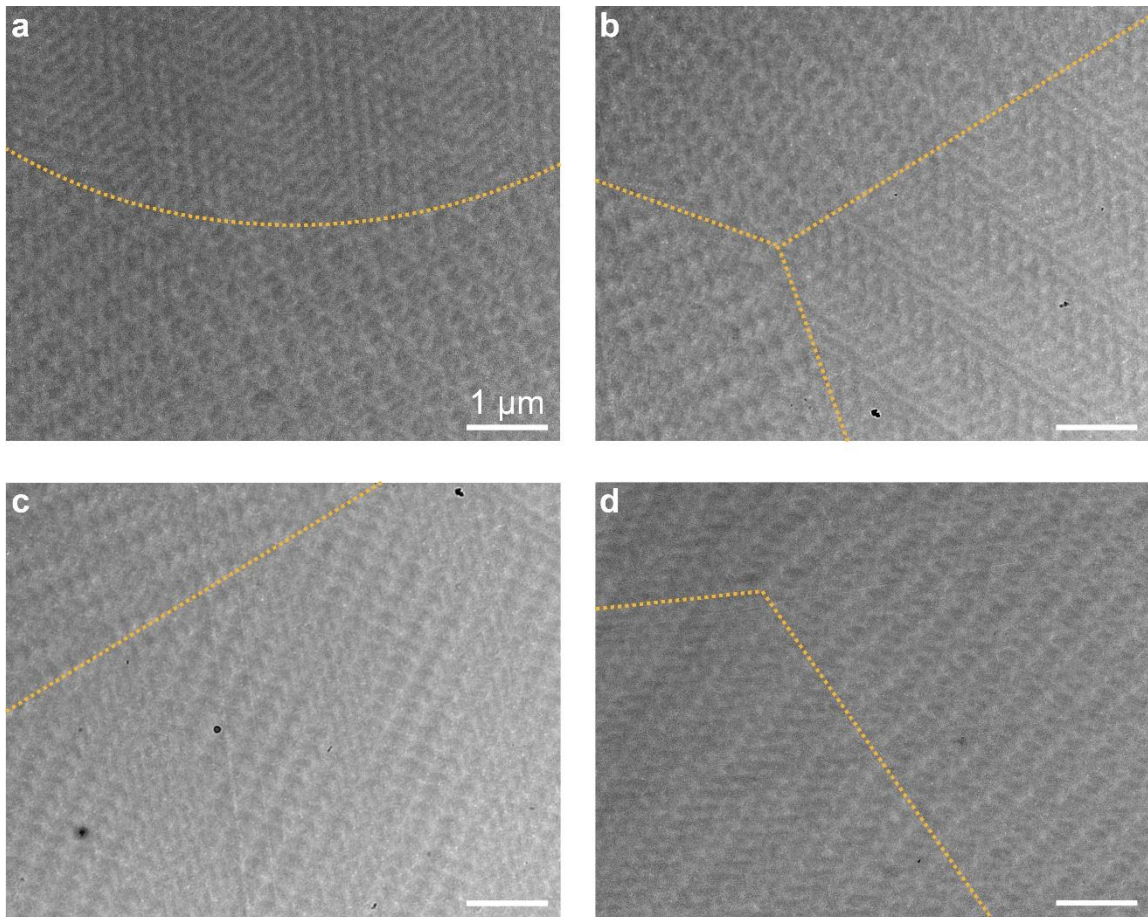


599  
600  
601  
602  
603

**Supplementary Fig. 34** TEM images of the interfaces among domains with distinct orientations of polydomain BPI. **a** Interfaces among three domains in polydomain BPI. **b** Interfaces among four domains in polydomain BPI.

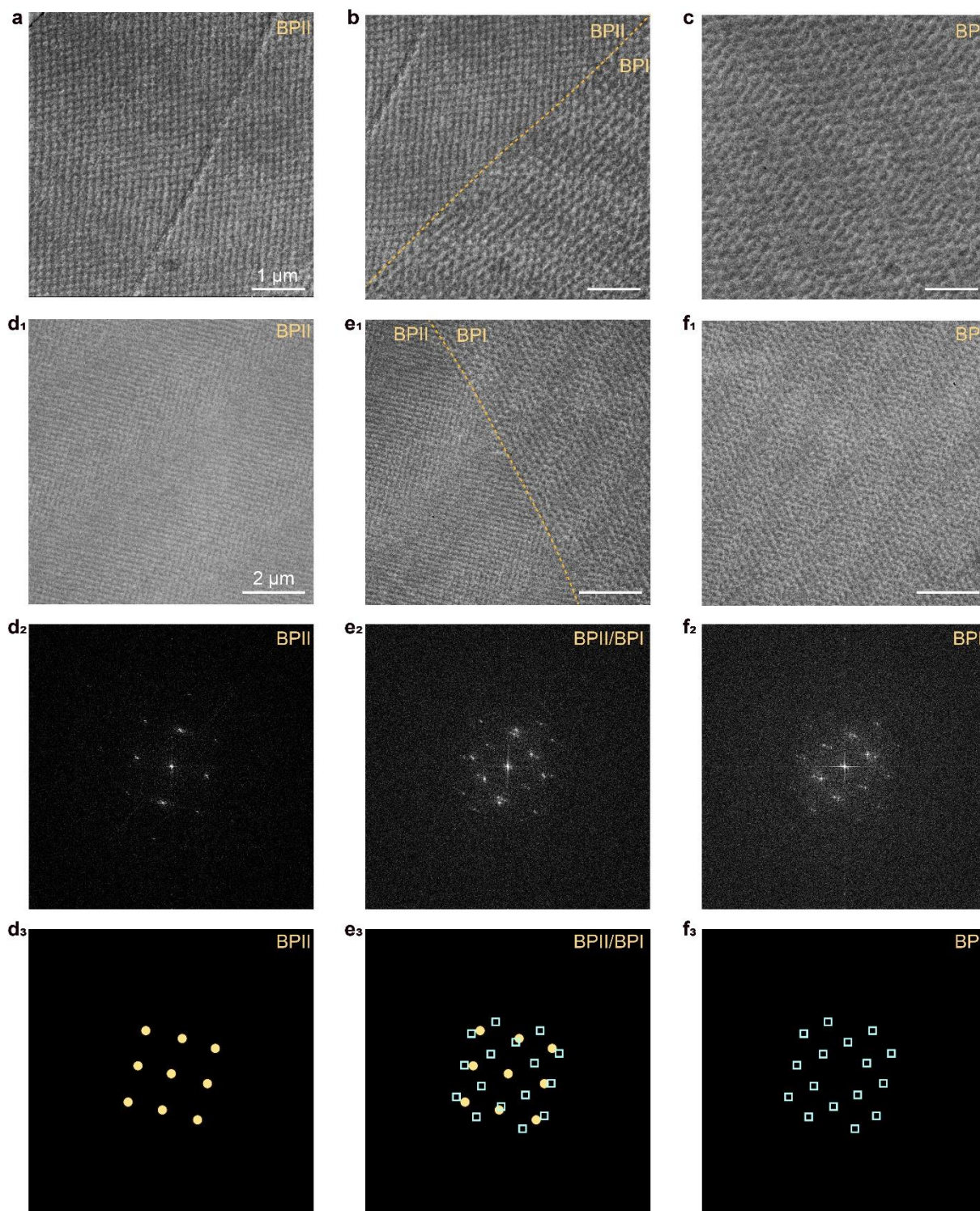
604 Excepting for the interface among BPI, BPII, and BPIII, TEM images of the interfaces  
605 corresponding to three and four domains of polydomain BPI are shown. The inserted image of  
606 (a<sub>1</sub>) shows the POM images of grains of polydomain BPI.

607  
608  
609  
610  
611



612 **Supplementary Fig. 35 a-d** Amplified TEM images of the interfaces among domains with distinct  
613 orientations of polydomain BPI. The orange dotted line highlights the interfaces.  
614  
615

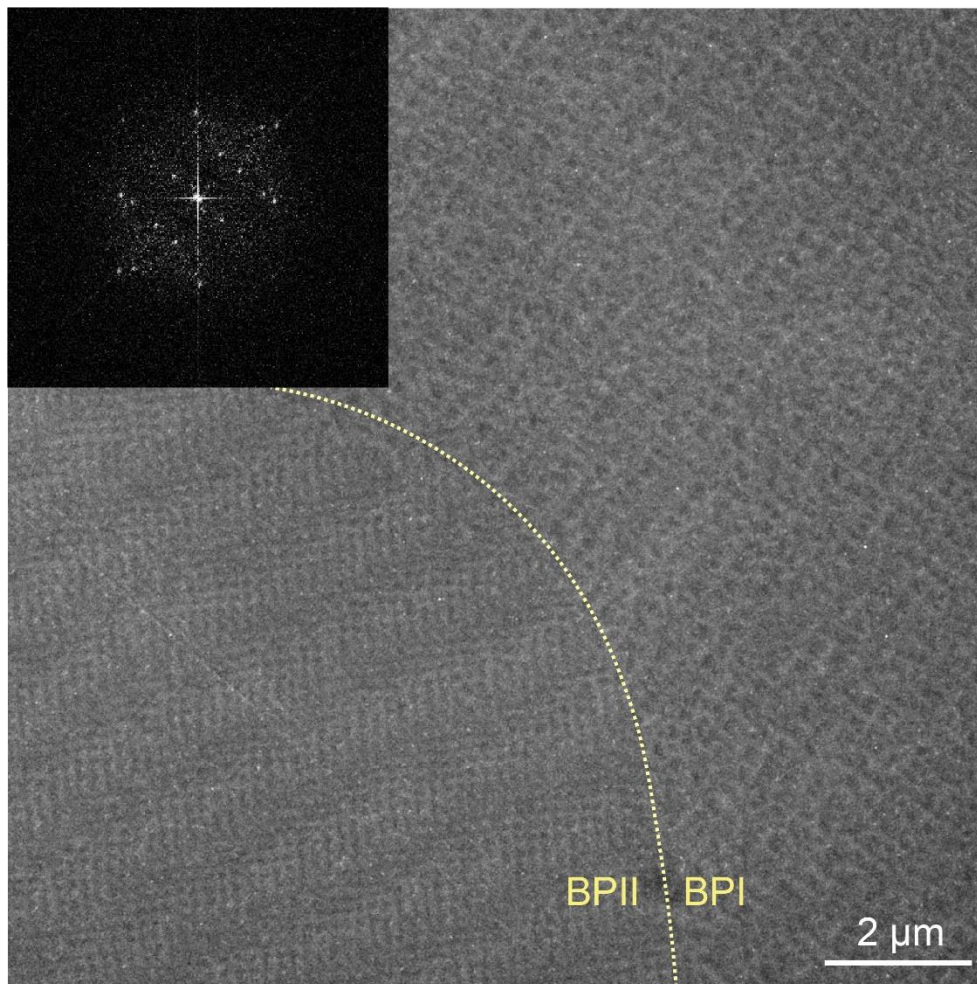
616  
617



618  
 619 **Supplementary Fig. 36 TEM images and the corresponding FFT patterns of the interface between**  
 620 **BPII<sub>{100}</sub> and BPI<sub>{110}</sub>.** (a, d<sub>1</sub>, d<sub>2</sub>, d<sub>3</sub>) BPII<sub>{100}</sub>, (b, e<sub>1</sub>, e<sub>2</sub>, e<sub>3</sub>) the interface of BPI<sub>{110}</sub>/BPII<sub>{100}</sub>, and (c, f<sub>1</sub>, f<sub>2</sub>,  
 621 f<sub>3</sub>) BPI<sub>{110}</sub>. d<sub>2</sub>, e<sub>2</sub>, f<sub>2</sub> FFT patterns were transferred from the areas in (d<sub>1</sub>, e<sub>1</sub>, f<sub>1</sub>), respectively. (d<sub>3</sub>, e<sub>3</sub>, f<sub>3</sub>)  
 622 Schematic diffraction patterns highlight the same position of the speckles of experiment results in (d<sub>2</sub>, e<sub>2</sub>, f<sub>2</sub>).  
 623 d<sub>3</sub> Diffraction speckles of BPII<sub>{100}</sub> labeled by yellow solid circles; e<sub>3</sub> simple addition of schematic diffraction  
 624 patterns of monophasic BPII<sub>{100}</sub> from (d<sub>3</sub>) and BPI<sub>{110}</sub> from (f<sub>3</sub>). where the yellow solid circles represent  
 625 diffraction speckles of BPII<sub>{100}</sub> and blue hollow squares represent diffraction speckles of BPI<sub>{110}</sub>; f<sub>3</sub>  
 626 diffraction speckles of BPI<sub>{110}</sub> labeled by blue hollow squares;  
 627

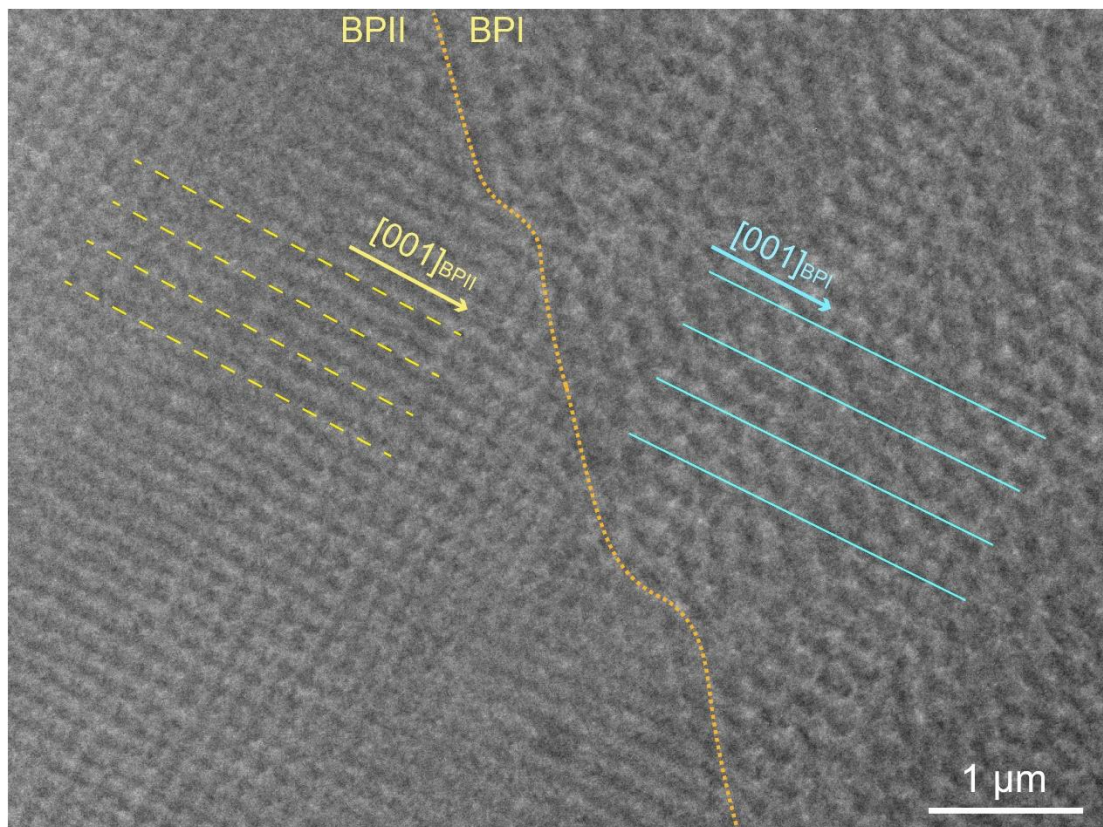
628 Especially, FFT patterns of the interface between  $BPI_{\{110\}}$  and  $BPII_{\{100\}}$  ( $e_2, e_3$ ) possess two  
629 sets of sharp diffraction speckles, which can be regarded as a simple addition of diffraction  
630 patterns of monophasic  $BPII_{\{100\}}$  ( $d_2, d_3$ ) and  $BPI_{\{110\}}$  ( $f_2, f_3$ ). It is confirmed by FFT analysis  
631 that the size and position of diffraction spots near the interface ( $e_2, e_3$ ) are the same as those in  
632 the bulk for  $BPII_{\{100\}}$  ( $d_2$ ) highlighted by yellow solid circles ( $d_3$ ) and  $BPI_{\{110\}}$  ( $e_2$ ) highlighted  
633 by blue hollow squares ( $e_3$ ), proving there is just a diffusionless reconfiguration of DTCs  
634 (equally to no transitional region near the interface).

635



636 **Supplementary Fig. 37 TEM image of the interface between BPII and BPI in real-space.** The inserted  
637 image is the FFT pattern transferred from the TEM image. The interface is highlighted by a yellow dotted  
638 line.  
639  
640

641 Herein, the BPII has the  $[100]$  orientation out-of-plane while the BPI has the orientation  
642 other than  $[110]$  direction out-of-plane.



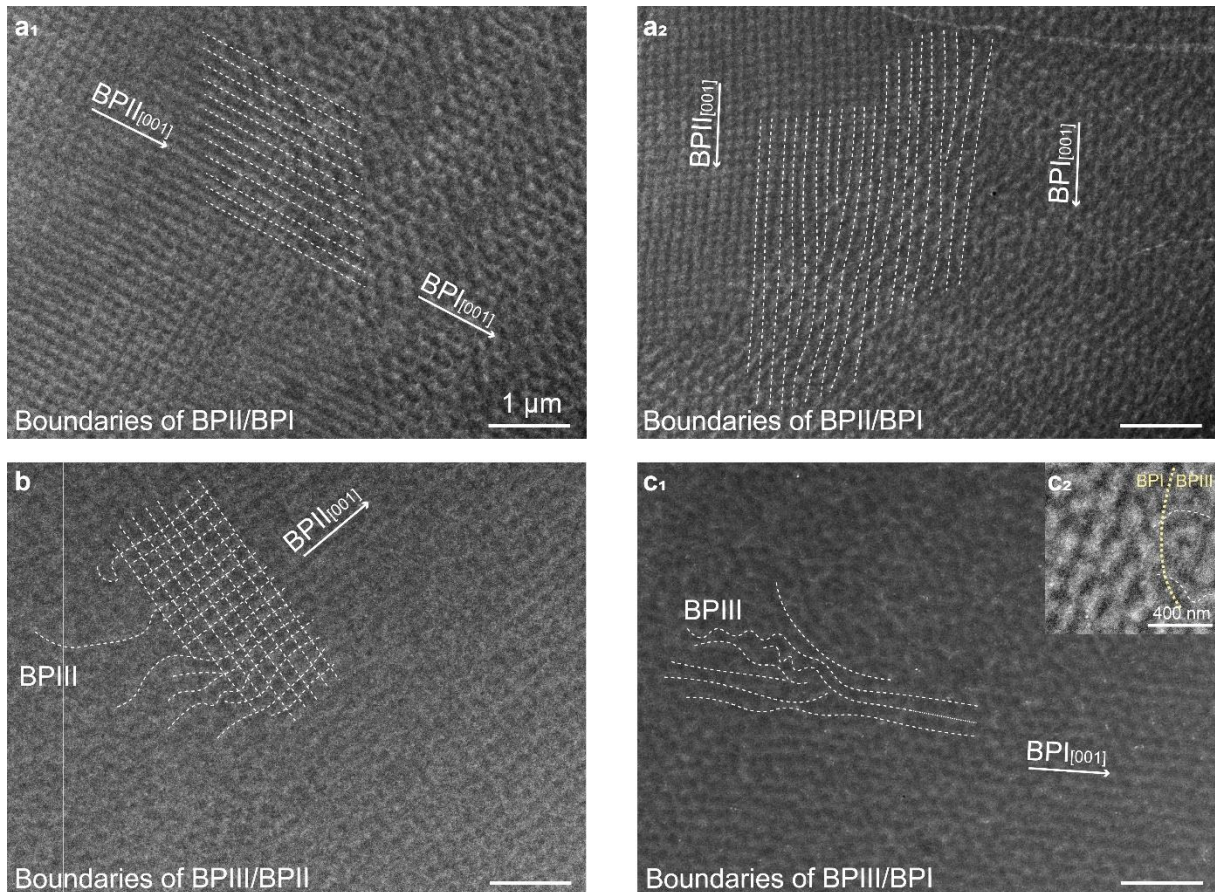
643  
 644 **Supplementary Fig. 38 TEM image of the interface between  $BPII_{\{100\}}$  and  $BPI_{\{110\}}$ .** The orange dotted  
 645 line represents the interface. The yellow dash line parallel to the  $[001]$  orientation of  $BPII_{\{100\}}$  and blue  
 646 solid lines represent the  $[001]$  orientation of  $BPI_{\{110\}}$ .

647  
 648 More specifically, the orientation of BPI is influenced by BPII and the crystal lattice of BPI

649 and BPII is coherent on the interface.

650

651



652  
 653 **Supplementary Fig. 39 TEM observation of the interfaces among BP III, BP II, and BPI.** a<sub>1</sub>-a<sub>2</sub>  
 654 Coherent crystal lattices between the interfaces of BP II<sub>{100}</sub>/BPI<sub>{110}</sub>. DTCs arrangement of the well-  
 655 matched parts is highlighted by dotted white lines. **b** The interface between BP III and BP II<sub>{100}</sub>, in which a  
 656 DTC can simultaneously belongs to crystal lattices of BP III and BP II<sub>{100}</sub>. **c**<sub>1</sub> The interface between BP III  
 657 and BP II<sub>{100}</sub>, where curved lines highlight the DTCs that coexist in both BP II<sub>{100}</sub> and BP III unit cells. **c**<sub>2</sub>  
 658 Magnified TEM image of the interface of BPI<sub>{110}</sub>/BP III, where the dotted lines highlight the DTCs  
 659 observed across the interface between BP III and BPI<sub>{110}</sub>.  
 660

661 The position of DTCs and the coherent crystal lattices are investigated by TEM at the  
 662 interfaces of BP II/BPI, BP III/BP II, and BP III/BPI. As for phase transformation between BPI  
 663 and BP II, the interfaces are coherent (a<sub>1</sub>, a<sub>2</sub>), in which a DTC simultaneously belongs to BP II  
 664 unit cells and BPI unit cells. These coherent lattices provide evidence for the thermoelastic  
 665 martensitic transformation between BP II and BPI.

666 Thanks to the clear interfaces observed by TEM between BP III and BP II<sub>{100}</sub> (b), the  
 667 speckles with four-fold symmetric highlighted by the dotted grid belong to BP II<sub>{100}</sub> while the  
 668 curved lines besides the grid highlight the DTCs simultaneously exist in both BP II<sub>{100}</sub> and  
 669 BP III, confirming no transitional area between BP II<sub>{100}</sub> and BP III. Thus, during the phase

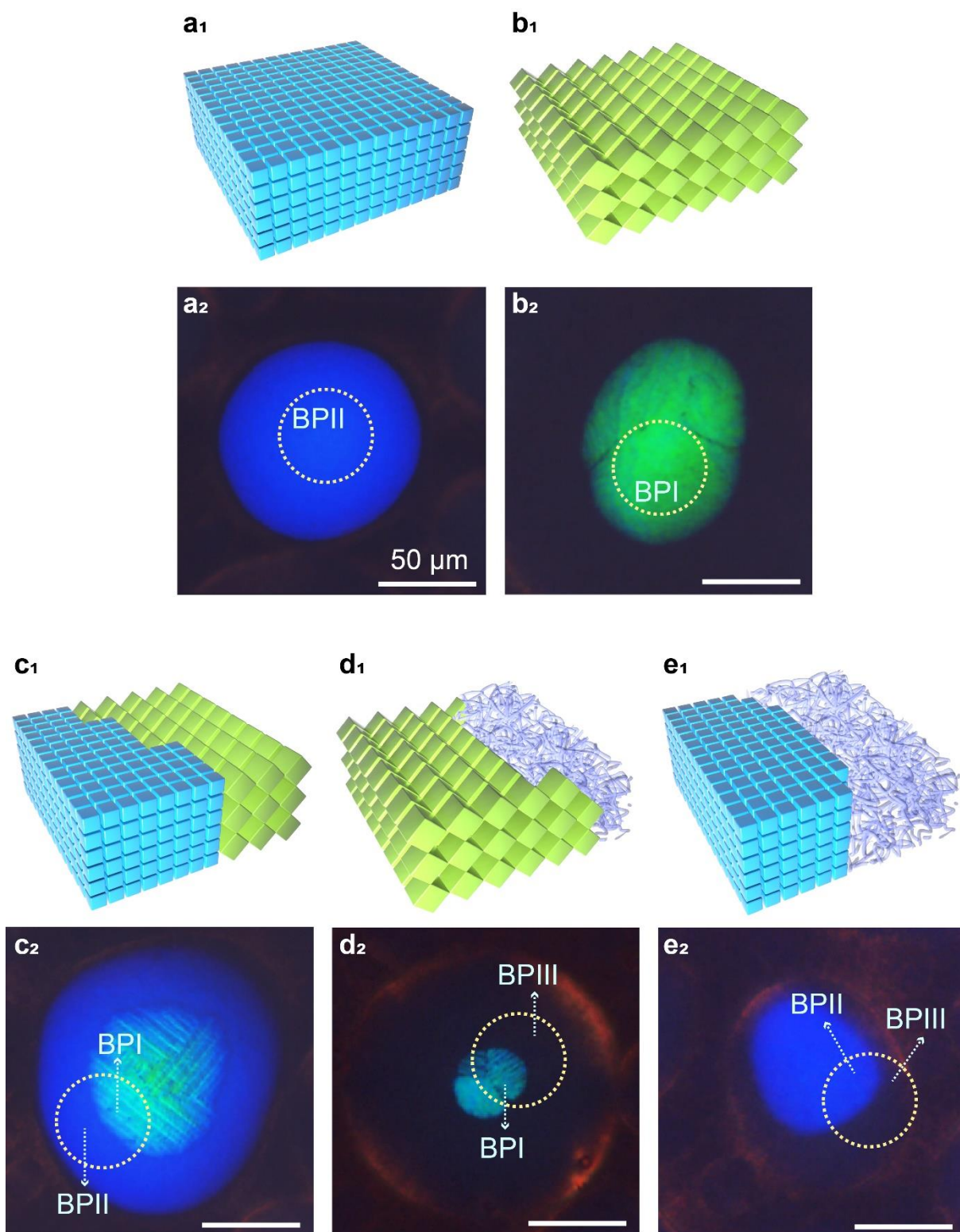
670 transformation between BPIII and BPII, the DTCs reconfiguration will directly form BPIII  
671 phase rather than a process of diffusion first and then reorganize.

672 In terms of the phase transformation between BPIII and BPI (c), a phenomenon was  
673 observed similarly to that of BPII and BPIII. Therefore, the phase transformation between BPIII  
674 and BPI is diffusionless.

675 In a word, by direct observation of the arrangement of DTCs by TEM, several pieces of  
676 evidence were obtained for the confirmation of the DLPT among BPIII, BPII, and BPI.

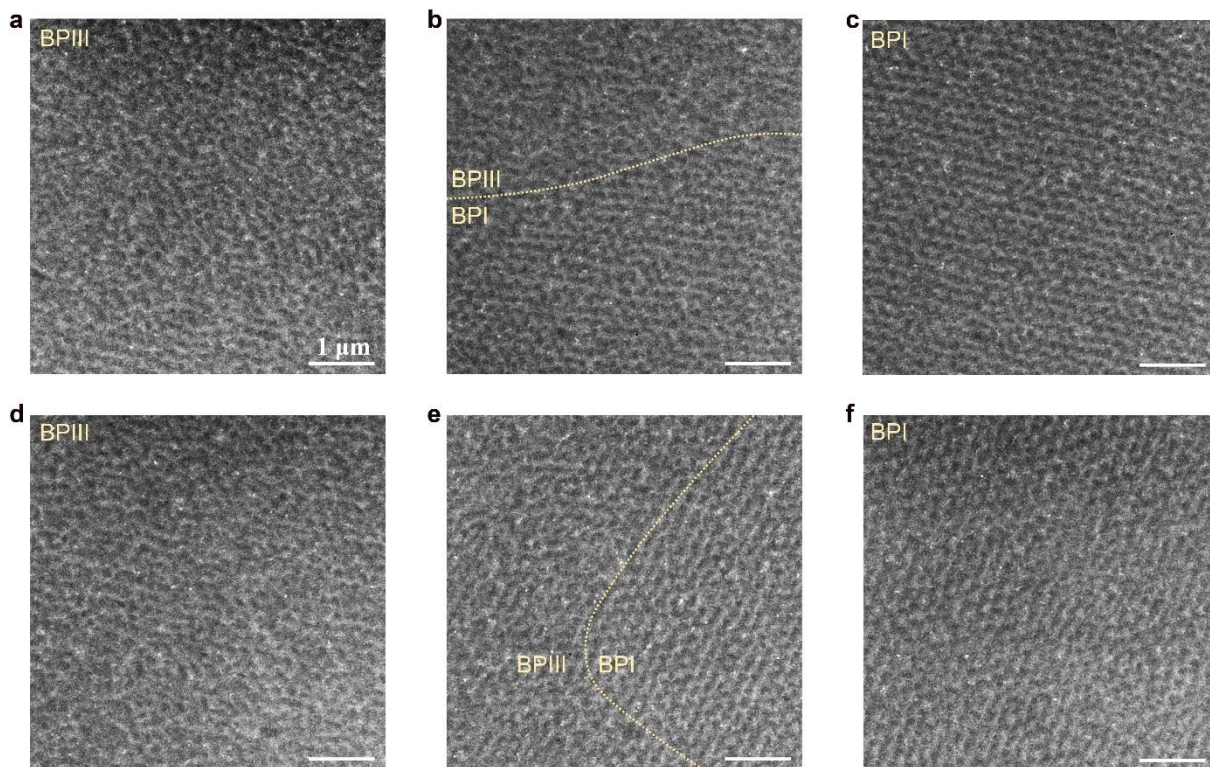
677

678



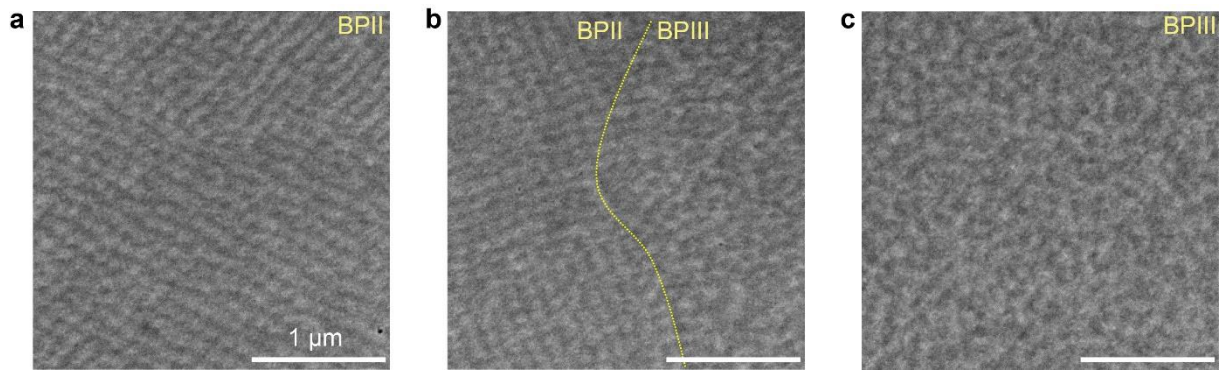
679  
 680 **Supplementary Fig. 40 Interfaces of core-shell configuration at Stage III.** a<sub>1</sub>-e<sub>1</sub> Schematic illustration  
 681 of the arrangement of unit cells in the monophasic BP II and BP I or the interfaces between BP III, BP II, and  
 682 BP I. a<sub>2</sub>-e<sub>2</sub> The textures taken on a crossed POM under reflection mode. The yellow dotted circle highlights  
 683 the interface or monophasic at Stage III. a<sub>2</sub> The polymer-stabilized monophasic BP II<sub>{100}</sub>. b<sub>2</sub> The polymer-  
 684 stabilized monophasic BP I<sub>{110}</sub>. c<sub>2</sub> The polymer-stabilized interface between BP II<sub>{100}</sub> and BP I<sub>{110}</sub>. d<sub>2</sub> The  
 685 polymer-stabilized interface between BP I<sub>{110}</sub> and BP III. e<sub>2</sub> The polymer-stabilized interface between  
 686 BP II<sub>{100}</sub> and BP III.





687  
688  
689  
690  
691

**Supplementary Fig. 41** TEM images of the interfaces between BPI<sub>{110}</sub> and BPIII were observed in real-space. **a, d** BPIII. **b, e** the interface of BPIII and BPI<sub>{100}</sub> (yellow line highlights the interface). **c, f** BPI<sub>{110}</sub>.



692  
693  
694  
695

**Supplementary Fig. 42 TEM images of the interface between BPII and BPIII in real-space. a**  
**BPII<sub>{100}</sub>. b** The interface between BPII<sub>{100}</sub> and BPIII (yellow line highlights the interface). **c** BPIII.

696

The structures of BPII<sub>{100}</sub> either near the interface or in the bulk are highly ordered.

697

Therefore, the phase transformation occurs within the size range of a unit cell of BPII<sub>{100}</sub> in (b)

698

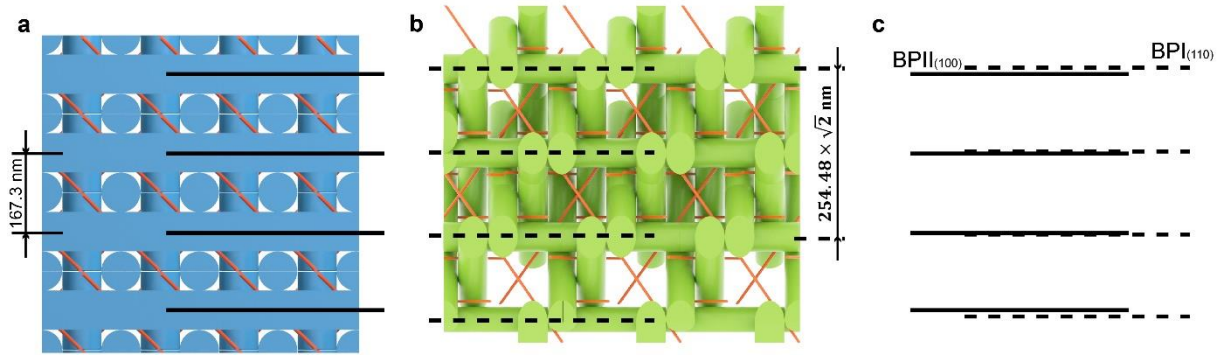
and without a transition region which may be attributed to that the DTCs diffusion first and

699

then reorganization when phase changes.

700

701



702

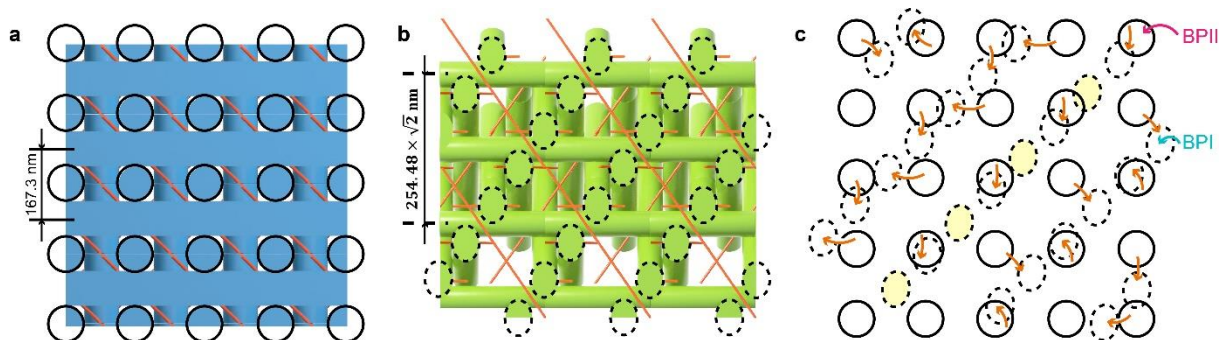
703 **Supplementary Fig. 43 a** Model of BPII unit cells with the [100] orientation out-of-plane. The axis of  
 704 horizontal DTCs is highlighted by black solid lines. **b** Model of BPI unit cells with the [110] orientation  
 705 out-of-plane. The axis of horizontal DTCs is highlighted by black dash lines. **c** The horizontal oriented  
 706 DTCs of  $BPII_{\{100\}}$  are parallel to that of  $BPI_{\{110\}}$ . The interval of horizontal DTCs between  $BPI_{\{110\}}$  and  
 707  $BPII_{\{100\}}$  are similar.

708

709 Clearly, nearly one-third of the DTCs in  $BPI_{\{110\}}$  [horizontal DTCs of  $BPI_{\{110\}}$  in (b)]  
 710 transfer from the horizontal DTCs of  $BPII_{\{100\}}$  (a). Since the space between adjacent horizontal  
 711 DTCs in  $BPII_{\{100\}}$  are similar to that of  $BPI_{\{110\}}$  (c), predicting the coherent lattice formation  
 712 between  $BPI_{\{110\}}$  and  $BPII_{\{100\}}$ . Supplementary Figs. 28c<sub>1</sub>, c<sub>4</sub>, 38b, and 39 show the clear  
 713 interfaces measured by TEM and the theoretically predicted arrangement of DTCs near the  
 714 interface between  $BPII_{\{100\}}$  and  $BPI_{\{110\}}$ , showing coherent lattice between  $BPII_{\{100\}}$  and  
 715  $BPI_{\{110\}}$ . Furthermore, the 2-Theta values measured by syn-SAXS corresponding to  $\{110\}_{BPII}$   
 716 and  $\{211\}_{BPI}$  are similar (Supplementary Figs. 46c<sub>3</sub>, e<sub>3</sub>, 47c<sub>1</sub>-d<sub>1</sub>, 48, 56d<sub>1</sub>-d<sub>4</sub>), proving coherent  
 717 of crystal lattice between  $\{110\}_{BPII}$  and  $\{211\}_{BPI}$  which is an evidence for the thermoelastic  
 718 martensitic transformation.

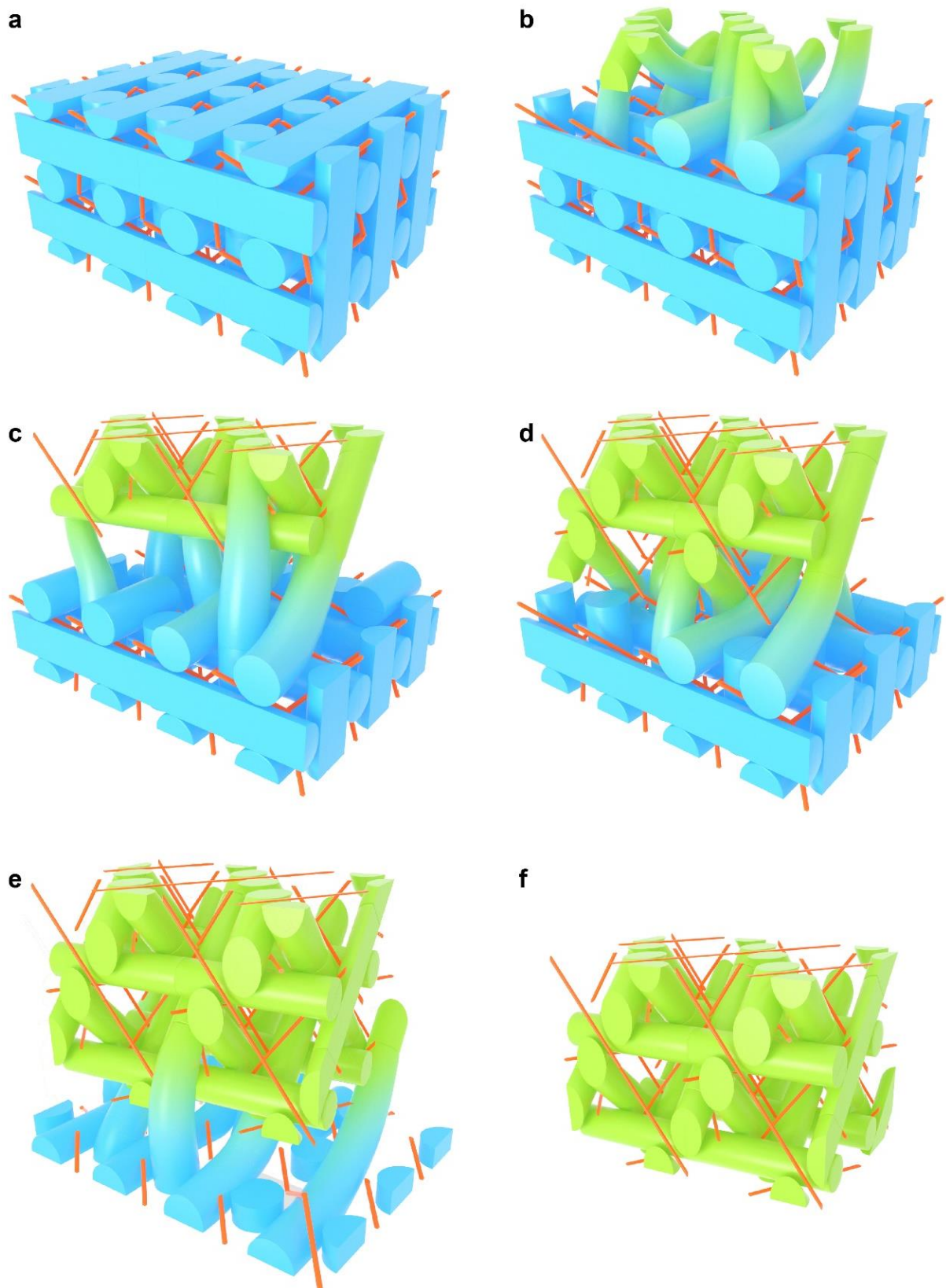
719

720



721  
 722 **Supplementary Fig. 44 Schematic image of the collective motion of DTCs during the phase**  
 723 **transformation from BPII to BPI.** **a** BPII unit cells with the [100] orientation out-of-plane. The solid  
 724 black circles highlight the position of DTCs with vertical orientation. **b** BPI unit cells with the [110]  
 725 orientation out-of-plane. The dash black ellipses highlight the position of DTCs with tilt orientation. **c** The  
 726 relationship between the vertical DTCs of BPI<sub>{110}</sub> and inclined DTCs of BPII<sub>{100}</sub> is evaluated by the  
 727 quantity and position of DTCs. The orange arrows highlight the predicted tendency of the rearrangement of  
 728 DTCs during the phase transformation of BPII/BPI.  
 729  
 730

731 As shown in the projected models, the vertical DTCs (solid circles) in BPII<sub>{100}</sub> (a) tend to  
 732 transfer to the inclined DTCs (dash circles) in BPI<sub>{110}</sub> (b). The orange arrows in (c) point out  
 733 the probable tendency of rearrangement of DTCs during the phase transformation from BPII to  
 734 BPI. However, the total number of inclined DTCs in BPI<sub>{110}</sub> is more than the vertical DTCs of  
 735 BPII<sub>{100}</sub> and the extra yellow ellipses shown in (c) may transfer from the horizontal DTCs of  
 736 BPII<sub>{100}</sub>.



737  
 738  
 739  
 740  
 741  
 742

**Supplementary Fig. 45** Models highlight the proposed mechanism of the collective move of DTCs during the thermoelastic martensitic transformation from  $BPII_{(100)}$  with 16 unit cells of  $(2 \times 2 \times 4)$  to  $BPI_{(110)}$ ,  $-9.74^\circ$ . **a**  $BPII_{(100)}$ . **b-e** The process of thermoelastic martensitic transformation from  $BPII_{(100)}$  to  $BPI_{(110)}$ . **f**  $BPI_{(110)}$ .

743       Based on the experiment results and analysis shown in Supplemental Figs. 33 and 52-53,  
744 the total process of rearrangement of DTCs during the thermoelastic martensitic transformation  
745 from  $\text{BPII}_{\{100\}}$  with 16 unit cells of  $(2 \times 2 \times 4)$  to  $\text{BPI}_{\{110\}}$  is shown in Figure 6 (in the main text).  
746 Several behavior of the rearrangement of DTCs are confirmed during the thermoelastic  
747 martensitic transformation of  $\text{BPII}/\text{BPI}$ : (i) the parent lattice of  $\text{BPII}$  needs to rotate  $9.74^\circ$ . (ii)  
748 nearly one-third of the horizontal DTCs of  $\text{BPII}_{\{100\}}$  tend to transfer to the horizontal DTCs of  
749  $\text{BPI}_{\{110\}}$ , resulting in the coherent lattice near the interface of  $\text{BPII}/\text{BPI}$ . (iii) the vertical DTCs  
750 in  $\text{BPII}_{\{100\}}$  tend to transfer to the tilt DTCs in  $\text{BPI}_{\{110\}}$ . The total number of tilt DTCs in  $\text{BPI}_{\{110\}}$   
751 is more than the vertical DTCs of  $\text{BPII}_{\{100\}}$ . The extra tilt DTCs of  $\text{BPI}_{\{110\}}$  may transfer from  
752 the horizontal DTCs of  $\text{BPII}_{\{100\}}$ .

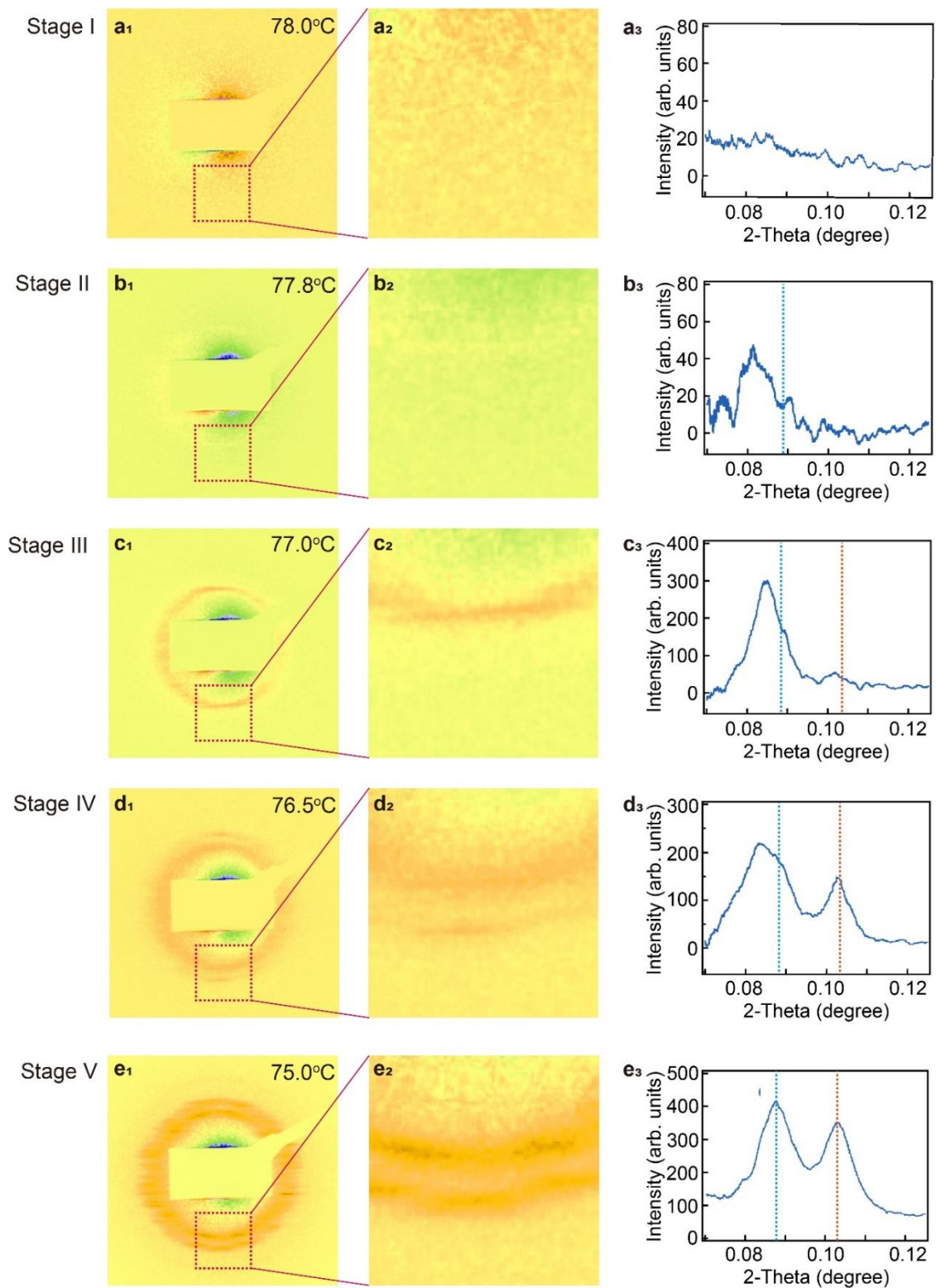
753

754

755

756 **Supplementary Note 5 Crystal analyses through syn-SAXS characterization of DLPT**

757 **based on PS-BPLCs**



758

759 **Supplementary Fig. 46 Crystal-crystal transformation during the DLPT measured from polymer-**  
 760 **stabilized polydomain BPLCs at distinct stages. a<sub>1</sub>-e<sub>1</sub> 2D-SAXS patterns with background subtracted.**  
 761 **a<sub>2</sub>-e<sub>2</sub> Enlarged images of the area highlighted by red squares in (a<sub>1</sub>-e<sub>1</sub>).** **a<sub>3</sub>-e<sub>3</sub> 1D-SAXS curves obtained by**  
 762 **90° azimuthal integral from (a<sub>1</sub>-e<sub>1</sub>).**

763

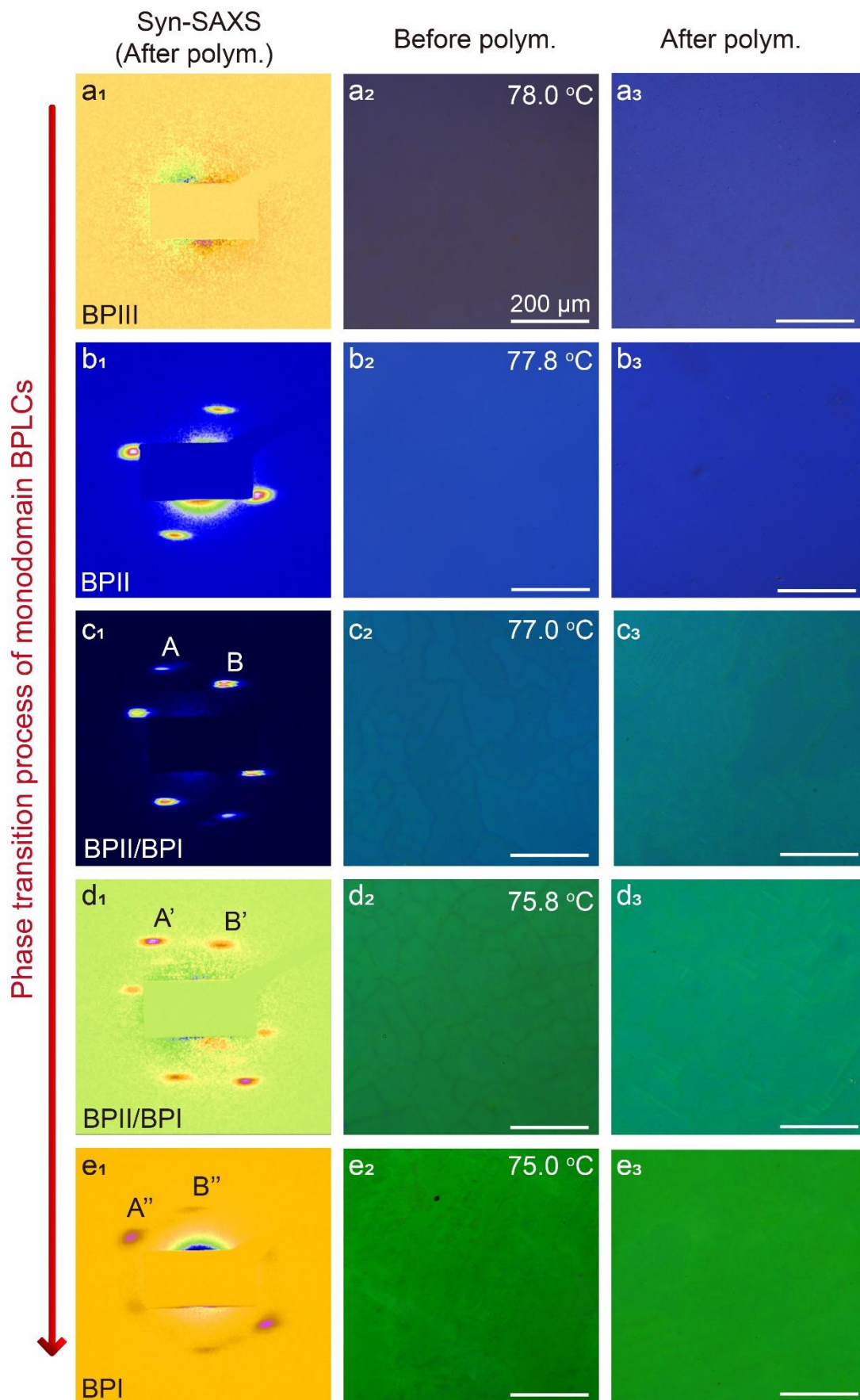
764 Polydomain PS-BPLCs are characterized by syn-SAXS at each stage which provides a  
765 macroscopic view on the crystal-crystal transformation. The 2D-SAXS patterns and  
766 corresponded 1D-SAXS curve are shown here. Stage I ( $a_1$ - $a_3$ ) is BPIII embedded in an isotropic  
767 background without diffraction speckle ( $a_1$ ) or peak in the 1D-SAXS curve ( $a_3$ ) owing to BPIII  
768 has similar symmetry to the isotropic state<sup>9</sup>. Stage II ( $b_1$ - $b_3$ ) consists of BPIII domains and  
769 BPIII/BPII core-shell configurations, giving a weak diffraction ring of BPII in the 2D-SAXS  
770 pattern ( $b_2$ ), and an obvious peak is detected at  $2\theta=0.0812^\circ$  in the 1D-SAXS curve ( $b_3$ ). Stages  
771 III ( $c_1$ - $c_3$ ) composes of the BPIII domains and core-shell configurations of BPIII/BPII,  
772 BPIII/BPI, and BPIII/BPII/BPI. In this case, more residual BPIII transfers to BPII which  
773 attributes to the intensity increase of BPII at  $2\theta=0.0847^\circ$ . Due to the small amount of BPI  
774 nucleates in the center of BPII and BPIII domains, a diffraction peak of  $\{310\}_{BPI}$  can be  
775 observed around  $2\theta=0.1020^\circ$  ( $c_3$ ). Stage IV ( $d_1$ - $d_3$ ) only composes of BPIII/BPII/BPI core-  
776 shell configurations. In this stage, all of BPIII/BPI core-shell configurations have transferred to  
777 BPIII/BPII/BPI core-shell configurations where more BPIII transferred to BPII or BPI.  
778 Therefore, both diffraction rings of BPII and BPI become stronger ( $d_2$ ). In the 1D-SAXS curve,  
779 the peak belonging to  $\{310\}_{BPI}$  is located at  $2\theta=0.1028^\circ$  whereas the peak at  $2\theta=0.085^\circ$   
780 belongs to the overlapped two peaks of  $\{110\}_{BPII}$  and  $\{211\}_{BPI}$ . The peaks of  $\{110\}_{BPII}$  and  
781  $\{211\}_{BPI}$  are almost overlapped where the details will be discussed in the following context  
782 (Supplementary Figs. 47-48). Stage V indicates a complete transition of the sample from BPIII,  
783 BPII to BPI ( $e_1$ - $e_3$ ), and two diffraction rings can be observed in 2D-SAXS, in which the inner  
784 ring originates from  $\{211\}_{BPI}$  and the outer ring originates from  $\{310\}_{BPI}$ . In the 1D-SAXS  
785 curve, the peak of  $\{310\}_{BPI}$  is located at  $2\theta=0.1030^\circ$  whereas the peak located at  $2\theta=0.0874^\circ$   
786 belongs to  $\{110\}_{BPII}$ . The blue and orange dotted lines shown in ( $a_3$ - $e_3$ ) highlights the center  
787 wavelength of two diffraction peaks. Clearly, both peaks of BPI and BPII shift to large angles  
788 which represent the shrinkage of the crystal lattice during the phase transition process from  
789 Stage I to V. With the emergence of BPI, a newly appeared diffraction ring can be observed in



790 (c<sub>2</sub>) and (d<sub>2</sub>). However, when BPII completely transfers to BPI (Stage V), two rings of {211}<sub>BPI</sub>  
791 and {310}<sub>BPI</sub> (e<sub>2</sub>) are presented in monophasic BPI, proving the overlapping of the diffraction  
792 ring of {211}<sub>BPI</sub> and {110}<sub>BPII</sub> which will be further investigated in Supplementary Figures 47-  
793 48.

794 During the phase transition process, the sharp diffraction rings of both BPI and BPII  
795 without diffuse scattering are observed, indicating that a sudden reconfiguration without  
796 transitional region exists near the interface between BPII and BPI.

797

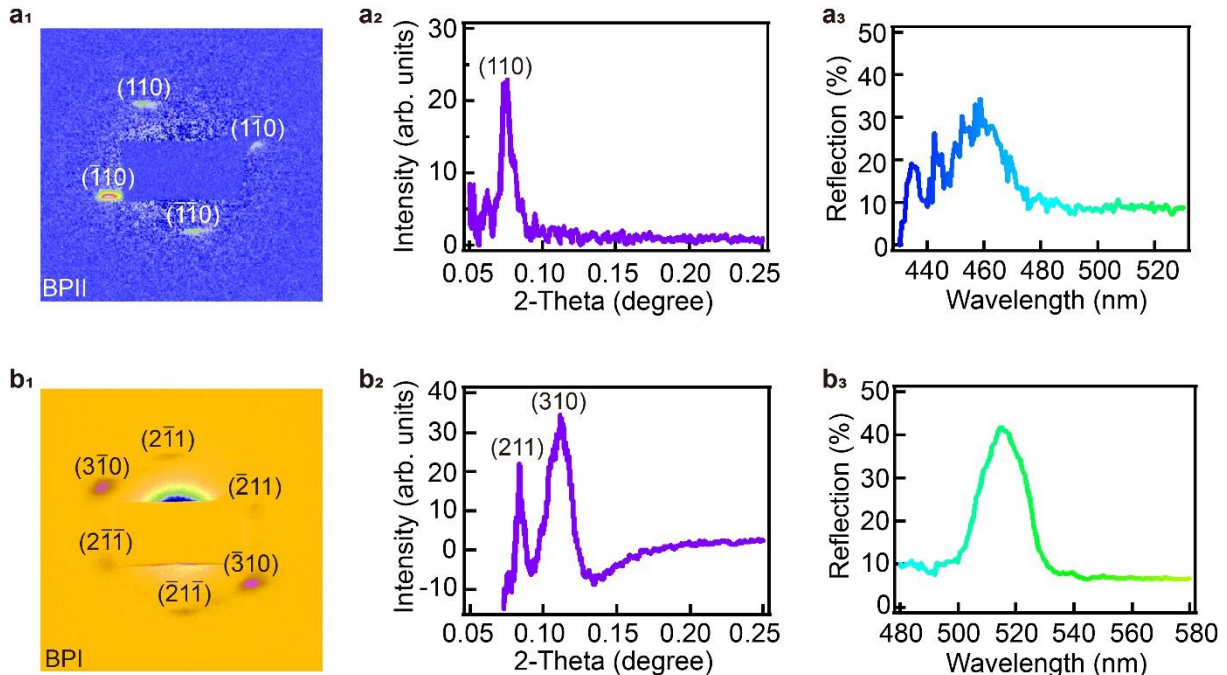


798  
799  
800

**Supplementary Fig. 47** **a<sub>1</sub>-e<sub>1</sub>** Syn-SAXS patterns and POM characterization of monodomain BPLCs (**a<sub>2</sub>-e<sub>2</sub>**) before and (**a<sub>3</sub>-e<sub>3</sub>**) after polymer-stabilization.

801 To further index the diffraction rings during the phase transition process of polydomain  
802 BPLCs (Supplementary Fig. 46), syn-SAXS and temperature-dependent POM are performed  
803 on monodomain BPLCs (Supplementary Movie 3). During the phase transition process, no  
804 diffraction pattern is observed for polymer-stabilized BPIII (a<sub>1</sub>-a<sub>3</sub>). Four-fold symmetry  
805 diffraction speckles are obtained in polymer-stabilized BPII (b<sub>1</sub>-b<sub>3</sub>). The diffraction speckles  
806 labeled with A belongs to the BPI in the hybrid phases of BPI/BPII, which is polymerized at  
807 77.0 °C (c<sub>1</sub>-c<sub>3</sub>). Speckle labeled with A' is enhanced while speckle labeled with B' is weakened,  
808 owing to the growth of BPI and the gradual disappearance of BPII in a hybrid phase of BPI/BPII  
809 polymerized at 75.8 °C (d<sub>1</sub>-d<sub>3</sub>). Speckles labeled with A'' and B'' are observed in monodomain  
810 BPI polymerized at 75.0 °C (e), in which all the BPII in (c-d) has transferred to BPI, indicating  
811 the speckles of BPII labeled with B and B' are overlapped by those of BPI labeled with B''.  
812 Thus, a similar *q* values and fixed azimuthal angle between BPII and BPI are confirmed  
813 according to the gradual fading from B, B' to B'' and enhancement from A, A' to A''.  
814  
815

816



817

818

819

820

821

822

823

824

**Supplementary Fig. 48 Syn-SAXS results and the corresponding reflection spectra of (a) BPII and (b) BPI. a<sub>1</sub>, b<sub>1</sub> 2D-SAXS patterns with background subtracted of BPII<sub>{100}</sub> (a<sub>1</sub>) and BPI<sub>{110}</sub> (b<sub>1</sub>). a<sub>2</sub>, b<sub>2</sub> 1D-SAXS curves obtained by 90° azimuthal integral from 2D-SAXS patterns of BPII<sub>{100}</sub> (a<sub>1</sub>) and BPI<sub>{110}</sub> (b<sub>1</sub>). a<sub>3</sub>, b<sub>3</sub> *In situ* reflection spectra of the same area as the samples used to measure 2D-SAXS patterns of (a<sub>1</sub>) BPII<sub>{100}</sub> and (b<sub>1</sub>) BPI<sub>{110}</sub>.**

825

826

827

828

829

830

831

832

833

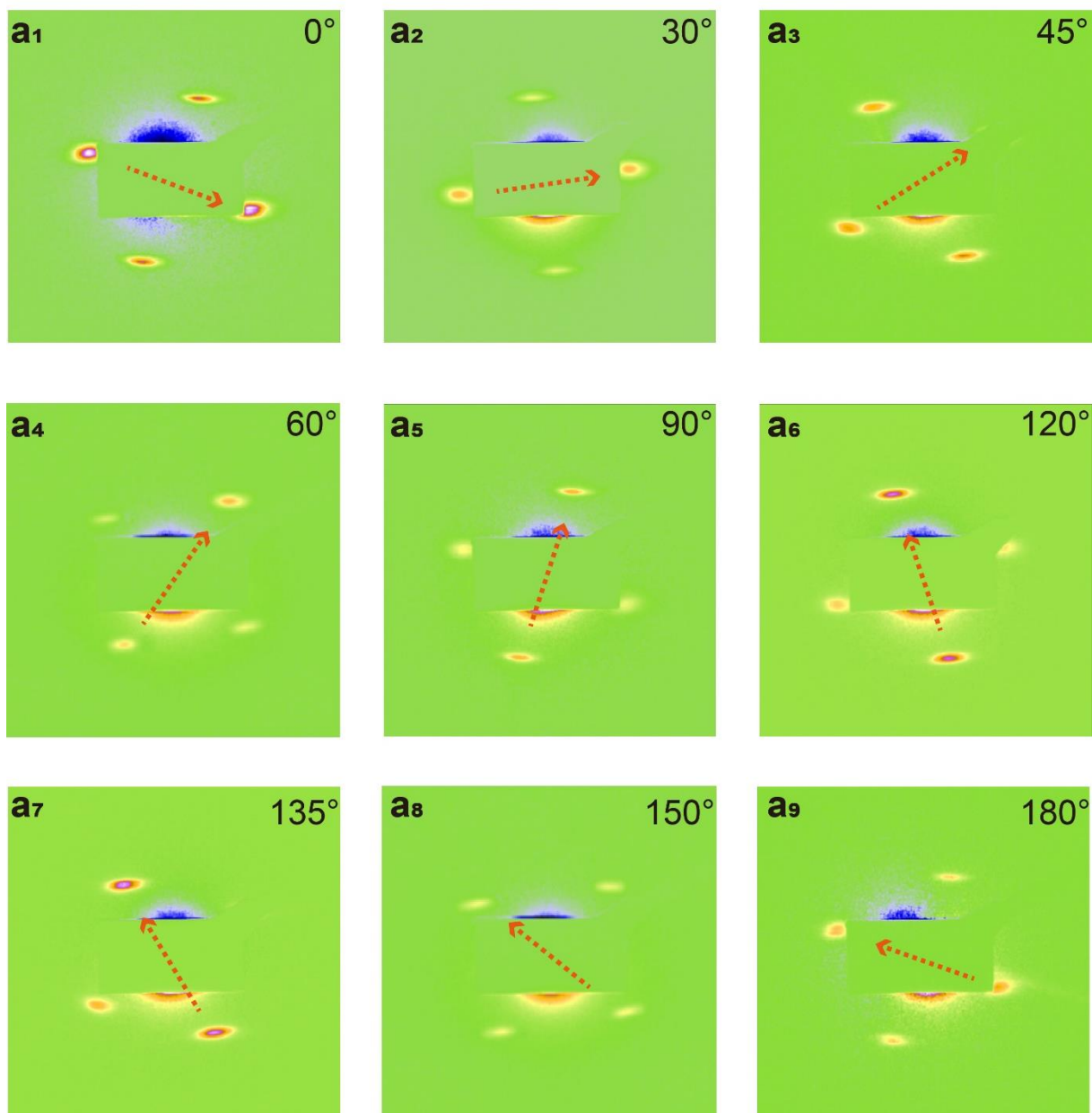
834

835

836

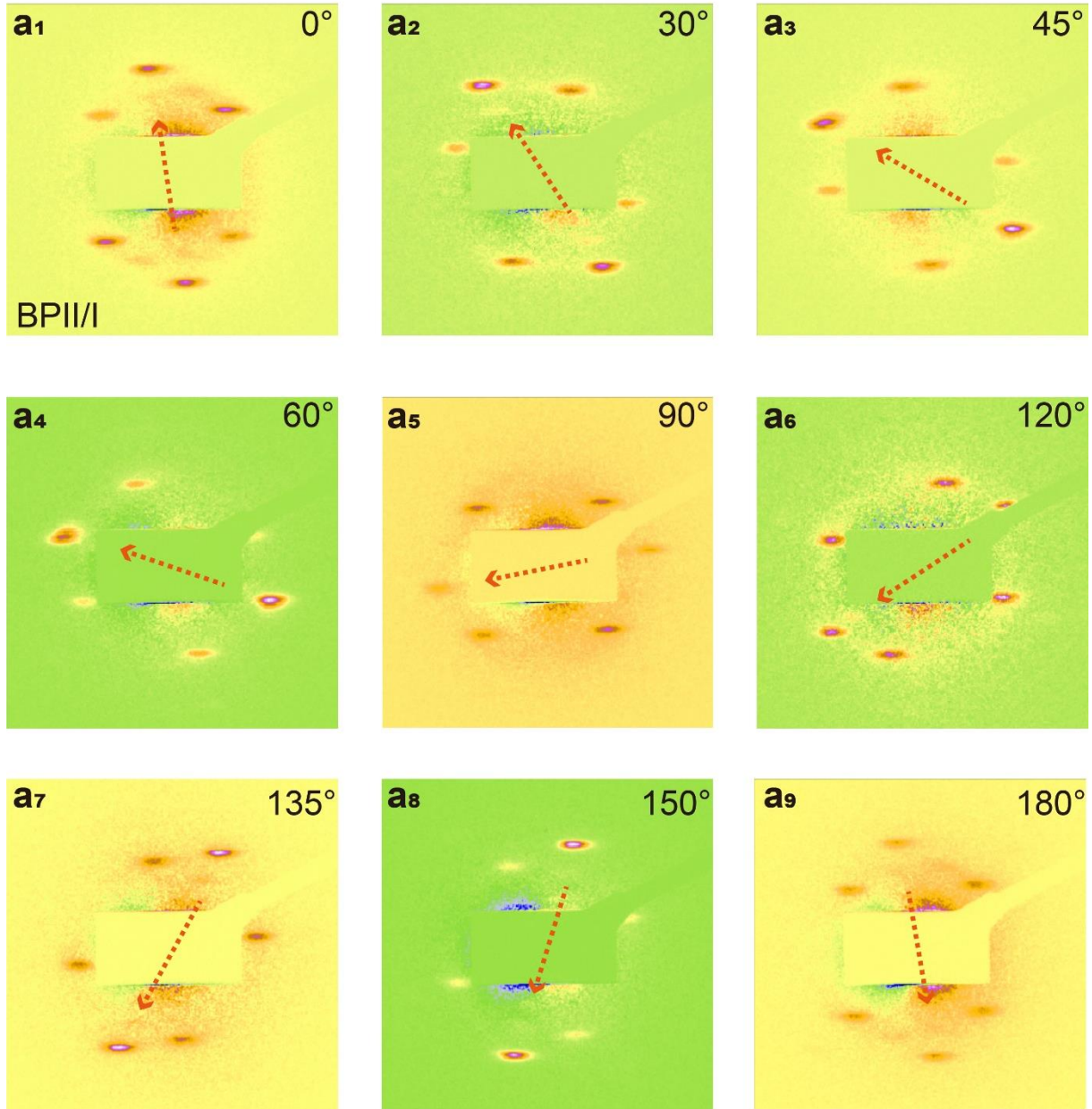
Syn-SAXS results and the corresponding reflection spectra of monodomain BPII<sub>{100}</sub> and BPI<sub>{110}</sub> have been measured along the normal direction. Four diffraction spots of {110}<sub>BPII</sub> are observed in (a<sub>1</sub>). Systematic extinctions of BPII are observed on {h00} when the obtained indexed pattern corresponds to the selection rule:  $h = n$  ( $n$  is an odd number). One diffraction peak located at  $2\theta = 0.0746^\circ$  (a<sub>2</sub>) is obtained by 90° azimuthal integral from 2D-SAXS patterns of BPII (a<sub>1</sub>). The lattice content of BPII is 167.33 nm calculated by Bragg's equation:  $\lambda = 2d_{(hkl)}\sin\theta$  ( $\lambda$ : wavelength of synchrotron radiation X-ray which is 1.54 Å;  $d_{(hkl)}$ : interplanar distance calculated by  $d_{(hkl)} = \frac{a}{\sqrt{h^2+k^2+l^2}}$ ;  $\theta$ : diffraction angle). The corresponding  $\lambda_c$  of BPII<sub>{110}</sub> is located at 459 nm obtained by *in situ* reflection spectrum (a<sub>3</sub>). Six diffraction spots belonging to {211}<sub>BPI</sub> and {310}<sub>BPI</sub> are observed in (b<sub>1</sub>). Systematic extinctions of BPI observed on the obtained indexed pattern correspond to the selection rule:  $h + k + l = n$  ( $n$  is an odd number) for {hkl} and  $k + l = n$  ( $n$  is an odd number) for {0kl}. Two diffraction

837 peaks are obtained by  $90^\circ$  azimuthal integral from 2D-SAXS patterns of  $\text{BPI}_{\{110\}}$  ( $b_1$ ). The  
838 diffraction peak belongs to  $\{211\}_{\text{BPI}}$  is located at  $2\theta=0.0835^\circ$  and  $\{310\}_{\text{BPI}}$  located at  
839  $2\theta=0.1096^\circ$  ( $b_2$ ). The lattice content of BPI calculated from  $\{211\}_{\text{BPI}}$  ( $2\theta=0.0835^\circ$ ) is 258.87  
840 nm while the crystal lattice calculated from  $\{310\}_{\text{BPI}}$  ( $2\theta=0.1096^\circ$ ) is 254.48 nm. Owing to  
841 lattice constant calculated from  $\{310\}_{\text{BPI}}$  is located at a higher angle in the 1D-SAXS curve  
842 which has a smaller systematical error than that of  $\{211\}_{\text{BPI}}$ , the crystal lattice calculated from  
843  $\{310\}_{\text{BPI}}$  is more precise. The corresponding *in situ* reflection spectrum of  $\text{BPI}_{\{110\}}$  indicates  
844 the  $\lambda_c$  is located at 518 nm.



845  
 846 **Supplementary Fig. 49 2D-SAXS patterns with background subtracted of monodomain polymer-**  
 847 **stabilized BPII. a<sub>1</sub>-a<sub>9</sub>** The film is rotated from 0° to 180° in {100} crystal plane of BPII. The dotted arrows  
 848 highlight the angle during rotation.  
 849

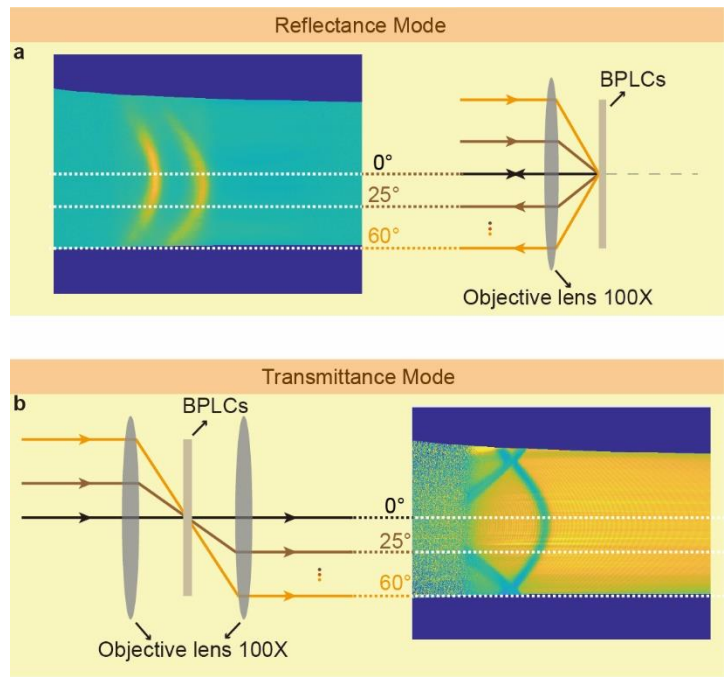
850 To further verify the monodomain BPII<sub>{100}</sub> is a single crystal, the angle-dependent syn-  
 851 SAXS patterns are measured by rotating the sample in {100}<sub>BPII</sub> from 0° to 180°. The four clear  
 852 diffraction spots of {110}<sub>BPII</sub> rotate with the sample which confirms BPII<sub>{100}</sub> a single crystal.  
 853



854  
 855 **Supplementary Fig. 50 2D-SAXS patterns with background subtracted of hybrid monodomain**  
 856 **BPI/BPII.** **a<sub>1</sub>-a<sub>9</sub>** The film is rotated from 0° to 180° in  $\{110\}_{\text{BPI}}$  and  $\{100\}_{\text{BPII}}$ . The dotted arrows highlight  
 857 the angle during rotation.  
 858

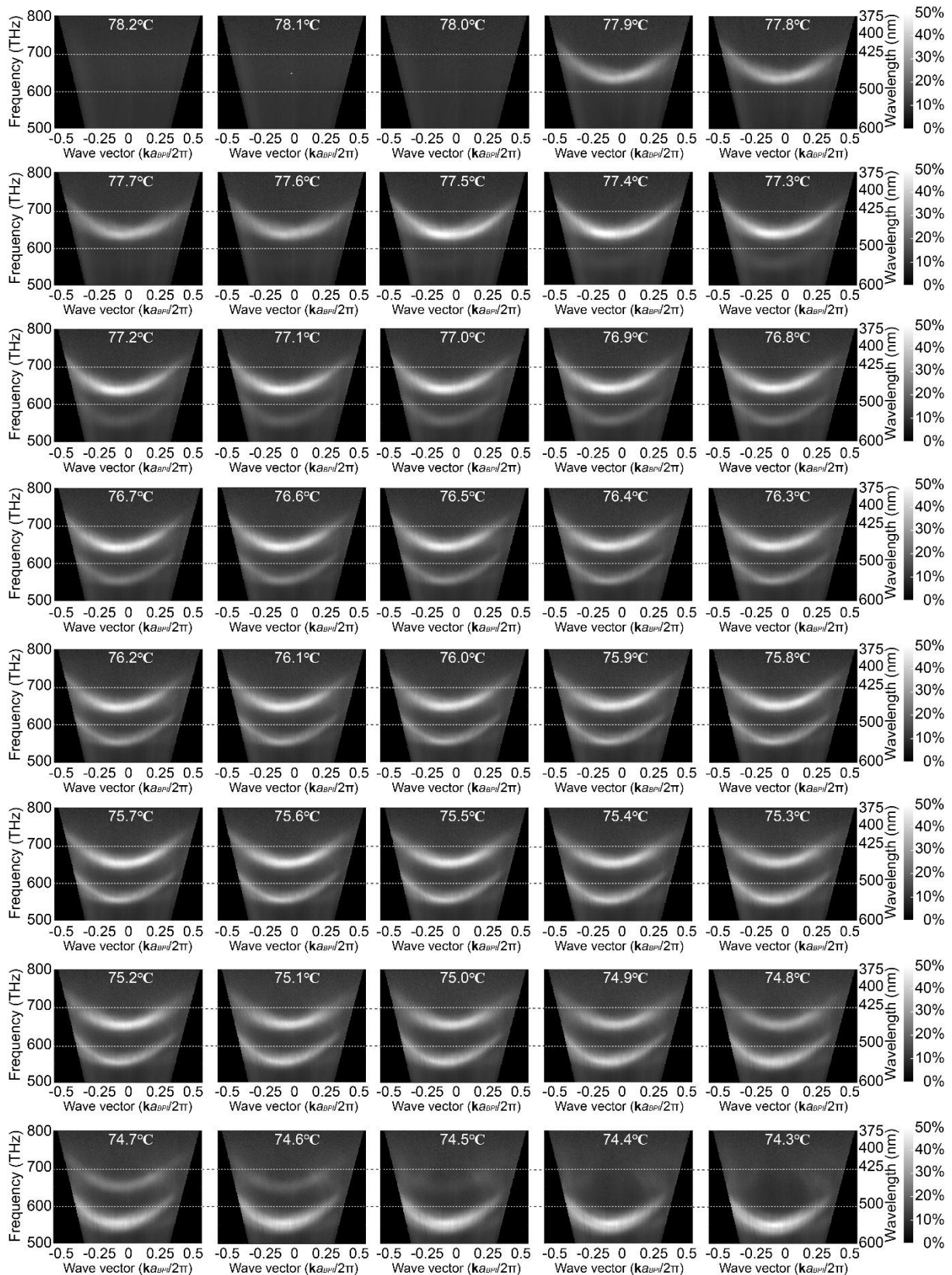
859 To further verify the monodomain BPLCs with hybrid phases of  $\text{BPI}_{\{110\}}$  and  $\text{BPII}_{\{100\}}$   
 860 obtained during the phase transition process) is a single crystal. The angle-dependent syn-SAXS  
 861 patterns are measured by rotating the sample in the normal direction from 0° to 180°. The  
 862 diffraction spots rotate with the film, which confirms both  $\text{BPI}_{\{110\}}$  and  $\text{BPII}_{\{100\}}$  in a hybrid  
 863 phase are single crystals. Due to the temperature gradient along thickness direction in an LC  
 864 cell on the heat stage, the single crystal of  $\text{BPI}_{\{110\}}$  and  $\text{BPII}_{\{100\}}$  mixture should exhibit a  
 865 layered structure where  $\text{BPI}_{\{110\}}$  at the bottom is covered by  $\text{BPII}_{\{100\}}$ .

866 **Supplementary Note 6 ARM characterization of phase transition of BPLCs**



867  
868 **Supplementary Fig. 51 Experiment setup of ARM under the inverted optical microscope in (a)**  
869 **transmission or (b) reflection mode.** Schematic views of light paths and the examples of ARM results are  
870 shown.  
871

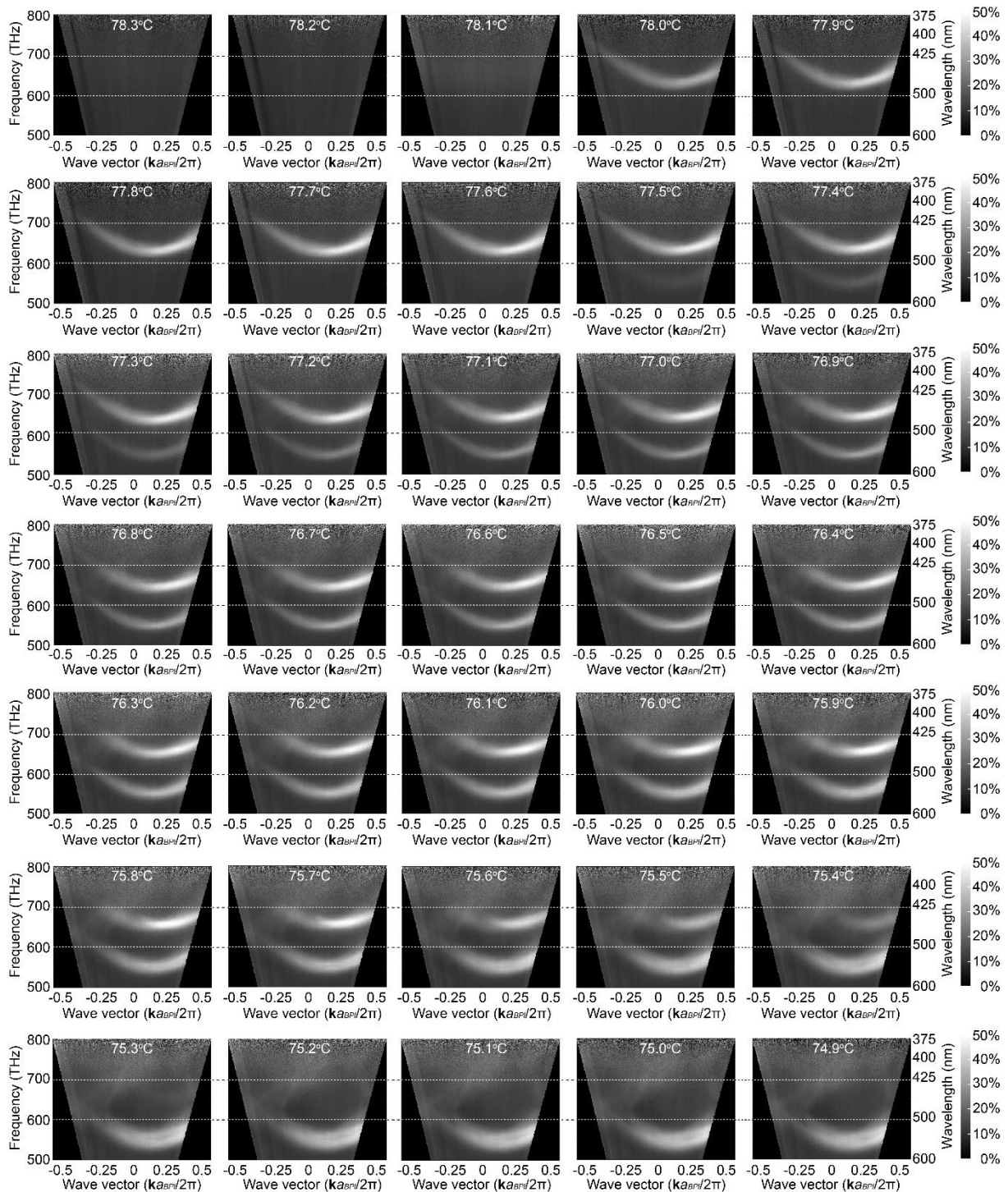




872  
873  
874  
875  
876  
877

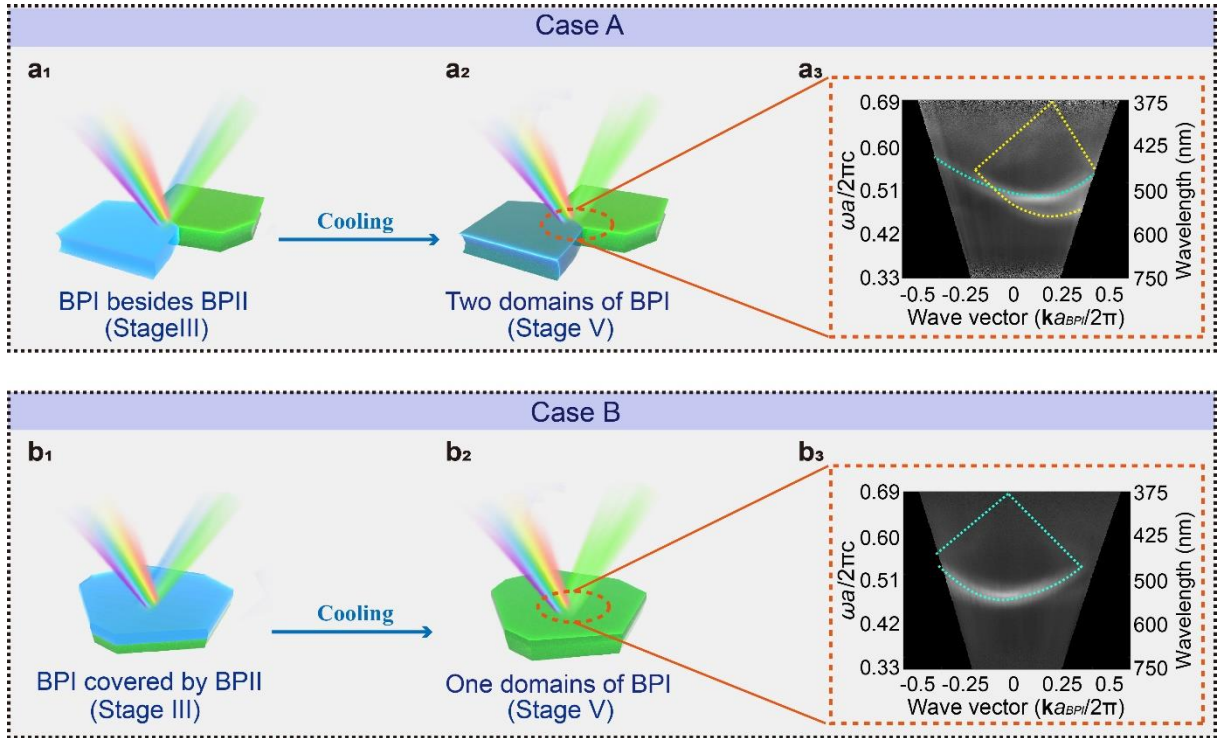
**Supplementary Fig. 52** *In situ* observation of the measured reflectance of polydomain BPLCs during the temperature reduction process from Stage I to V. The color scale indicates the reflectivity of the measured area. The colour scale on the right side of each row is also available for the five spectra in which row.

878 Here, *in situ* dynamic track of the polydomain BPLCs is carried out by angle-resolved  
879 microspectroscopy (ARM). During the temperature reduction from a clear point to 78.0 °C, no  
880 streak is observed at Stage I (BPIII nuclei in the isotropic background) owing to BPIII is an  
881 amorphous structure without bandgaps. When temperature reduces to 77.9 °C, a bright  
882 reflection streak appears around 637 THz (463 nm, normalized frequency of peak near the  
883 normal incident angle ( $f_{nor}$ ) of 0.36), representing the emergence of BPII<sub>{100}</sub> at Stage II.  
884 Another streak around 554 THz (541 nm,  $f_{nor}=0.47$ ) at 77.6 °C belongs to BPI<sub>{110}</sub>. The  
885 coexisting of two streaks represent the coexistence of BPI<sub>{110}</sub> and BPII<sub>{100}</sub>. In this case, the  
886 center of streak located around 554 (637) THz originates from the [110] ([100]) direction of  
887 BPI (BPII). It is confirmed that {110}<sub>BPI</sub> is parallel to {100}<sub>BPII</sub> within the temperature range  
888 of 77.3 to 75.6 °C owing to the matched center of two streaks, indicating that the orientation of  
889 BPI<sub>{110}</sub> crystal lattice can be guided by the orientation of BPII<sub>{100}</sub> crystal lattice. With the  
890 further growth of BPI<sub>{110}</sub>, the anticrossings of BPI<sub>{110}</sub> become more clear from 74.8 °C. During  
891 the cooling process, the centers of two streaks have a slight mismatch within the temperature  
892 range of 75.5 to 75.2 °C, which is caused by the slight rotation of {100}<sub>BPII</sub> while the orientation  
893 of {110}<sub>BPI</sub> remains unchanged. Finally, the streak of BPII<sub>{100}</sub> vanishes at 74.5 °C and only  
894 one streak of BPI<sub>{110}</sub> is observed at 74.4 °C which indicates BPII transfers to BPI completely.  
895



896

897 **Supplementary Fig. 53** *In situ* observation of the measured reflectance of polydomain BPLCs during the  
 898 temperature reduction process from Stage I to V, which is similar to Supplementary Fig. 52. The color  
 899 scale indicates the reflectivity of the measured area. The colour scale on the right side of each raw is also  
 900 available for the five spectra in which raw.  
 901  
 902  
 903  
 904



905  
 906 **Supplementary Fig. 54 Determination of core-shell configuration during the phase transition process.**  
 907 **a<sub>1</sub>-a<sub>3</sub>** Case A for prediction of nucleation point of BPI<sub>{110}</sub> domain next to BPII<sub>{100}</sub> domain at Stage III (**a<sub>1</sub>**),  
 908 Stage V (**a<sub>2</sub>**) obtained by cooling from (**a<sub>1</sub>**), and the contour plot of reflection spectra (**a<sub>3</sub>**) obtained from the  
 909 interface between the two domains of BPI with distinct orientation. **b<sub>1</sub>-b<sub>3</sub>** Case B for prediction of  
 910 nucleation point of BPI<sub>{110}</sub> covered by BPII<sub>{100}</sub> at Stage III (**b<sub>1</sub>**), Stage V (**b<sub>2</sub>**) obtained by cooling from  
 911 (**b<sub>1</sub>**), and the resulted contour plot of reflection spectra (**b<sub>3</sub>**).  
 912

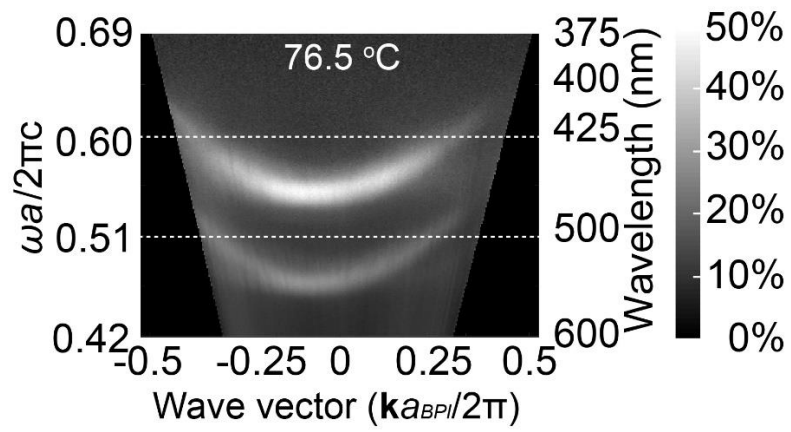
913 According to *in situ* measurement results of ARM (reflectance captured at 77.4 °C to 74.6 °C  
 914 in Supplementary Fig. 52 and 77.5 °C to 75.1 °C in Supplementary Fig. 53), two streaks are  
 915 observed spontaneously indicating that BPI<sub>{110}</sub> and BPII<sub>{100}</sub> coexist in the measured region  
 916 and the {110}<sub>BPI</sub> is observed approximate parallel to {100}<sub>BPII</sub> during the phase transition  
 917 process. However, the nucleation and growth sites of BPI are still unclear.

918 Here, two possible existing cases are presented for the nucleation and growth site of BPI  
 919 and BPII: side-by-side (Case A) or core-shell (Case B) configuration. Case A represents that  
 920 BPI and BPII are located side-by-side at Stage III (**a<sub>1</sub>**). To obtain a similar contour plot with  
 921 two streaks of BPI and BPII (Supplementary Fig. 55) which is obtained by *in situ* ARM  
 922 (Supplementary Fig. 52), the incident light is required to be at the interface between BPI and  
 923 BPII (**a<sub>1</sub>**) according to the ARM test principle. When Stage III (**a<sub>1</sub>**) is cooled to Stage V (**a<sub>2</sub>**),  
 924 BPII domain will transfer to BPI and form a new BPI domain with distinctive orientation, which

925 is always distinct from the existing BPI domain in (a<sub>1</sub>). The position of incident light is kept  
926 unchanged during the phase transition process, and the interface of two BPI domains with  
927 distinct orientations (a<sub>2</sub>) should be measured. Owing to the distinctive reflection streak for  
928 particular crystal orientation, two sets of curves overlapped will be predicted (a<sub>3</sub>). However,  
929 this case is inconsistent with the experimental results (reflectance captured at 74.4 °C to 74.3 °C  
930 in Supplementary Fig. 52 and 75.0 °C to 74.9 °C in Supplementary Fig. 53), suggesting case A  
931 is non-existing in the experiment.

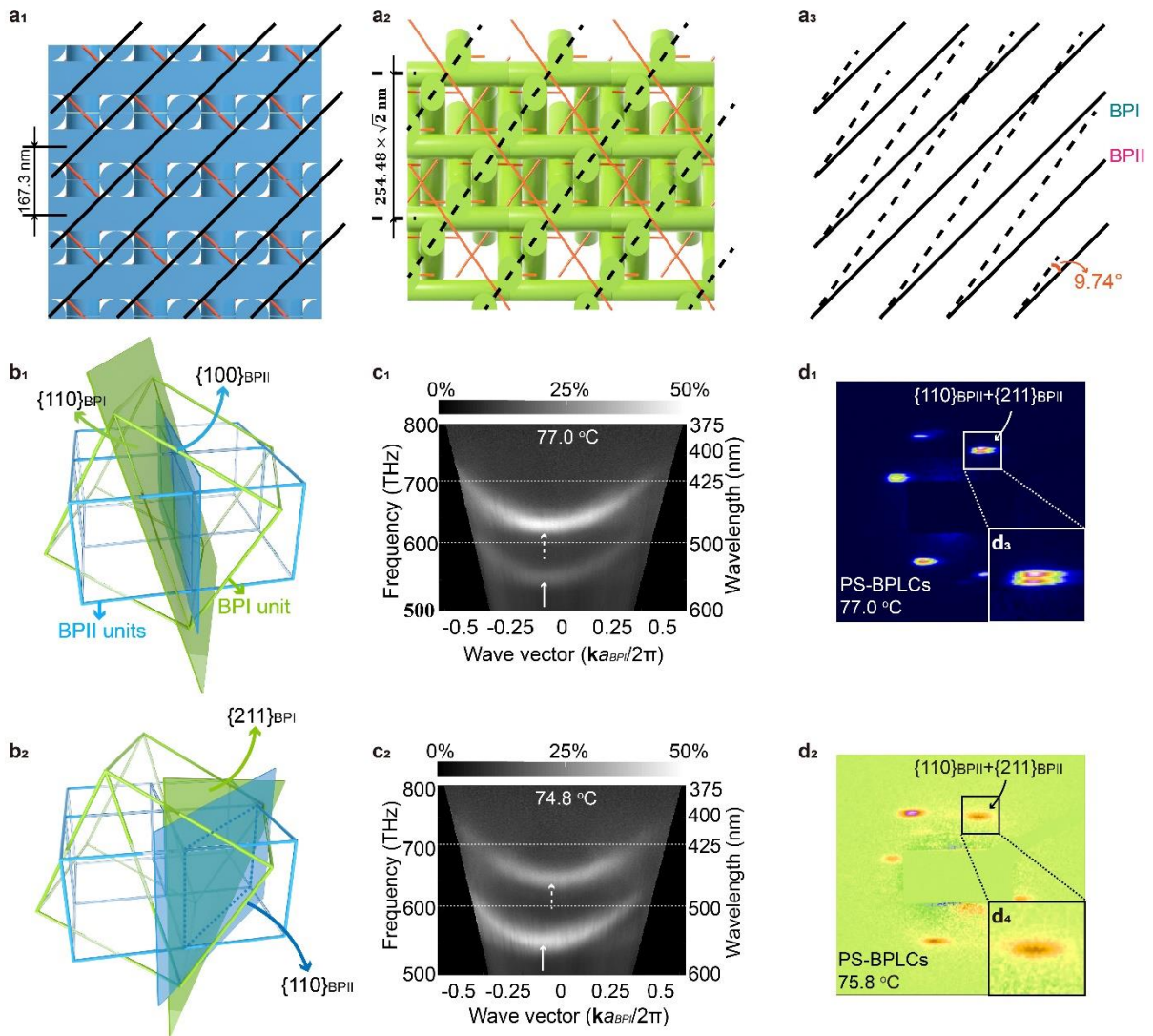
932 In Case B, the phase transition of BPLCs is supposed to be a core-shell configuration (Case  
933 B) where the BPI domain is covered by the BPII domain, and BPI nucleates in the center of  
934 BPII. In such a case, to obtain a rational contour plot with two streaks of BPI and BPII  
935 (Supplementary Fig. 55) which is obtained by in situ ARM (Supplementary Fig. 52), the  
936 incident light can be in the intermediate regions of the core-shell configuration (a<sub>1</sub>). After Stage  
937 III (b<sub>1</sub>) is cooled to Stage V (b<sub>2</sub>), BPII will transfer to BPI and forms only one BPI domain,  
938 achieving the same orientation as the BPI domain existed in Stage III (b<sub>1</sub>). Since the position  
939 of incident light is maintained at the same point in (b<sub>1</sub>), only one BPI domain can be measured,  
940 exhibiting only one sharp streak observed at Stage V (b<sub>3</sub>). Due to the agreement between Case  
941 B and experiment results in core-shell configuration (b<sub>3</sub>) (reflectance captured at 74.4 °C to  
942 74.3 °C in Supplementary Fig. 52 and 75.0 °C to 74.9 °C in Supplementary Fig. 53), the core-  
943 shell configuration of BPI covered by BPII can be confirmed by ARM measurement during *in-*  
944 *situ* dynamic track of the phase transition process.

945  
946



947  
 948  
 949  
 950  
 951  
 952

**Supplementary Fig. 55** Contour plots of measured reflectance of Case B at Stage III of Supplementary Fig. 54. The color scale indicates the reflectivity of the measured area.



953  
954  
955  
956  
957  
958  
959  
960  
961  
962  
963  
964  
965  
966  
967  
968  
969  
970  
971  
972  
973  
974  
975

**Supplementary Fig. 56 Lattice orientation relationships between BPI and BPII experienced a thermoelastic martensitic transformation.** **a<sub>1</sub>** BPII unit cells with the [100] orientation out-of-plane. The black solid lines connect the centers of DTCs with vertical orientation in BPII. **a<sub>2</sub>** BPI unit cells with the [110] orientation out-of-plane. The black dash lines connect the centers of DTCs with tilt orientation in BPI. **(a<sub>3</sub>)** Schematic of the angle between the solid lines of BPII and the dash lines of BPI which is 9.74°. **b<sub>1</sub>** {100} crystal plane of BPII ( $\{100\}_{\text{BPII}}$ ) is approximately parallel to {110} crystal plane of BPI ( $\{110\}_{\text{BPI}}$ ) while there is a small angle between them. **b<sub>2</sub>** Schematic illustration of the orientation relationship between BPI and BPII where  $\{110\}_{\text{BPII}}$  is parallel to  $\{211\}_{\text{BPI}}$ . **c<sub>1</sub>** ARM result of BPLCs captured at 77.0 °C (Stage III) exhibit a well-matched dip between the  $\{110\}_{\text{BPI}}$  streak with  $\{100\}_{\text{BPII}}$  streak. The arrows highlight the centers of the streaks. The color scale indicates the reflectivity of the measured area. **c<sub>2</sub>** ARM result of BPLCs captured at 74.8 °C (Stage IV) exhibits a slightly mismatched center of the  $\{110\}_{\text{BPI}}$  streak in relation to  $\{100\}_{\text{BPII}}$ . As the center of  $\{110\}_{\text{BPI}}$  streak does not shift, the mismatch may be caused by the rotation of  $\{100\}_{\text{BPII}}$ , resulting in a small angle between the approximately paralleled  $\{100\}_{\text{BPII}}$  and  $\{110\}_{\text{BPI}}$ . The arrows highlight the centers of the streaks. **d<sub>1</sub>** Syn-SAXS pattern measured from the BPLCs with BPI $_{\{110\}}$  and BPII $_{\{100\}}$  in coexistence, which is polymer-stabilized at 77.0 °C. **d<sub>2</sub>** Syn-SAXS pattern measured from the BPLCs with BPI $_{\{110\}}$  and BPII $_{\{100\}}$  in coexistence, which is polymer-stabilized at 75.8 °C. **d<sub>3</sub>** The speckles of BPI $_{\{211\}}$  and BPII $_{\{110\}}$  are relatively close but do not overlap, indicating that the  $\{110\}_{\text{BPII}}$  is approximately parallel to  $\{211\}_{\text{BPI}}$  with a small angle at an early stage during the phase transition process. **d<sub>4</sub>** The speckles of  $\{211\}_{\text{BPI}}$  and  $\{110\}_{\text{BPII}}$  are well overlapped, indicating that  $\{110\}_{\text{BPII}}$  and  $\{211\}_{\text{BPI}}$  are parallel.

976 As shown in (a<sub>1</sub>-a<sub>2</sub>), the black solid lines connect the center of DTCs with vertical  
 977 orientation in BPII<sub>{100}</sub> while the black dash lines connect the center of DTCs with tilt  
 978 orientation in BPI<sub>{110}</sub>. There is an angle of 9.74° (=arccos $\frac{\sqrt{3}}{3}$ -45°) between the black solid lines  
 979 highlighted in BPII<sub>{100}</sub> (a<sub>1</sub>) and the black dash lines shown in BPI<sub>{110}</sub> (a<sub>2</sub>) is observed in the  
 980 projected models (a<sub>3</sub>), predicting that an angle of 9.74° between BPI<sub>{110}</sub> and BPII<sub>{100}</sub> is  
 981 required during the thermoelastic martensitic transformation. It is hypothesized that the vertical  
 982 DTCs in BPII<sub>{100}</sub> tend to form the vertical DTCs in BPI<sub>{110}</sub> during the cooling process. Since  
 983 the molecules are relatively free to move, the diffusionless fuse and merge of DTCs<sup>2</sup> rearrange  
 984 through local molecular twist and reorientation. When the vertical DTCs in BPII<sub>{100}</sub> transfer  
 985 to the tilted DTCs in BPI<sub>{110}</sub>, the molecular of DTCs in BPII<sub>{100}</sub> can twist the smallest angle  
 986 to form DTCs in BPI<sub>{110}</sub> which is an energy favor process. The rotation of the azimuthal angle  
 987 is further proved by syn-SAXS and ARM results (c-d).

988 It is observed that the dips of BPI<sub>{110}</sub> and BPII<sub>{100}</sub> streaks are well-matched at an early  
 989 stage [77.0 °C in (c<sub>1</sub>)] of the phase transformation, proving that {110}<sub>BPI</sub> // {100}<sub>BPII</sub>. When the  
 990 phase transition is at the last stage [(74.8 °C in (c<sub>2</sub>))], a small deviation of the dips is observed,  
 991 resulting in a small angle of 9.74° appears between {110}<sub>BPI</sub> and {100}<sub>BPII</sub> (b<sub>1</sub>). In this case, the  
 992 {211}<sub>BPI</sub> // {110}<sub>BPII</sub> is predicted (b<sub>2</sub>). It can be seen that the dip of BPI<sub>{110}</sub> does not change  
 993 while that of BPII<sub>{100}</sub> has rotated which means the rotations of the parent lattice are required  
 994 during the thermoelastic martensitic transformation.

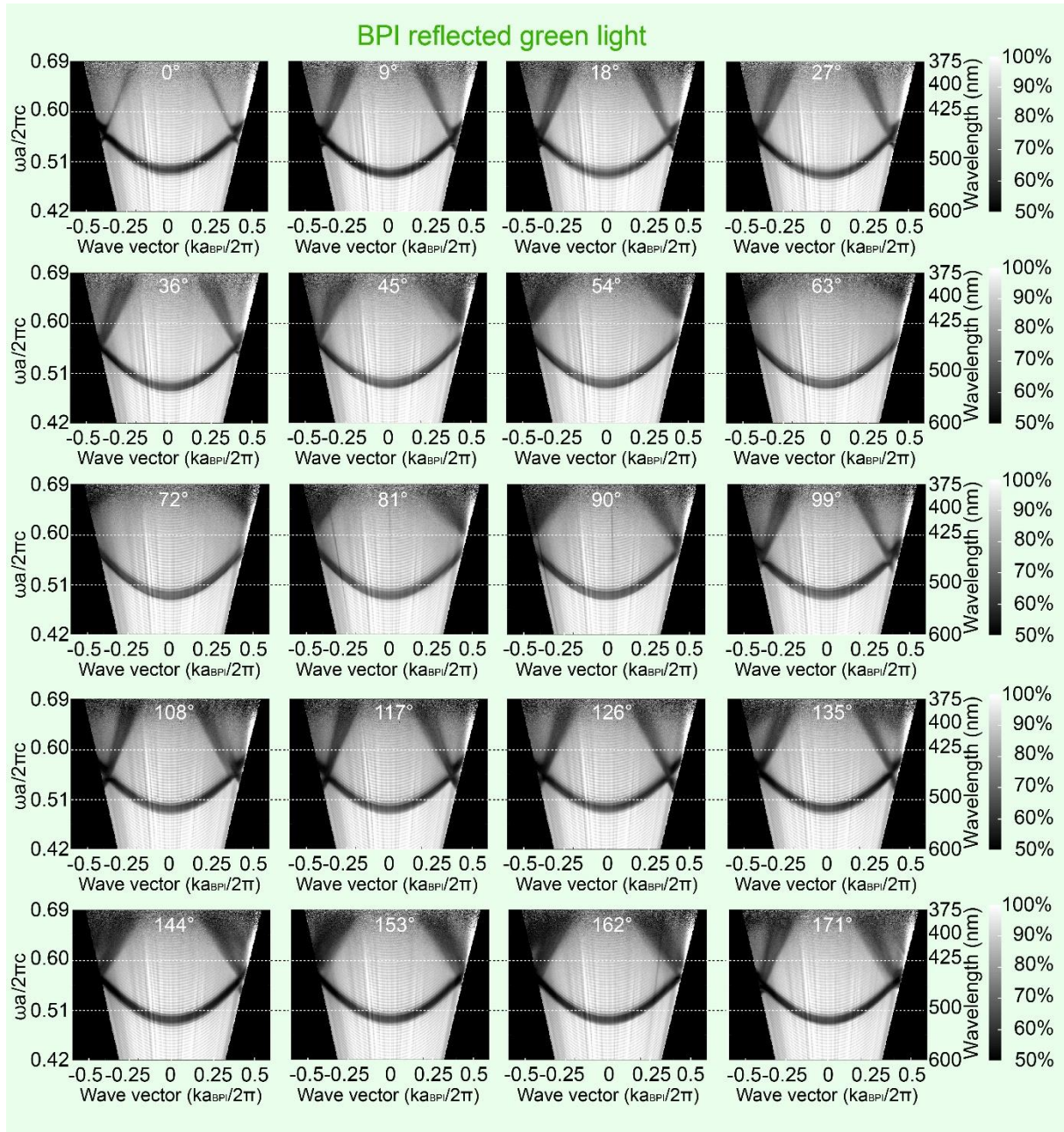
995 Simultaneously, the rotation of the parent BPII phase and the resulted {211}<sub>BPI</sub> // {110}<sub>BPII</sub>  
 996 can be confirmed by the syn-SAXS results. At an early stage of phase transition, just an  
 997 approximately parallel relationship between {211}<sub>BPI</sub> and {110}<sub>BPI</sub> can be observed,  
 998 corroborating by close but not overlapping speckles shown in (d<sub>1</sub> and d<sub>3</sub>). However, the BPII<sub>{100}</sub>  
 999 rotates during the phase transformation, resulting in {110}<sub>BPII</sub> parallels with {211}<sub>BPI</sub> (d<sub>2</sub> and  
 1000 d<sub>4</sub>) which is confirmed by the well overlapping of speckles originated from {211}<sub>BPI</sub> and



1001  $\{110\}_{\text{BPII}}$  in a monodomain PS-BPLCs hybrid with  $\text{BPI}_{\{110\}}$  and  $\text{BPII}_{\{100\}}$ . Besides, the 2-Theta  
1002 values corresponding to  $\{110\}_{\text{BPII}}$  and  $\{211\}_{\text{BPI}}$  are similar (Supplemental Figs. 46e<sub>3</sub>-f<sub>3</sub>, 47c<sub>1</sub>-  
1003 d<sub>1</sub>, and 48), providing the coherent of crystal lattices between  $\{110\}_{\text{BPII}}$  and  $\{211\}_{\text{BPI}}$  which is  
1004 an evidence for the thermoelastic martensitic transformation.

1005

1006

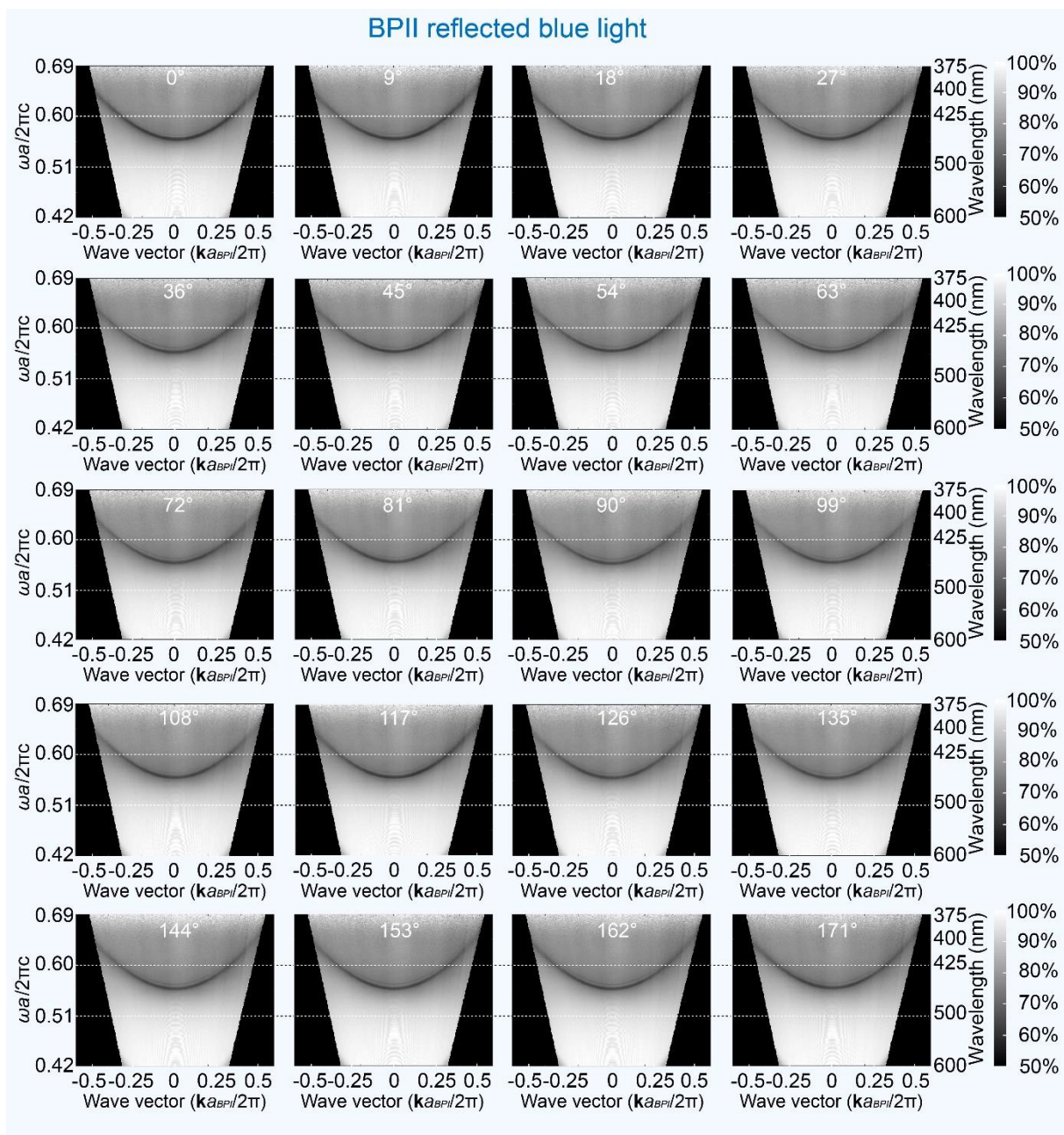


1007  
 1008 **Supplementary Fig. 57** Contour plots of measured transmittance by rotating the monodomain BPI<sub>{110}</sub>  
 1009 (reflected green light) film from 0° to 171° along [110] direction. The color scale indicates the transmissivity  
 1010 of the measured area. The colour scale on the right side of each row is also available for the four spectra in  
 1011 which row.

1012  
 1013 It is found that the anticrossings of streaks moving inward and outward periodically on the  
 1014 spectra when we rotate the azimuthal incident angle of the light irradiated onto BPI which  
 1015 reflected green light. The shapes of the streaks indicate that the normal incident angle  
 1016 corresponds to  $\overline{\Gamma N}$  ([110]) direction which is confirmed by TEM (Supplementary Fig. 31).

1017 When the rotation angle of the sample is 126°, a minimum incident angle is observed where  
 1018 anticrossings appear in normalized wave vector  $\frac{ka}{2\pi} = Approx. \pm 0.41 \frac{2\pi}{a_{BPI}}$  and the

1019 corresponding incident angle is the non-high-symmetry-point  $L_{\perp}$  (the perpendicular foot of  $\Gamma$   
1020 on  $\overline{HP}$ ). When sample is rotated to  $162^{\circ}$ , one maximum is observed where anticrossings appear  
1021 in normalized wave vector  $\frac{\mathbf{k}a}{2\pi} = Approx \pm 0.50 \frac{2\pi}{a_{BPI}}$  with the azimuthal angle shall correspond  
1022 to  $\overline{NP}$ . The other maximum of the anticrossing angle exceeds the observable range when the  
1023 sample is rotated to  $72^{\circ}$ , but we can still determine that azimuthal angle as the  $\overline{NH}$  direction.  
1024

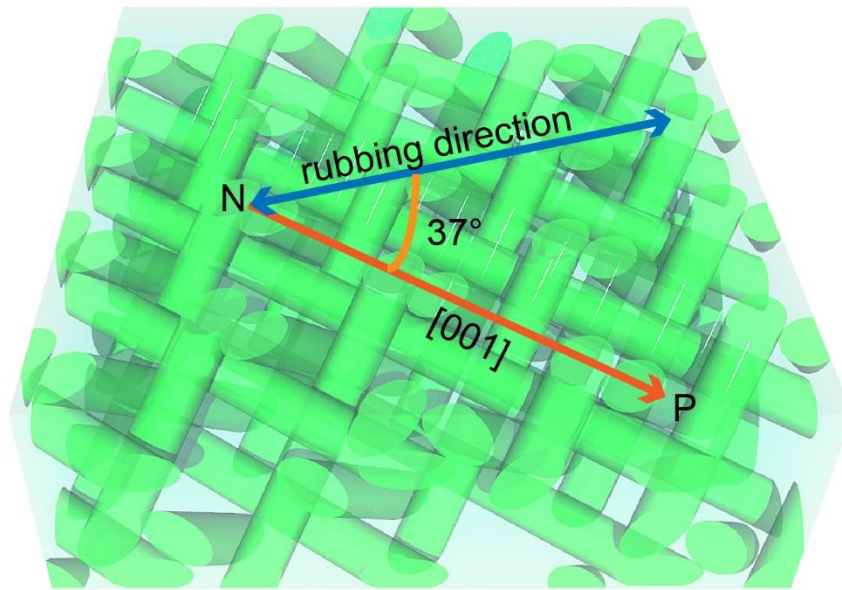


1025  
 1026 **Supplementary Fig. 58** Contour plots of measured transmittance by rotating the monodomain BPII<sub>{100}</sub>  
 1027 (reflected blue color) film from 0° to 171° along [100] direction. The color scale indicates the transmissivity  
 1028 of the measured area. The colour scale on the right side of each row is also available for the four spectra in  
 1029 which row.

1030  
 1031 The normal angle of single-domain polymer-stabilized BPII<sub>{100}</sub> shall be the  $\overline{\Gamma X}$  ([100])  
 1032 direction which is confirmed by TEM (Supplementary Fig. 27). Because of the limited  
 1033 measurement range (Supplementary Fig. 64), the shapes of the streak in transmittance spectra  
 1034 are almost the same during varying the azimuthal angles. Thus, the crystallographical  
 1035 orientations of BPII<sub>{100}</sub> cannot be recognized through ARM.

1036

1037

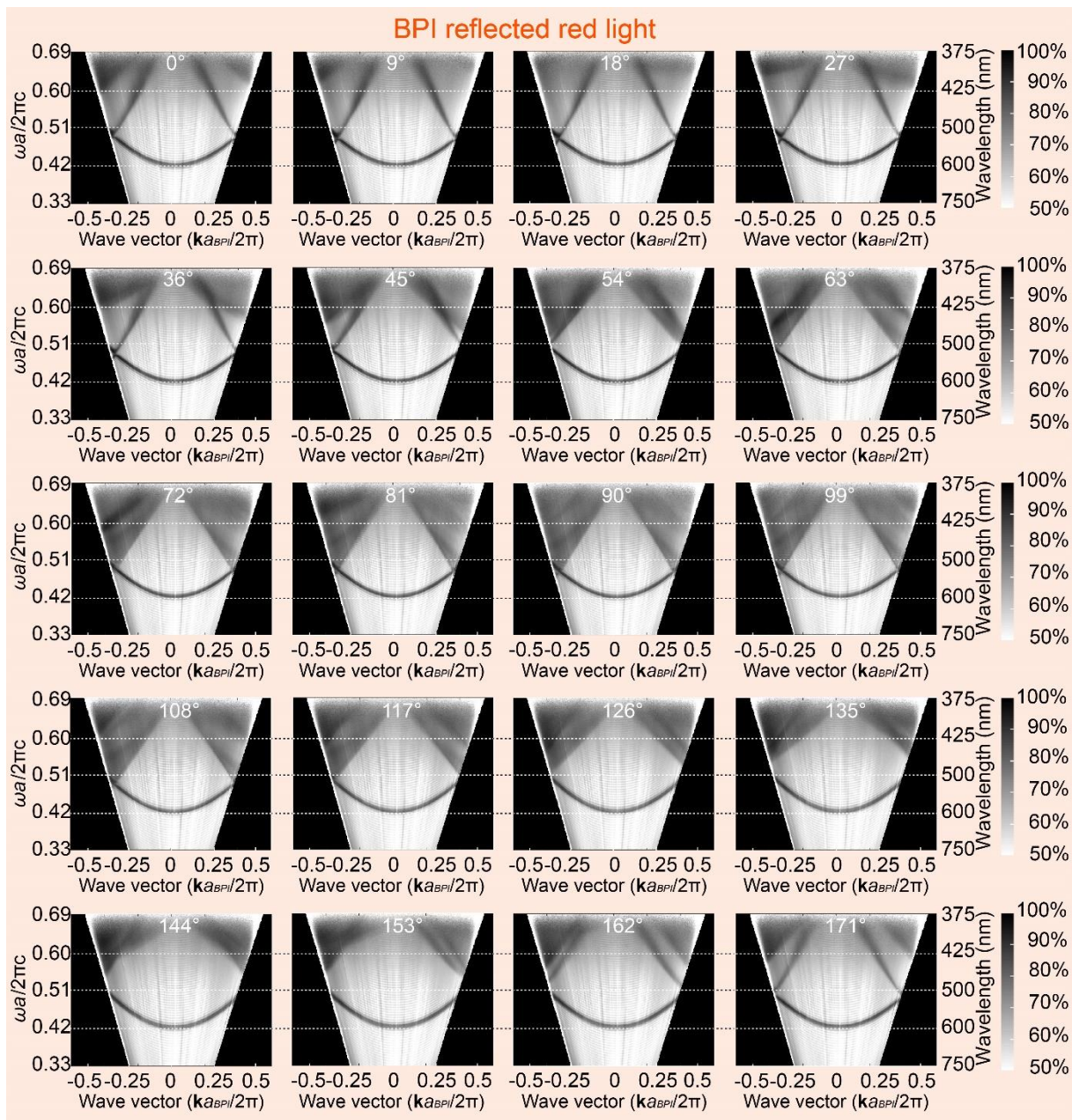


1038  
1039  
1040

**Supplementary Fig. 59** Schematic illustration of the angle between  $\overline{NP}$  direction and rubbing direction.

1041  
1042  
1043  
1044  
1045

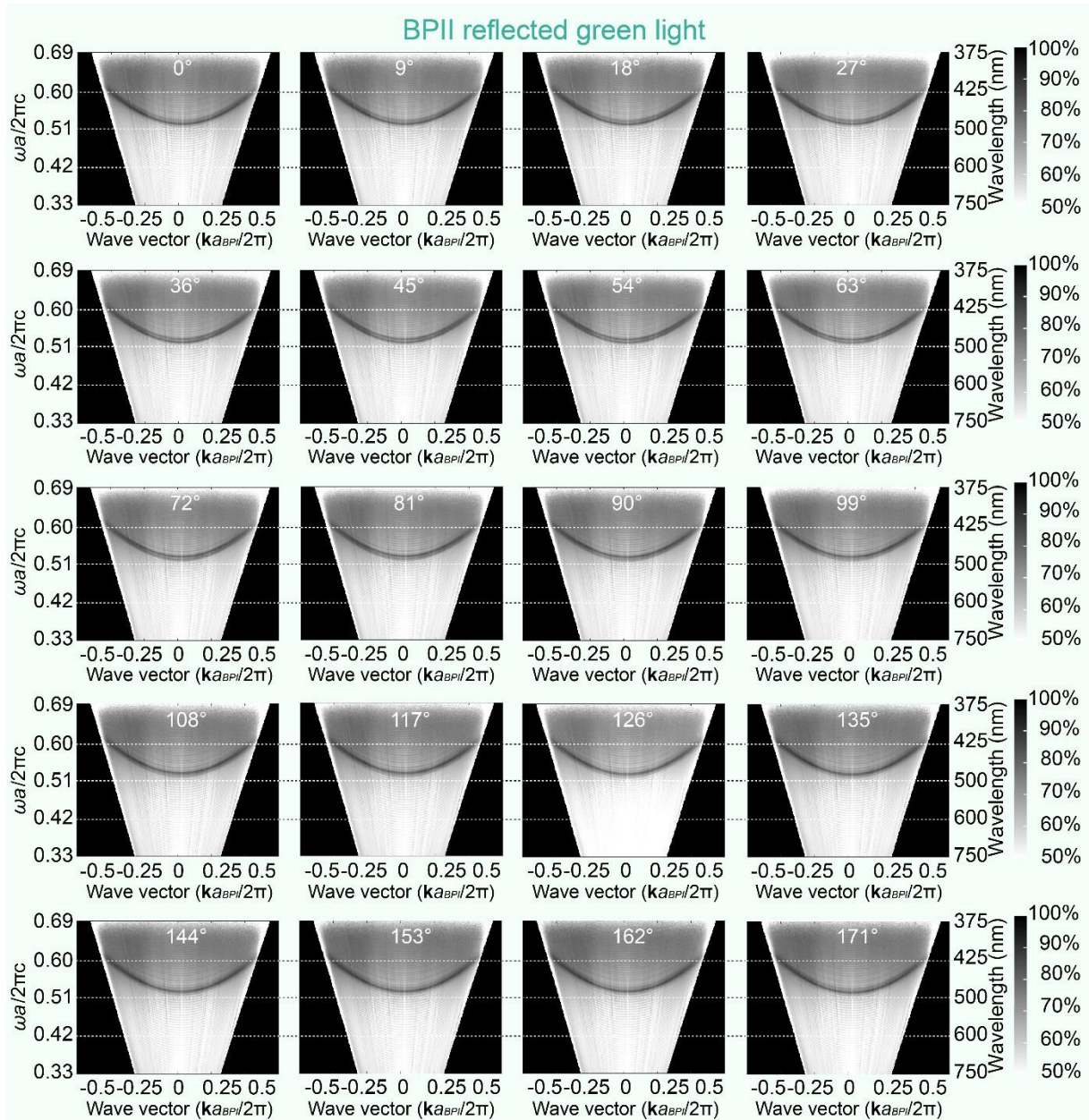
The angle between rubbing direction and  $\overline{NP}$  direction ( $[001]$  of BPI) is measured as  $37^\circ$ . Thus, the azimuthal angle and orientation of BPI can be determined by rubbing direction. The vector shown in the schematic image approximately coincides with the  $[001]$  in-plane orientation of the single-crystal  $BPI_{\{110\}}$  domain.



1046  
 1047 **Supplementary Fig. 60** Contour plots of measured transmittance by rotating the monodomain BPI<sub>{110}</sub>  
 1048 (reflected red color) film from 0° to 171° along [110] direction. The color scale indicates the transmittivity  
 1049 of the measured area. The colour scale on the right side of each raw is also available for the four spectra in  
 1050 which raw.  
 1051

1052  
 1053 Similar to BPI<sub>{110}</sub> reflected green light (Supplementary Fig. 57), the anticrossings of  
 1054 streaks moving inward and outward periodically on the spectra when the azimuthal incident  
 1055 angle of the light irradiated onto BPI rotated from 0° to 171°. The shape of the streak indicates  
 1056 that the normal incident angle corresponds to the  $\overline{\Gamma N}$  ([110] direction). When the rotation angle  
 1057 of the sample is close to 90°, the minimum incident angle is observed where anticrossings

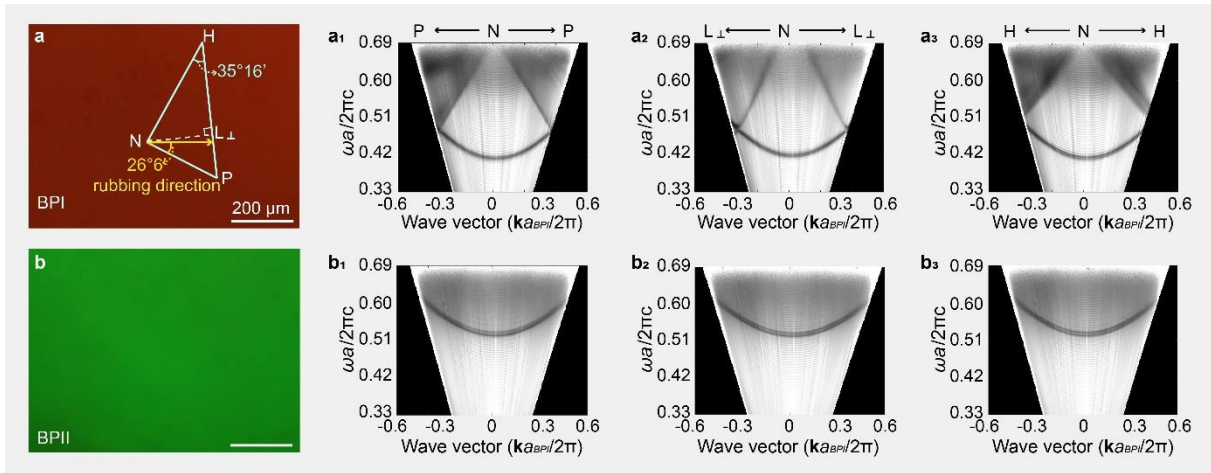
1058 appear in normalized wave vector  $\frac{\mathbf{k}a}{2\pi} \text{Approx} \pm 0.35$  and the corresponding incident angle is the  
1059 non-high-symmetry-point  $L_{\perp}$  (the perpendicular foot of  $\Gamma$  on  $\overline{HP}$ ). When the sample is rotated  
1060 to  $54^{\circ}$ , one maximum angle is observed where the azimuthal angle shall correspond to  $\overline{NP}$ . The  
1061 other maximum of the anticrossing angle also exceeds the observable range when the sample is  
1062 rotated to  $144^{\circ}$ , but we can still determine that azimuthal angle as the  $\overline{NH}$  direction.  
1063



1064  
1065 **Supplementary Fig. 61** Contour plots of measured transmittance by rotating the monodomain BPII<sub>{100}</sub>  
1066 (reflected green color) film from 0° to 171° along [100] direction. The color scale indicates the transmissivity  
1067 of the measured area. The colour scale on the right side of each row is also available for the four spectra in  
1068 which row.  
1069

1070  
1071 BPII<sub>{100}</sub> film reflects green light was measured when the azimuthal incident angle of the  
1072 light irradiated onto BPI is rotated from 0° to 171°. The photonic bandgap is located at 490.8  
1073 nm. Due to the limited measurement range, the transmittance spectra are all of the same among  
1074 distinct azimuthal angles similar to BPII<sub>{100}</sub> reflected blue light (Supplementary Fig. 58). Thus,  
1075 the crystallographical orientations of BPII<sub>{100}</sub> cannot be recognized through ARM.  
1076

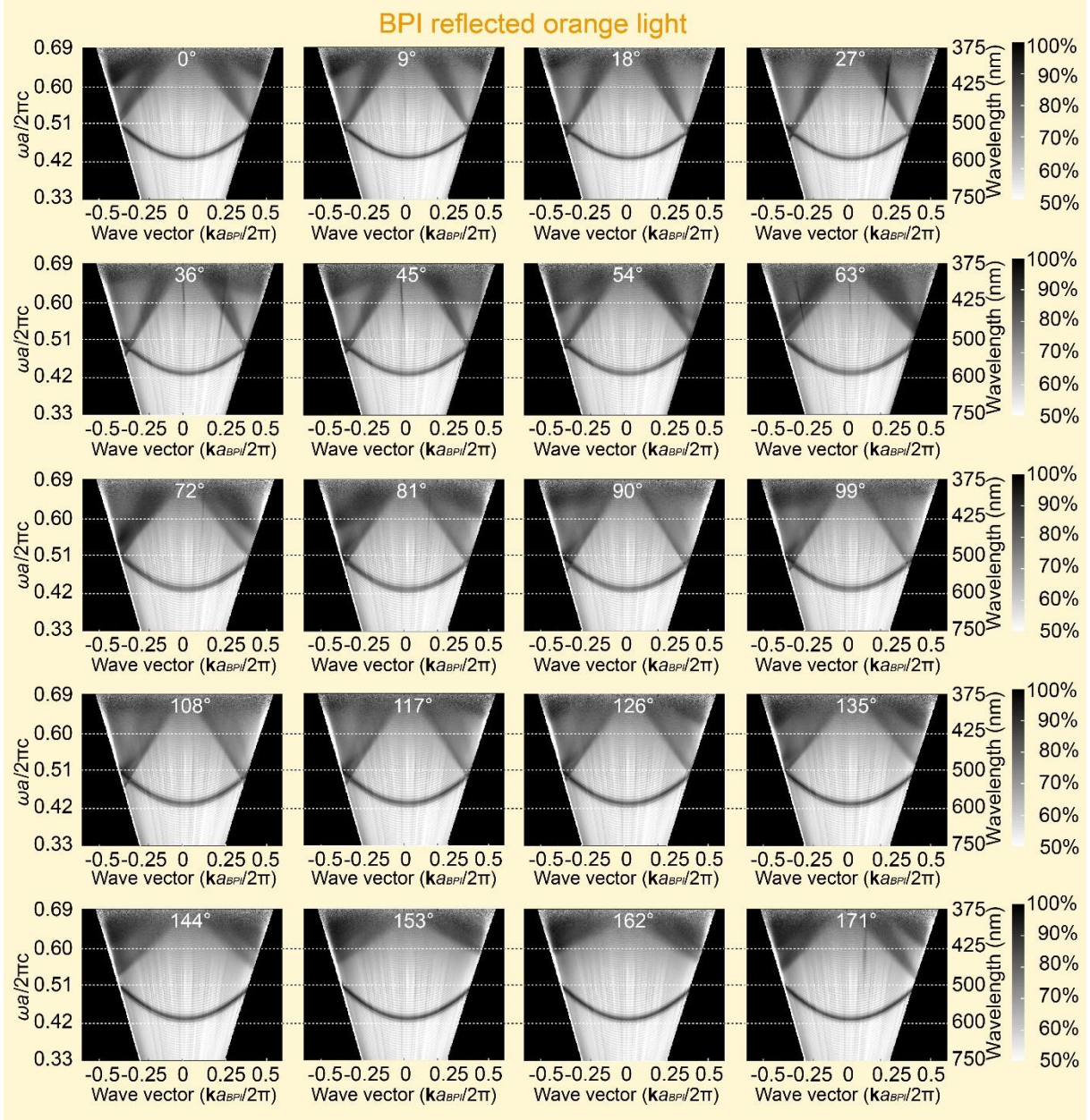




1077  
 1078 **Supplementary Fig. 62 The relationship between rubbing direction and crystal orientation.** **a** POM  
 1079 image of a typical texture of monodomain BPI<sub>{110}</sub> (reflected red light). The light blue line represents the  
 1080 detect direction. **a1**, **a2**, **a3** Contour plots of measured transmittance of BPI along the  $\overline{NP}$ ,  $\overline{NL_{\perp}}$  and  $\overline{NH}$   
 1081 orientations. **b** is a POM image of a typical texture of monodomain BPII<sub>{100}</sub> (reflected green light). **b1**, **b2**,  
 1082 **b3** Contour plots of measured transmittance of BPII<sub>{100}</sub>.  
 1083

1084 Experimental observation confirms that both the orientation of crystal planes and  
 1085 azimuthal orientations of cubic can be controlled by the rubbing direction of PI alignment layers  
 1086 and detected by the ARM measurement. Due to only one typical band structure is detected for  
 1087 crystal lattice with a particular azimuthal orientation, these results suggest that the role of the  
 1088 rubbed polyimide layers goes beyond merely forming single-crystal BPLCs: azimuthal  
 1089 orientation of BCC (BPI) can be determined by the rubbing direction of alignment layers.

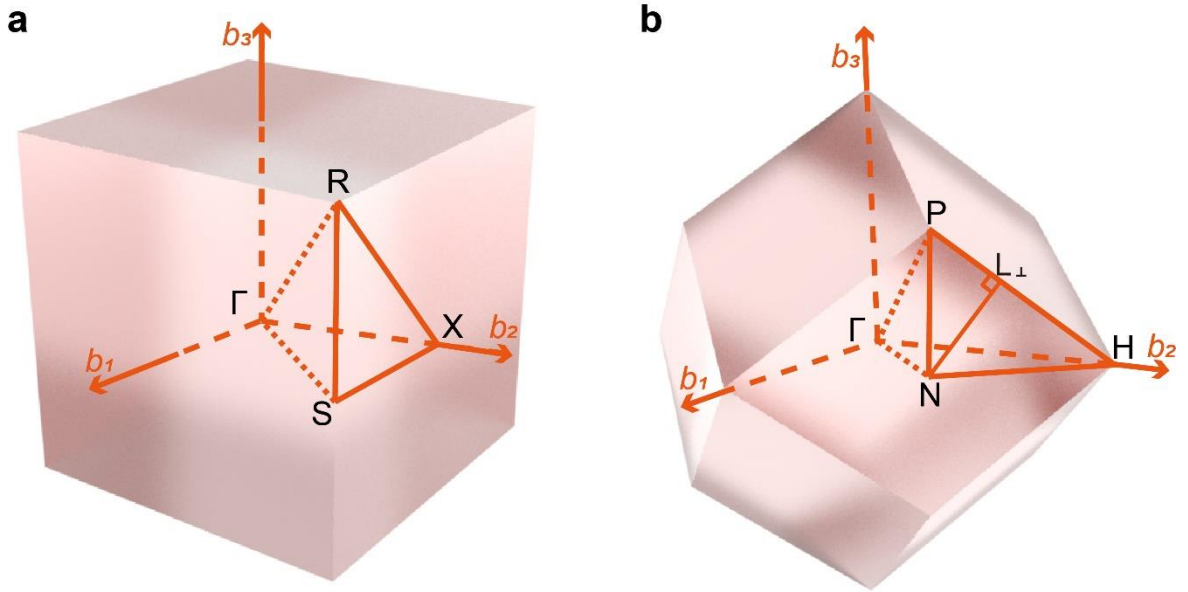
1090



1091  
 1092 **Supplementary Fig. 63** Contour plots of measured 2D transmittance by rotating the monodomain BPI<sub>{110}</sub>  
 1093 film (reflected orange light) from 0° to 171° along [110] direction. The color scale indicates the transmissivity  
 1094 of the measured area. The colour scale on the right side of each row is also available for the four spectra in  
 1095 which row.  
 1096

1097  
 1098 ARM is performed on monodomain BPI<sub>{110}</sub> film which is reflected orange light. The  
 1099 anticrossings move inward and outward periodically on the streak patterns when the azimuthal  
 1100 incident angle of the light irradiated onto BPI is rotated from 0° to 171°. The shape of the streak  
 1101 indicates that the normal direction corresponds to  $\bar{\Gamma N}$  ([110] direction). When the rotation  
 1102 angle of the sample is close to 117°, the minimum incident angle is observed of anticrossings  
 1103 appeared in normalized wave vector  $\frac{ka}{2\pi} \text{ approx. } \pm 0.38 \frac{2\pi}{a_{BPI}}$  and the corresponding incident

1104 angle is the non-high-symmetry-point  $L_{\perp}$  (the perpendicular foot of  $\Gamma$  on  $\overline{HP}$ ). When the  
1105 sample is rotated close to  $63^{\circ}$ , one maximum is observed is considered as  $\overline{NP}$  direction. The  
1106 other maximum of the anticrossing angle also exceeds the observable range when the sample is  
1107 rotated close to  $153^{\circ}$ , but we can still determine that the azimuthal angle as the  $\overline{NH}$  direction.  
1108  
1109



1110  
1111 **Supplementary Fig. 64** Irreducible BZs with symmetry points of (a) BPII and (b) BPI.  
1112

1113 Irreducible BZ of BPII is a cubic (a), and its high symmetry points are labeled by  $\Gamma$ ,  $S$ ,  $R$ ,

1114 and  $X$ . The coordinates of the points are  $\Gamma: (0,0,0) \frac{2\pi}{a_{\text{BPII}}}$ ,  $S: (\frac{1}{2}, \frac{1}{2}, 0) \frac{2\pi}{a_{\text{BPII}}}$ ,  $R: (\frac{1}{2}, \frac{1}{2}, \frac{1}{2}) \frac{2\pi}{a_{\text{BPII}}}$  and  $X:$

1115  $(0, \frac{1}{2}, 0) \frac{2\pi}{a_{\text{BPII}}}$  ( $a_{\text{BPII}}$  is the lattice constant of BPII of 167.33 nm, Supplementary Fig. 48). The

1116 distance among high symmetry points of BPII in  $k$ -space are calculated and further normalized

1117 by  $k_0 = \frac{2\pi}{a_{\text{BPII}}} = 0.0375 \text{ nm}^{-1}$ . The distance between  $X$  and  $S$  points  $XS = 0.0188 \text{ nm}^{-1}$  (normalized

1118 wave vector of  $0.5002 \frac{2\pi}{a_{\text{BPII}}}$ ) and distance between  $X$  and  $R$  points  $XR = 0.0265 \text{ nm}^{-1}$  (normalized

1119 wave vector of  $0.7072 \frac{2\pi}{a_{\text{BPII}}}$ ). Compared with Figure 3C<sub>2</sub> in the main text showing the observable

1120 range of normalized wave vector is around  $\pm 0.33 \frac{2\pi}{a_{\text{BPII}}}$ , the distance between each BPII's BZ

1121 edge and the normal incident angle is beyond the observable range. As for BPI, the shape of

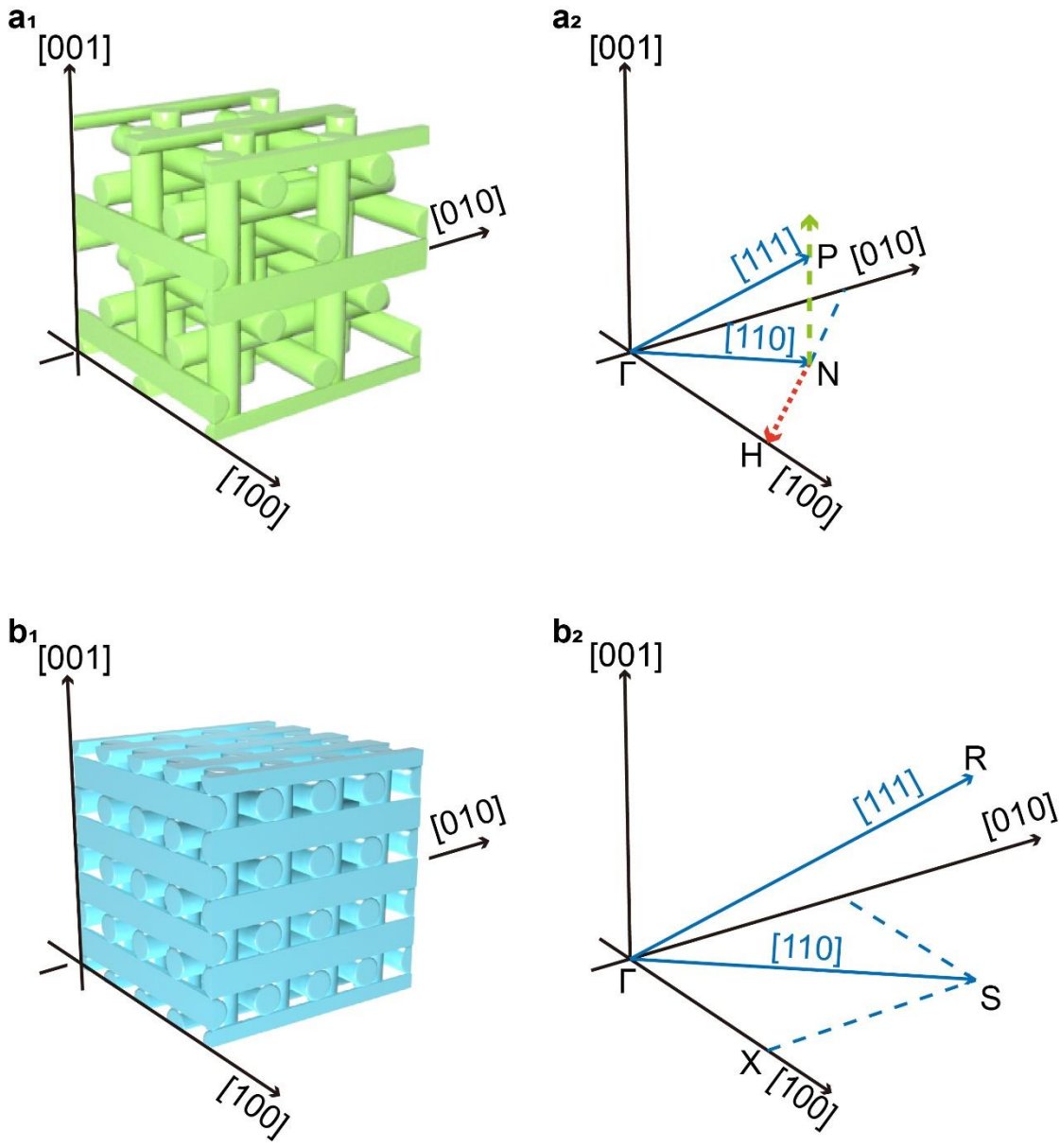
1122 irreducible BZ of BPI is a regular dodecahedron and its high symmetry points are labeled by  $\Gamma$ ,

1123  $N$ ,  $P$ , and  $H$  where a non-high-symmetry-point  $L_{\perp}$  represents the perpendicular foot of  $N$  on

1124  $\overline{HP}$ . The coordinates of the points are  $\Gamma: (0,0,0) \frac{4\pi}{a_{\text{BPI}}}$ ,  $N: (\frac{1}{4}, \frac{1}{4}, 0) \frac{4\pi}{a_{\text{BPI}}}$ ,  $P: (\frac{1}{4}, \frac{1}{4}, \frac{1}{4}) \frac{4\pi}{a_{\text{BPI}}}$  and  $H:$

1125  $(0, \frac{1}{2}, 0) \frac{4\pi}{a_{\text{BPI}}}$  ( $a_{\text{BPI}}$  is the lattice constant of BPI of 254.48 nm, Supplementary Fig. 48). The

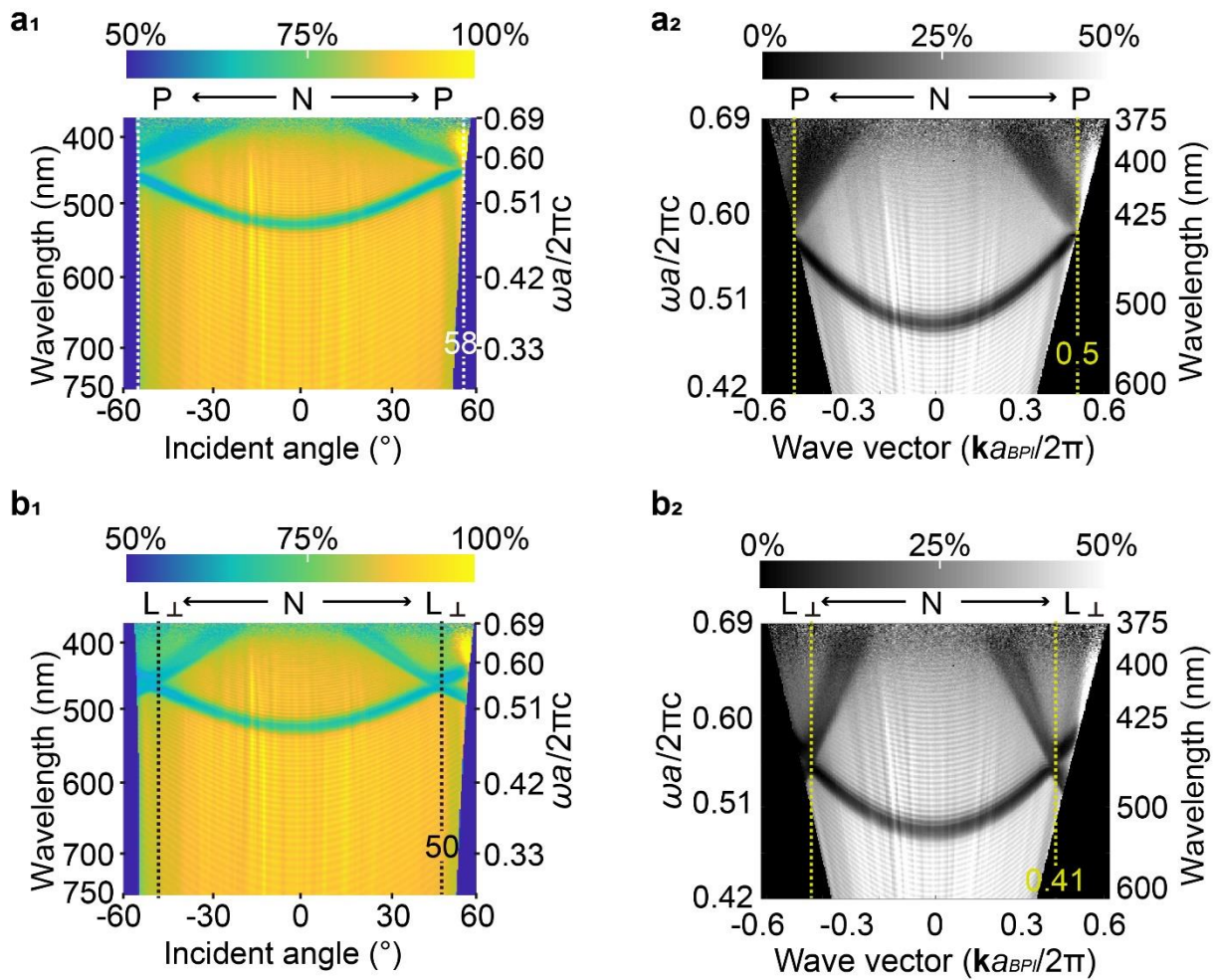
1126 distance among high symmetry points of BPII in k-space are calculated and further normalized  
1127 by  $k_0 = \frac{2\pi}{a_{\text{BPI}}} = 0.0247 \text{ nm}^{-1}$ . The distance between  $N$  and  $P$  points  $NP = 0.0123 \text{ nm}^{-1}$  (normalized  
1128 wave vector of  $0.4984 \frac{2\pi}{a_{\text{BPI}}}$  agrees well with Figure 3B<sub>2</sub> in the main text). The distance between  
1129  $N$  and  $L_{\perp}$  points is  $NL_{\perp} = 0.0100 \text{ nm}^{-1}$  (normalized wave vector of  $0.4065 \frac{2\pi}{a_{\text{BPI}}}$  agrees well  
1130 with Figure 3B<sub>3</sub>, in the main text). The distance between  $N$  and  $H$  points  $NH = 0.0173 \text{ nm}^{-1}$   
1131 (normalized wave vector of  $0.7027 \frac{2\pi}{a_{\text{BPI}}}$ , indicating this anticrossings are beyond the observable  
1132 range (around  $\pm 0.63 \frac{2\pi}{a_{\text{BPI}}}$  in Figure 3B<sub>4</sub> in the main text))  
1133



1134  
 1135 **Supplementary Fig. 65 Direction of measured transmittance and endpoints of BZ are highlighted in**  
 1136 **the real-space model.  $\mathbf{a}_1$  Model of 8 unit cells ( $2 \times 2 \times 2$ ) of BPI.  $\mathbf{a}_2$  Direction of  $\overline{NP}$  highlighted by green**  
 1137 **dash arrow and  $\overline{NH}$  highlighted by a red dotted arrow in a coordinate which is the same as ( $\mathbf{a}_1$ ).  $\mathbf{b}_1$  Model**  
 1138 **of 64 unit cells ( $4 \times 4 \times 4$ ) of BPII.  $\mathbf{b}_2$  Endpoints of BZ are labeled X, M, and R in a coordinate that is the same**  
 1139 **as ( $\mathbf{b}_1$ ). The labels of P, N, H, and  $\Gamma$  (R, M, X, and  $\Gamma$ ) represent the high-symmetry directions for BPI (BPII).**  
 1140

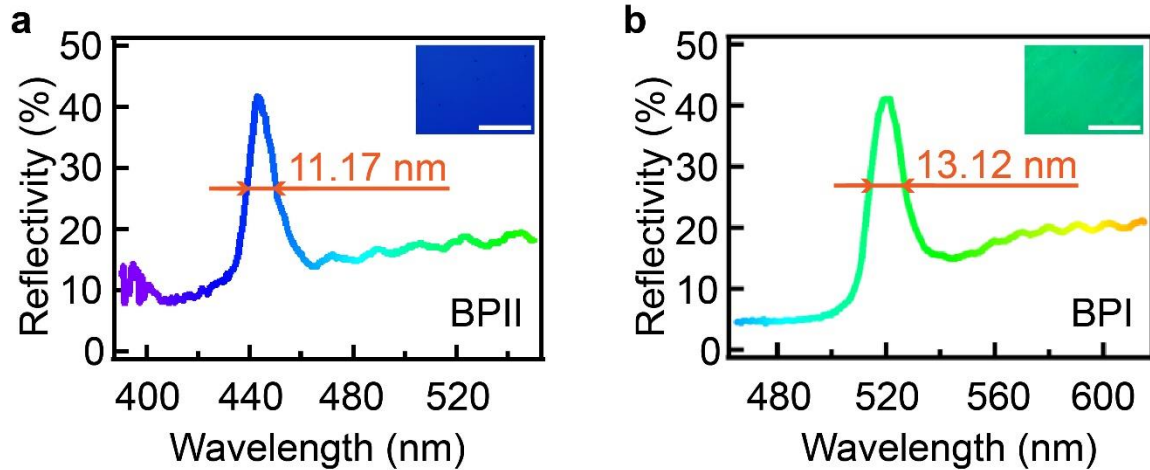
1141 The high symmetry points in reciprocal space of P, N, H, and  $\Gamma$  ( $\mathbf{a}_1$ ) are labeled in real-  
 1142 space BPI model ( $\mathbf{a}_2$ ) and R, M, X, and  $\Gamma$  ( $\mathbf{b}_1$ ) are labeled in real-space BPII model ( $\mathbf{b}_2$ ). The  
 1143 coordinates used here are the same.

1144  
 1145  
 1146



1147  
 1148  
 1149  
 1150  
 1151  
 1152

**Supplementary Fig. 66** Contour plots of measured transmittance of monodomain polymer-stabilized  $BPI_{110}$  along (a<sub>1</sub>, a<sub>2</sub>)  $N \rightarrow P$ , (b<sub>1</sub>, b<sub>2</sub>)  $N \rightarrow L_{\perp}$  and direction. The color scale indicates the reflectivity.



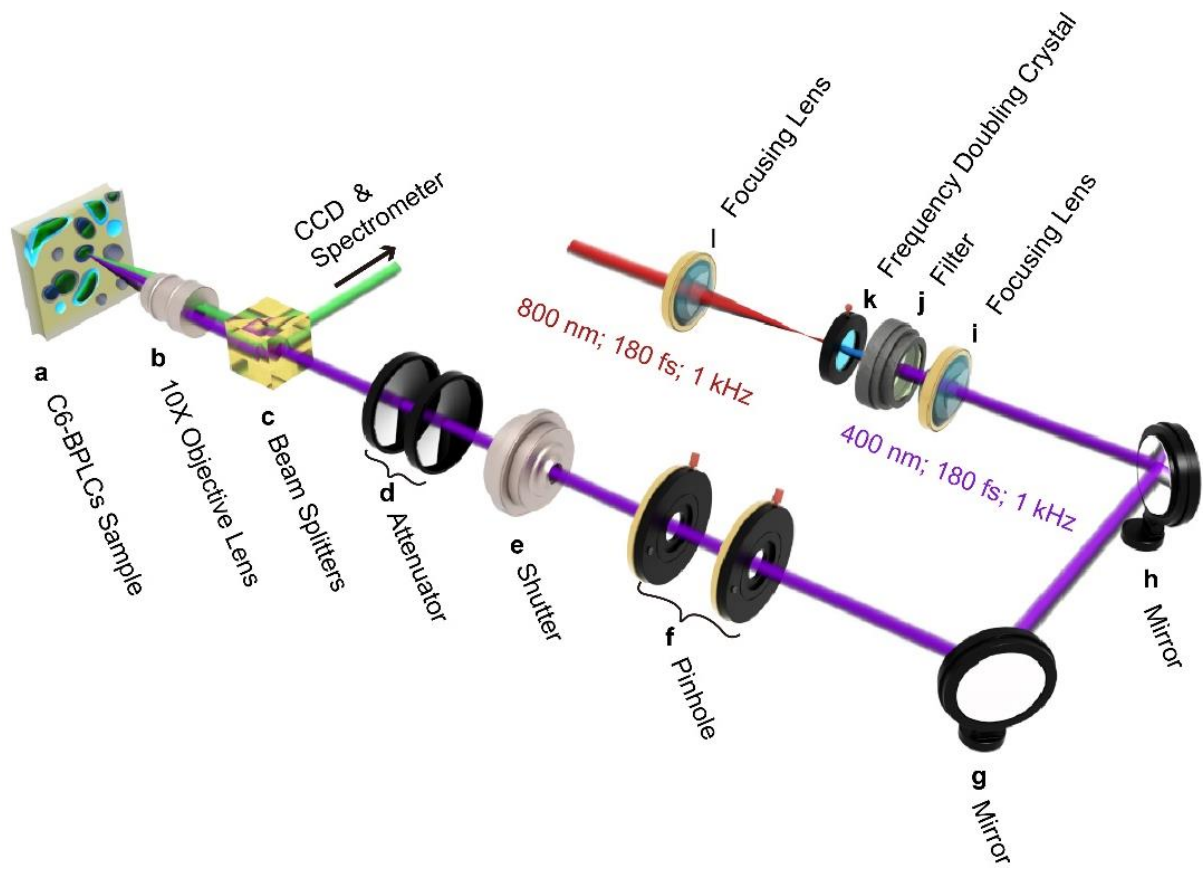
1153  
 1154 **Supplementary Fig. 67** Reflection spectra of (a) monodomain BPII<sub>{100}</sub> and (b) BPI<sub>{110}</sub>. Inserted images  
 1155 is POM images of monodomain BPII<sub>{100}</sub> and BPI<sub>{110}</sub>. The scale bar is 400 nm.  
 1156

1157 The FWHM of reflection spectra of BPI<sub>{110}</sub> and BPII<sub>{100}</sub> reflect the width of the photonic  
 1158 bandgap to a certain extent. In this case, the FWHM of BPII<sub>{100}</sub> of 11.17 nm is narrower than  
 1159 that of BPI<sub>{110}</sub> (13.12 nm), which agrees with the calculated band structures (see Figures 1b5,  
 1160 1c<sub>3</sub> in the main text).

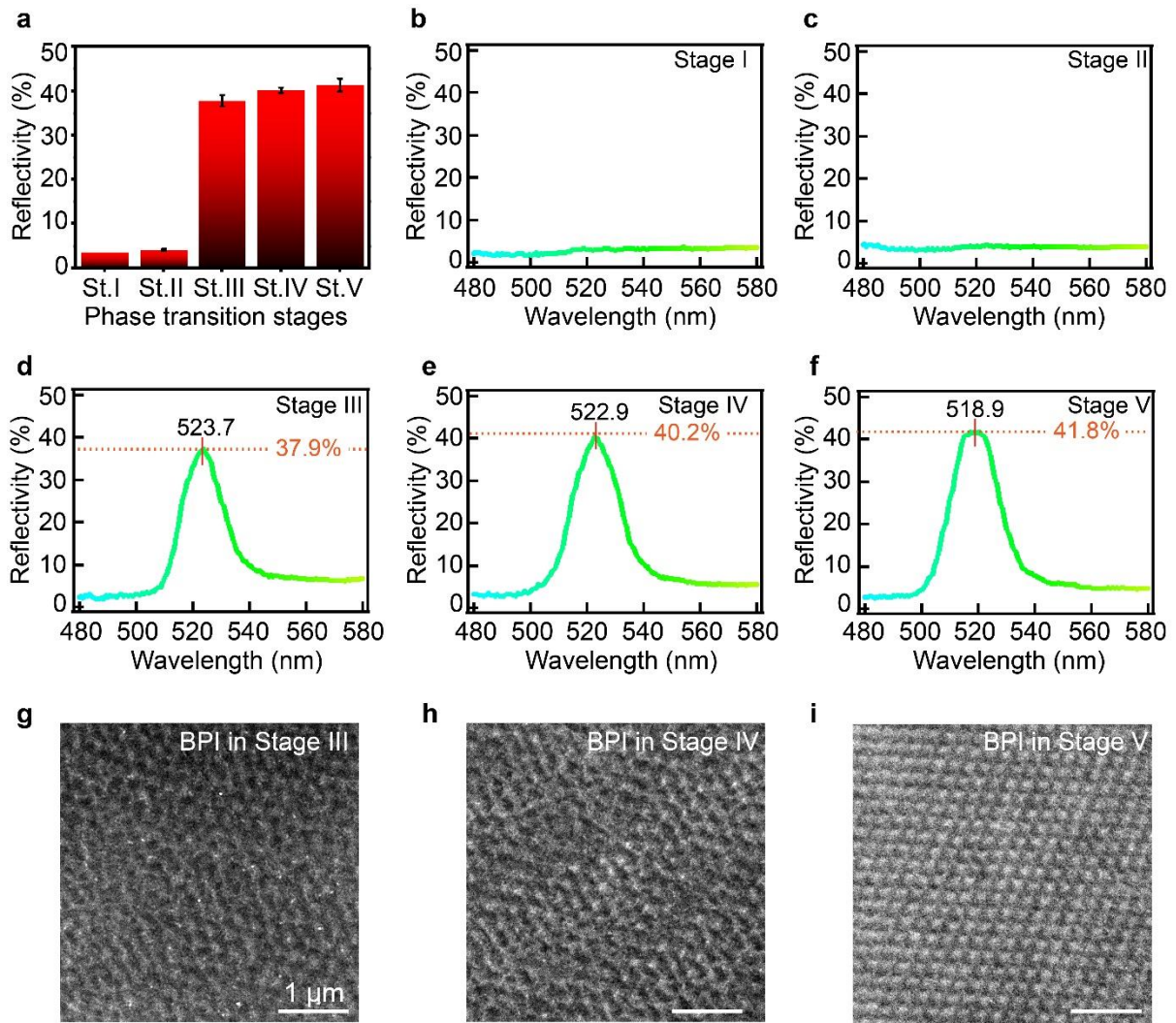
1161 In addition, the crystal lattices of monodomain BPLCs have higher quality than  
 1162 polydomain BPLCs. The FWHM of monodomain BPI (BPII) is 13.12 (11.17) nm which is  
 1163 slightly narrower than the polydomain BPI (BPII) of 13.61 (13.67) nm (see Figure. 1E<sub>4</sub> in the  
 1164 main text).

1165





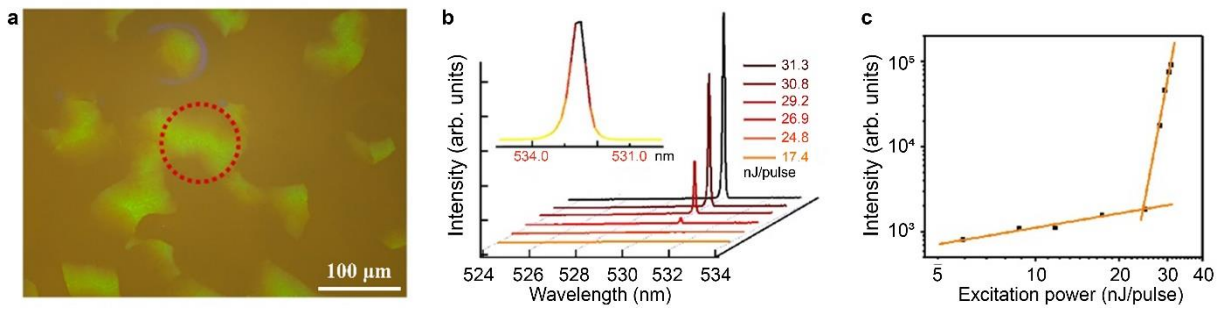
1167  
 1168 **Supplementary Fig. 68 Configuration of laser experiment for measuring the fluorescence and lasing**  
 1169 **spectra of the C6-BPLCs. a:** C6 doped self-standing PS-BPLCs sample in each stage; **b:** 10X objective  
 1170 lens (NA=0.3); **c:** beam splitters; **d:** attenuator; **e:** shutter; **f:** pinhole; **g:** mirror; **h:** mirror; **i:** focusing lens; **j:**  
 1171 filter **k:** frequency doubling crystal; **l:** focusing lens; CCD is the abbreviation of ‘Charge-coupled Device’



1172  
1173  
1174  
1175  
1176  
1177

**Supplementary Fig. 69** *In situ* reflection spectra of C6-BPLCs utilized for measurement of lasing properties of Figure 5 in the main text. **a** Overview of reflectivity in distinct stages ‘St. I’ to ‘St. V’ refer to ‘Stage I’ to ‘Stage V’. Reflection spectra of **(b)** Stage I, **(c)** Stage II, **(d)** Stage III, **(e)** Stage IV, and **(f)** Stage V. TEM images of BPI in **(g)** Stage III, **(h)** Stage IV, and **(i)** Stage V.

1178



1179

1180

1181

1182

1183

1184

1185

1186

**Supplementary Fig. 70 Lasing properties of C6-BPLCs film at Stage IV polymerized at 76.2 °C (Stage IV<sub>76.2</sub>).** **a** Textures captured by an inverted optical microscope in reflection mode. The red dotted circle highlights the excited blue phase platelet. **b** The emission spectra plotted relative to the low-energy photonic bandedge, where the inset is the lasing peak on a magnified wavelength scale. **c** Typical input-output curve. The solid lines represent the best fit to the data below and above the excitation threshold.

1187

Lasing properties in Stage IV of C6-BPLCs polymerized at 76.2 °C (Stage IV<sub>76.2</sub>) are

1187

studied. Single-mode lasing is realized at 530.70 nm with an FWHM of 0.107 nm and Q

1188

factor of 4960. It exhibits a clear threshold of 24.50 nJ/pulse as a function of pump energy.

1189

1190 **Supplementary References**

- 1191 1. Gandhi, S. S. & Chien, L. C., Unraveling the Mystery of the Blue Fog: Structure, Properties, and  
1192 Applications of Amorphous Blue Phase III. *Adv. Mater.* **2017**, *29* (47), 1704296-1704309 (2017).
- 1193 2. Chiang, I. H., Long, C. J., Lin, H. C., Chuang, W. T., Lee, J. J. & Lin, H. C., Broad ranges and fast  
1194 responses of single-component blue-phase liquid crystals containing banana-shaped 1,3,4-oxadiazole  
1195 cores. *ACS Appl. Mater. Interfaces* **2014**, *6* (1), 228-235 (2014).
- 1196 3. Kim, M. S. & Chien, L. C., Topology-mediated electro-optical behaviour of a wide-temperature liquid  
1197 crystalline amorphous blue phase. *Soft Matter*. **2015**, *11* (40), 8013-8018 (2015).
- 1198 4. Henrich, O., Stratford, K., Marenduzzo, D & Cates, M. E., Ordering dynamics of blue phases entails  
1199 kinetic stabilization of amorphous networks. *Proc. Natl. Acad. Sci. U. S. A.* **2010**, *107* (30), 13212-13215  
1200 (2010).
- 1201 5. Yang, J. J., Liu, J., Guan, B., He, W. L., Yang, Z., Wang, J. X., Ikeda, T & Jiang, L., Fabrication and  
1202 photonic applications of large-domain blue phase films. *J. Mater. Chem. C* **2019**, *7* (31), 9460-9466  
1203 (2019).
- 1204 6. Jo, S. Y., Jeon, S. W., Kim, B. C., Bae, J. H., Araoka, F. & Choi, S. W., Polymer Stabilization of Liquid-  
1205 Crystal Blue Phase II toward Photonic Crystals. *ACS Appl. Mater. Interfaces* **2017**, *9* (10), 8941-8947  
1206 (2017).
- 1207 7. Castles, F., Day, F. V., Morris, S. M., Ko, D. H., Gardiner, D. J., Qasim, M. M., Nosheen, S., Hands, P.  
1208 J., Choi, S. S., Friend, R. H. & Coles, H. J., Blue-phase templated fabrication of three-dimensional  
1209 nanostructures for photonic applications. *Nat. Mater.* **2012**, *11* (7), 599-603 (2012).
- 1210 8. Tanaka, S., Yoshida, H., Kawata, Y., Kuwahara, R., Nishi, R. & Ozaki, M., Double-twist cylinders in  
1211 liquid crystalline cholesteric blue phases observed by transmission electron microscopy. *Sci. Rep.* **2015**,  
1212 **5**, 16180-16189 (2015).
- 1213 9. Sala-Tefelska, M. M., Orzechowski, K., Sierakowski, M., Siarkowska, A., Woliński, T. R., Strzeżysz, O  
1214 & Kula, P., Influence of cylindrical geometry and alignment layers on the growth process and selective  
1215 reflection of blue phase domains. *Opt. Mater.* **2018**, *75*, 211-215 (2018).
- 1216  
1217  
1218  
1219  
1220  
1221  
1222